Academic year 2015-2016

Université de Liège

FACULTY OF SCIENCES

Department of chemistry

Coating of crystallized Yttrium Orthoferrite (o-$YFeO_3$) by wet deposition methods

Dissertation presented by

STEVENS Frédéric

To obtain the title of

Doctor of Sciences

Greenmat

Résumé

L'objectif de cette thèse est d'obtenir un dépôt d'orthoferrite d'yttrium orthorhombique sur substrat conducteur. Ceci, en vue de d'étudier de nouveaux catalyseurs potentiels pour le clivage photoélectrochimique de l'eau.

Le clivage photoélectrochomique de l'eau produit du dihydrogène et du dioxygène grâce à l'énergie solaire et un catalyseur. Le dihydrogène et le dioxygène sont les combustibles d'une réaction exothermique. Transformer l'eau en ces deux composés est donc une méthode de stockage de l'énergie.

Plusieurs semiconducteurs sont étudiés comme catalyseurs pour ce clivage. Cette thèse se concentre sur l'étude de l'un d'eux : l'orthoferrite d'yttrium orthorhombique (o-$YFeO_3$), et sur deux méthodes de dépôt de ce matériau sur substrat conducteur : la méthode de déposition par plongée (dip-coating) et la pyrolyse d'une vaporisation ultrasoniquement générée (USP).

Dans un premier temps, deux méthodes de synthèse de l'o-$YFeO_3$, sous forme de poudre, ont été envisagées : l'une basée sur des chlorures de fer et d'yttrium, l'autre basée sur les nitrates de ces mêmes métaux. Les éventuels problèmes de proportion ou de précipitations successives ont été respectivement dissipés par une étude de masse et une analyse de l'évolution du pH. Ces poudres, issues des chlorures ou des nitrates, ont permis de caractériser la proportion et la pureté des phases cristallines en fonction de la température de calcination par l'étude de la diffraction des rayons X (XRD) ; de caractériser l'énergie de la bande interdite (band gap optique) par la spectroscopie de réflectance diffuse (DRS) et d'en observer leur morphologie par les microscopies électroniques à balayage (SEM) ou en transmission (TEM). Toutes ces analyses nous ont poussés à continuer notre étude en nous focalisant sur la synthèse basée sur les nitrates et d'utiliser une température de calcination de 850°C.

Ensuite, ces mêmes analyses (pH, XRD, DRS) ont permis d'estimer l'influence de l'ajout de différents composés organiques en cours de synthèse sur la cristallinité, la pureté, la température de calcination et l'énergie de la bande interdite de ces poudres. Cette thèse a montré que l'additif qui améliore au maximum ces propriétés est l'acide citrique. Dans le cas des poudres, dès 450°C

– soit 400°C de moins que la même synthèse sans acide citrique – l'o-$YFeO_3$ est cristallisé. Les solutions qui seront utilisées pour les méthodes de déposition seront donc composées à partir, entre autre, de nitrate de fer, de nitrate d'yttrium et d'acide citrique.

La méthode dite du « dip-coating » consiste à plonger le substrat qu'on compte recouvrir dans une solution de précurseurs – composée, entre autre, des nitrates métalliques et d'acide citrique – de le ressortir recouvert d'un film mince de cette solution pour ensuite le chauffer et ainsi obtenir un dépôt du matériau désiré. De nombreux problèmes d'adhérence, de stabilité de solution, de quantité de matière, d'homogénéité de dépôt et de cristallisation de composé ont eu raison de nos efforts pour la mise au point de tels dépôts par cette technique.

L'autre méthode de déposition utilisée durant cette thèse est l'«USP ». Cette technique vaporise une solution de précurseurs au moyen de vibrations ultrasoniques. Le brouillard ainsi généré est propulsé vers le substrat par du gaz sous pression. Le substrat, pendant ce processus, est placé sur une plaque chauffante. La solution vaporisée chauffera au fur et à mesure qu'elle se rapprochera du substrat. Cette technique implique l'ajustement de plusieurs paramètres qui définissent le type de composés qui atteindront le substrat. Cette thèse a abouti à la mise au point de ces différents paramètres qui ont permis d'obtenir un dépôt d'orthoferrite d'yttrium orthorhombique sur un substrat conducteur. Ce dépôt présente une activité photoélectrochimique en tant qu'anode pour le clivage de l'eau, mais ses performances ne permettent pas, dans son état actuel, de concurrencer les semiconducteurs précédement décrit par d'autres chercheurs. Une poursuite des travaux dans ce domaine devraient se focaliser sur le dopage et/ou la structuration contrôlée de l'orthoferrite d'yttrium.

Table of content

Introduction

1. Context

The world's population grows bigger and bigger[1]. Energy needs and carbon dioxide emissions (fig. 1 and 2) follow the same trend. This correlation is mainly due to the fact that fossil fuel is our most important source of energy and carbon dioxide gas comes from its combustion. This gaseous compound is often pointed to as one of the main factor of global warming. Moreover, fossil fuels have a regeneration rate far slower than that of their usage rate. Indeed, in 2014, the reserve-to-production ratios of oil, natural gas and coal were estimated to be 53, 54 and 110 years respectively[2]. To support the evolution of the world's population and its energy needs, it is necessary to develop or create a technology that produces enough energy in the cleanest possible way and from a source that will not diminish on the time scale of the human race's existence. These energy sources are sometimes called renewables.

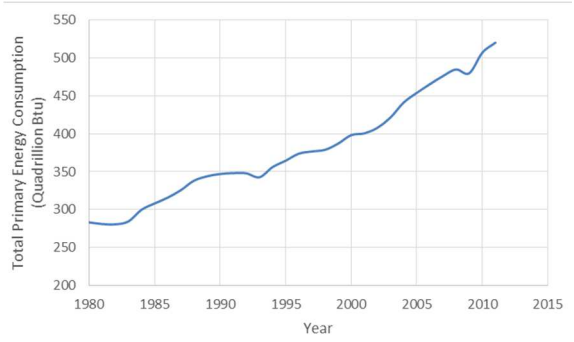

Figure 1. Evolution of primary energy consumption from 1980 to 2012.[3]

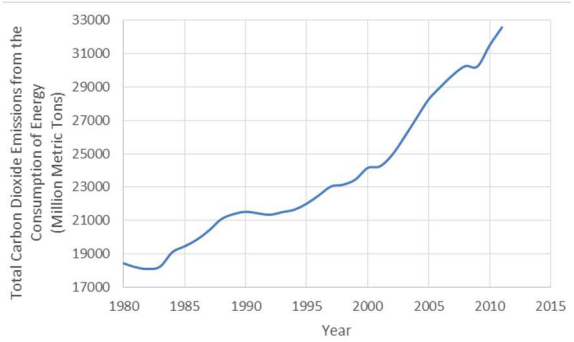

Figure 2. Evolution of CO_2 emission from 1980 to 2012.[4]

Sun, wind and tides are CO_2-neutral renewable energies. These energy sources are not, at this time, massively used because their production of electricity is, unfortunately not, produced at the time and in the place that they are required. Furthermore, the electricity produced by these sources is more expensive than the electricity produced from fossil fuels.

An energy carrier that can be stored and converted into electricity on a large scale may reduce the price of these technologies.

One possible energy carrier is dihydrogen. Its combustion is exothermic and does not produce carbon dioxide (eq. 1).

$$2H_{2g} + O_{2g} \rightarrow 2H_2O_l \qquad \Delta H = -285{,}9\ kJ/mol$$ *Equation 1: dihydrogen combustion*

Research and development focus on two main areas: The production and the storage of the two gases – dihydrogen and dioxygen– required for this reaction.

Dihydrogen is mainly obtained from fossil fuels via steam reforming, partial oxidation, plasma reforming or coal gasification[5-8]. All these methods are based on fossil fuel. H_2 is also produced from water via electrolysis or thermolysis.[9,10].

The actual storage of this gas requires a pressurized or refrigerated tank[11] and research is focused on solid state storage like microporous material, zeolithes, Metal-Organic Frameworks, alloys, carbon based-compounds and hydrides[12-16].

Dioxygen is produced industrially by the fractional distillation of liquefied/cryogenized air, by the air filtering/adsorption method through molecular sieves made of zeolithe or metal oxides, or by water electrolysis.[9,17-20]. The gas is stored in high pressure oxygen tanks, cryogenic tanks or in chemical compounds[21-23].

This thesis will contribute to the development of research in the field of energy carriers by exploring the conception of new materials that may produce H_2 as a potential energy carrier.

2. Water splitting

Water splitting (eq. 2) is the reaction by which water is transformed into dihydrogen and dioxygen.

$$2H_2O_l \rightarrow 2H_{2g} + O_{2g} \qquad \Delta H = +285{,}9\ kJ/mol$$ *Equation 2: water splitting reaction*

As an endothermic reaction, energy must be supplied to the system. The sun, among other energy sources, can deliver the required energy. In this particular case, the reaction is also called photoelectrolysis of water or photo-water splitting.

Although the sun shines on oceans, the water does not spontaneously transform into H_2 and O_2 (fig. 3). This reaction has to be catalyzed thanks to the use of suitable semiconductor. A catalyst increases the reaction rate. This reaction rate depends on the frequency of contact between water molecules and electrochemically active species, like electrons and holes. These species are generated in the catalyst, a semiconductor, by solar energy. The contact between water and the active species occurs at the surface of the catalyst. If the catalyst is porous or

presents an important surface, like reduced particle size, the reactivity will be improved. However, very small particle size significantly decreases the crystallinity, influencing charge mobility and increased surface recombination, which reduces the catalytic efficiency (see further)[25].

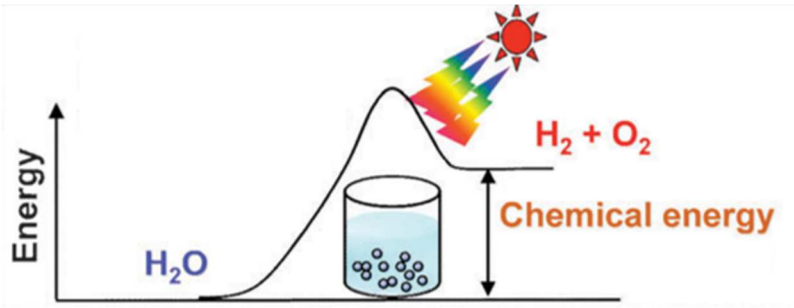

Figure 3: Catalyzed photo-water splitting[24]

The electronic band structure defines the photocatalytic properties of semiconductors[26]. Solar energy transfers an electron from the valence band to the conduction band (fig. 4). This electron excitation results in an electron-hole pair. The electron (e^-) belongs to the conduction band (CB) and the hole (h^+) belongs to the valance band (VB) (fig. 4).

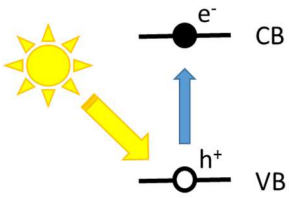

Figure 4: Sunlight provides the energy to excite an electron from the valance band (VB) of a semiconductor to its conduction band (CB).

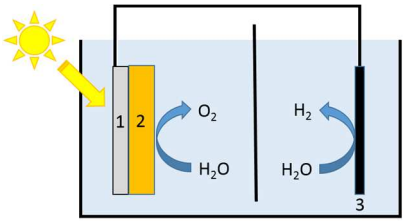

Figure 5: Water splitting cell made of an anode containing a semiconductor (2) coated on a transparent conducting oxide (1) and a cathode (3).

The reactor is represented in fig. 5. This cell is composed of two electrodes. One of the electrodes supports the semiconductor where the electron-hole pair is generated. The excited electron (e^-), localized on the conduction band of the semiconductor, migrates through this semiconductor(2) to reach the conductive electrode(1) and reach the cathode(3) before being recombined with one hole (h^+).

It is important to avoid, or at least minimize, the recombination because it reduces the cell's efficiency[24]. Indeed, if they recombine, these electrons cannot travel through the external circuit to reach the cathode. Electrons form dihydrogen at the cathode (eq. 3).

$$2H^+ + 2e^- \rightarrow H_2 \qquad E^0 = 0{,}00V vs RHE$$ *Equation 3: water reduction*

Holes (h^+) - if they are in contact with water - allow water oxidation according to the following reaction (eq. 4).

$$2H_2O + 4h^+ \rightarrow O_2 + 4H^+ \quad E^0 = -1{,}23V vs RHE$$ *Equation 4: water oxidation*

The combination of these two reactions gives the overall water splitting reaction (eq. 5).

$$2H_2O \rightarrow 2H_2 + O_2 \qquad \Delta E^0 = -1{,}23V$$ *Equation 5: water splitting*

Water oxidation limits the speed of the reaction. Indeed to obtain one molecule of dioxygen, four holes are required, compared to water reduction where only two electrons produce one molecule of dihydrogen. It is the reason why this thesis is focused on the photoanode's conception.

3. The Photoanode

This electrode is composed of two parts: a substrate and a semiconductor coating.

In this thesis, a conductive, transparent and stable substrate is used. The conductivity is required to play the role of an electrode. Newly generated charges must be able to migrate toward the external circuit. Front and back illumination of the electrode can be considered in the case of a transparent substrate and finally, the substrate must not be affected during the synthesis process of this electrode: melting and cracks are not permitted to obtain a reproducible electrode.

The semiconductor must have a suitable band gap. This means that the potential of the valence band edge must be more positive than the oxidation potential of water – equal to +1,23V versus Normal Hydrogen Electrode (NHE) at pH 0 (or +0,82V at pH 7) - for the photochemical water oxidation to occur and the flat band potential has to be more negative than the proton reduction - equal to 0,0V versus ENH at pH 0 (or -0,41V at pH 7) - to facilitate water reduction. The flat band potential corresponds to the bottom of the conduction band of the semiconductor[24,26]. (fig. 6).

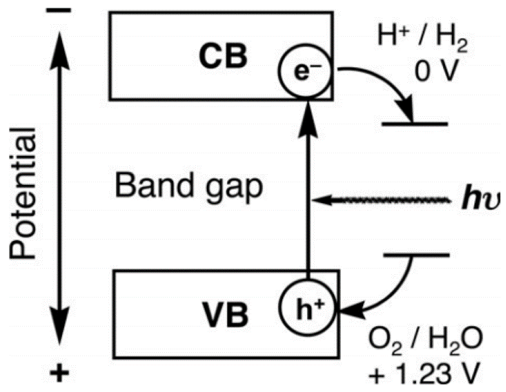

Figure 6: Energy diagram of a catalytic semiconductor for water splitting[24]

Consequently the band gap must be at least of 1,23eV. From eq. 6 and 7, the light must have a maximum wavelength of 1010nm.

$$E\ (J) = \frac{h.c}{\lambda\ (m)}$$ *Equation 6: Planck-Einstein equation*

Where *E* is the energy (in joules), *h* is the Planck constant equal to $6{,}63.10^{-34}$ J.s, *c* is the speed of light with a value of 3.10^{8} m/s and λ is the wavelength (in m). Usually, the energy unit of the band gap is expressed in electron-volt (eV) and as sunlight is considered, nanometers (nm) are used, instead of meters, for the unit of the wavelength. The simplified eq. 7 is then obtained.

$$E\ (eV) = \frac{1241\ eV.nm}{\lambda\ (nm)}$$ *Equation 7*

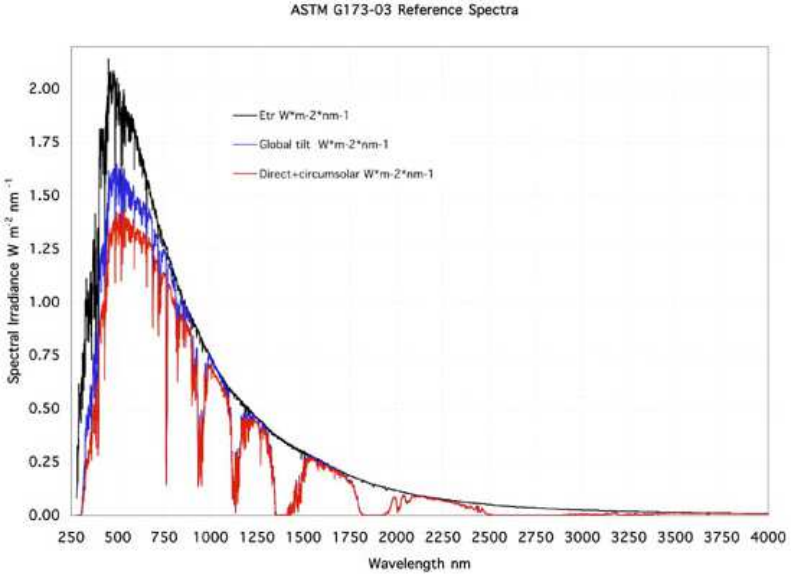

Figure 7: Extraterrestrial spectral irradiance (black line), Direct Normal Spectral Irradiance (blue line) and the Global Total Spectral Irradiance (red line) on a 37° sun facing tilted surface[27]. The red curve presents reduced values of spectral irradiance due to the absorption of O_2, H_2O, CO_2 and other molecules that comprise the atmosphere.

Sunlight at the earth's surface is categorized as ultraviolet light (UV, λ<400nm), infrared light (IR, λ>700nm) and visible light (vis., between 400 and 700nm). UV, IR and vis. constitute approximatively 4%, 54% and 42% respectively of the solar spectral irradiance (fig. 7)[27]. A semiconductor that absorbs the UV light uses less than 4% of the sunlight. To be more attractive, a semiconductor must have a band gap that does not exceed the value of 3,1 eV corresponding to 400nm.

Semiconductors with a too low flat band potential or a too small band gap require a bias voltage or a second semiconductor with a redox shuttle – a molecule that can be reversibly oxidized and reduced – to drive the reaction (fig. 8).

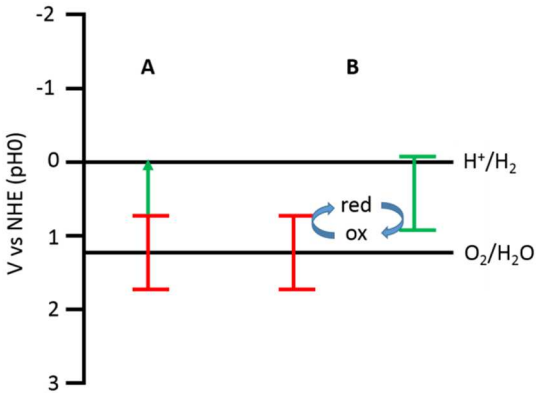

Figure 8: Energy diagram for water splitting with a semiconductor (red lines). The reaction requires A) a bias voltage (green arrow) or B) a second semiconductor (green lines) with a redox shuttle.

Literature often relates the case B in fig. 8, as a Z-scheme process[24-26,28]. In this process, each semiconductor can be tuned. One of the two semiconductors plays the role of the anode (water oxidation), the other deals with the water reduction. In some cases, Z-scheme water splitting proceeds even in the absence of reversible redox shuttles because of the interparticle electron transfer during the physical contact between both photocatalysts: the hydrogen and oxygen evolution photocatalysts[28].

3.1 Reported semiconductors

In the 1970s, Fujishima and Honda demonstrated that a cell consisting of a TiO_2 (Rutile) anode and a Pt cathode allows the photolysis of water[29]. Even if this compound offers excellent stability, TiO_2 possesses a semiconductor band gap energy around 3,2 eV. Due to this high value, this semiconductor cannot harvest a significant portion of the solar spectrum. Its potential solar-to-hydrogen conversion efficiency is very low (less than 2%)[30]. The efficiency of a cell is calculated from the net power density gained (in nW/cm^2) versus the power density

of the light (in mW/cm²) that illuminates the cell. The gain is the product of the voltage difference between the working electrode and the counter electrode and the current density[31].

Since 1972, many groups develop new materials for photo-water splitting. The band structure of tested semiconductors can be easily found in the literature[24,25,28,32] (fig. 9).

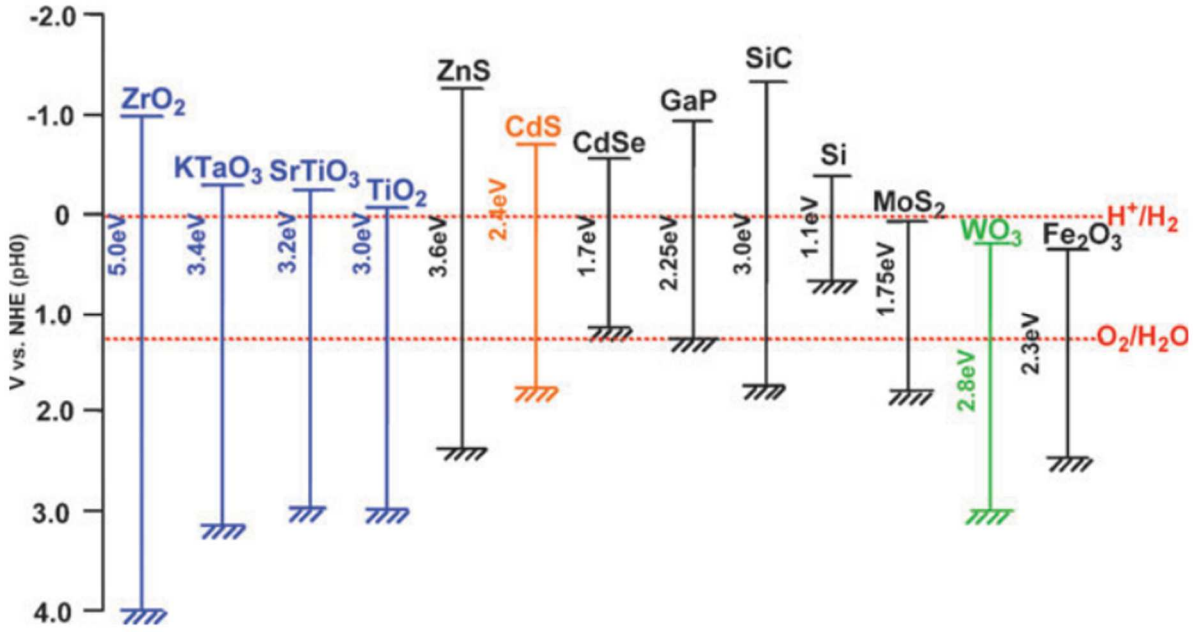

Figure 9: The relationship between the redox potentials of water splitting and the band structure of studied semiconductors[24].

Light absorption	photocatalyst	BG (eV)	Water splitting reaction
UV	$KTaO_3$	3,4	Water reduction + oxidation
	SiC	3,0	Water reduction + oxidation
	$SrTiO_3$	3,2	Water reduction + oxidation
	Ta_2O_5	3,9	Water reduction + oxidation
	TiO_2	3,0	Water reduction + oxidation
	ZnS	3,6	Water reduction + oxidation
	ZrO_2	5	Water reduction + oxidation
visible	CdS	2,4	Water reduction + oxidation
	CdSe	1,7	Water reduction
	GaP	2,3	Water reduction
	Si	1,1	Water reduction
	Fe_2O_3	2,3	Water oxidation
	MoS_2	1,8	Water oxidation
	WO_3	2,8	Water oxidation

Table 1: Photocatalysts and their application fields

The band gap reported for TiO_2 varies from 3,0eV (fig. 9[24,33]) to 3,3eV[34]. This can be attributed to several reasons. First, TiO_2 crystallizes in different crystal structures: rutile, anatase and brookite. A variation in the crystal structure implies a variation in the band structure of the material[24]. Furthermore, depending on the technique used to determine the band gap, the values can be slightly different for a same crystal structure: e.g. photoemission spectroscopy (PES) and inverse photoemission spectroscopy (IPES) give a value of 3,3 ± 0,5 eV[34] for the rutile electronic band gap. The rutile optical band gap, determined by Diffuse Reflectance Spectroscopy (DRS), is equal to 3,0 eV[33]. In this work, we consider the optical band gap determined by DRS.

According to the fig. 9, TiO_2 is a suitable material for overall water splitting – its valence band and its conduction band are located on either side of the water oxidation and reduction level. A few other materials have the same characteristic: ZrO_2, $KTaO_3$, $SrTiO_3$, ZnS, CdS and SiC. All these compounds, except CdS, only work using UV light due to their large band gap (tab. 1). Even if the band position seems perfect for water splitting, as in the CdS case, this material is not active due to photocorrosion[24]. Photocorrosion is the reaction where photogenerated holes react with the material (eq. 8) instead of reacting with water (eq. 4).

$$CdS + 2h^+ \rightarrow Cd^{2+} + S$$ *Equation 8: Photocorrosion of CdS*

Water reduction may occur, using visible light for CdSe, GaP and Si. Some groups try to allow the overall water splitting by, conceptually, broadening the band gap of these compounds. Instead of using CdSe, CdS is substituted. Sulfur, instead of selenium, gives a larger band gap for CdS than CdSe. In CdS, the band position seems perfect but the material presents the fore mentioned photocorrosion problems. The conceptual change of phosphor with nitrogen in GaP gives GaN. This material is studied by Maeda and co-workers[35-37] and its maximal efficiency is equal to 2,5%[26]. According to the same concept, SiC is imagined from Si. SiC is studied by Hao[38].

Although MoS_2 has a band structure fitting with water oxidation, Chorkendorff and his group show that the un-coordinated S atoms at the edges of MoS_2 nanoparticles have an important water reduction activity but no dioxygen production[25,39-41]. This material is mainly used as a co-catalyst in combination with water oxidation catalyst through the construction of Z-scheme photocatalyst systems.

Oxygen-deficient metal oxides, like WO_3 and Fe_2O_3 show enhanced activities for water oxidation due to an improved separation of their electron-hole pairs[25]. These semiconductors are frequently used in Z-scheme photocatalyst systems.

Hematite (Fe_2O_3) is a semiconductor studied in our laboratory for water oxidation[42]. Hematite absorbs visible light and according to its energy band diagram (fig. 9), this material is suitable only for water oxidation. It is assumed that a broadening of its band gap, even if it moves its light absorption towards a UV wavelength, may allow an overall water splitting reaction by changing the position of the conduction band.

The valence band of photocatalysts consist of p orbitals: O 2p for oxide, N 2p for nitride, S 3p for sulfide. d or sp orbitals usually comprise the conduction band of these semiconductors[24]. The position of the conduction and the valence band can be modified by atom substitution or the use of a dopant. A huge field of water splitting research focuses on band engineering.

This thesis is about yttrium orthoferrite ($YFeO_3$), a compound quite similar to hematite where, conceptually, one of the two iron atoms is substituted by an yttrium atom. Metal substitution will change the orbital that composes the conduction band. The conduction band of $YFeO_3$ may come closer or even exceed the water reduction potential compared to that of hematite.

3.2 Orthorhombic $YFeO_3$, the studied semiconductor

To our knowledge, $YFeO_3$ was never mentioned in the literature for being a suitable semiconductor for water splitting application but it is already registered as a photocatalyst for CO oxidation[43] and degradation of various compounds[44-47]. While the band structure of $YFeO_3$ is not well described, iron atoms, as in Fe_2O_3, occupy octahedral sites and its band gap slightly broader than that of Fe_2O_3[48], makes it an attractive candidate for water splitting using visible light.

Geller et al describe $YFeO_3$ for the first time in 1956[49]. This compound has a distorted perovskite structure composed by three kinds of atoms corresponding to ABO_3 formula[50]. Ideal perovskite has a cubic crystal structure (fig. 10 a)) but due to a difference in the atomic radius, 1,26 and 0,893 Å for iron and yttrium respectively, $YFeO_3$ is orthorhombic (fig. 10 b)).

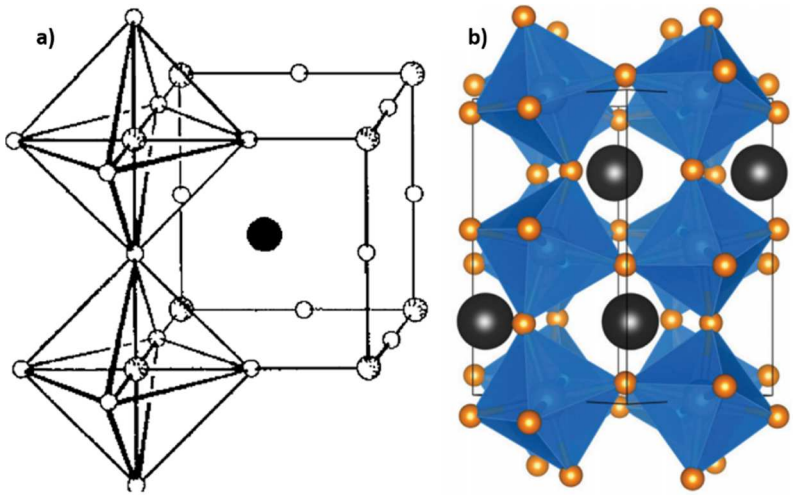

Figure 10: Ideal cubic[50] (a) and distorted (orthorhombic YFeO3)[51](b) perovskite structures. The A site cations are displayed as black spheres. They are localized in the cavity made by the FeO_6 octahedron.

This distortion changes the degenerated orbital on which electrons are positioned. If the system is not distorted electrons are mainly positioned on z^2 orbital. The distortion moves them to x^2-y^2, changing the energy level of the valence and conducting bands.

Based on the reported electronic properties, o-$YFeO_3$ seems to be a promising water splitting photocatalyst, especially for water oxidation, the reaction occurring at the photoanode.

3.3 Requirements

The synthetized material must meet few important criteria:

* The crystallinity of $YFeO_3$ will define the charge carrier's mobility. The material must be crystallized in an orthorhombic phase and contain as little amorphous phase as possible.

* A soft chemistry route is favored with a low thermal treatment to avoid the melting of the glass substrate.

* The main part of this work uses water as a solvent and environmental friendly reactants.

* To increase the number of catalytic sites and the contact with water in the water splitting cell, $YFeO_3$ must be porous and present a high specific surface.

* The yttrium orthoferrite thin film coating must be adherent on a conductive glass substrate.

3.4 Objectives

The aim of this Ph.D. project is to develop a low temperature crystallization route, to explore wet deposition methods (dip-coating and ultrasonic spray pyrolysis), to obtain an adherent and crystallized coating of o-$YFeO_3$ and test the photocatalytic properties of this material for water splitting perspectives.

The first part of this work is devoted to the study of the synthesis of the purest orthorhombic yttrium orthoferrite powder. The second chapter relates the impact of organic compounds added during the synthesis on the improvement of crystallinity and calcination temperature of the o-$YFeO_3$ powder. Then, two wet deposition techniques were tested: dip-coating and ultrasonic spray pyrolysis in chapter 3 and 4 respectively. This thesis ends with our conclusion about the best tested method to obtain a coating of crystallized yttrium orthoferrite and with some ideas to continue this work.

4. Bibliography

1) United States Census bureau, *World Population*, www.census.gov, august **2015**

2) BP, *statistical review of world energy*, www.bp.com/statisticalreview, June **2015**

3) US Department of energy, *Total Primary Energy Consumption*, www.eia.gov, august **2015**

4) US Department of energy, *CO_2 emissions*, www.eia.gov, august **2015**

5) Linde, *Steam Reforming*, www.linde-engineering.com, **2004**

6) Iaquaniello G., Antonetti E., Cucchiella B., Palo E., Salladini A., Guarinoni A., Lainati A. and Basini L., *Natural Gas - Extraction to End Use*, InTech, **2012**, p.267-286

7) Chun Y.N., Kim S.C., *Production of Hydrogen-Rich Gas from Methane by Thermal Plasma Reform*, J. Air & Waste Manage. Assoc., **2007**, Vol. 57, Iss. 12, p. 1447-1451

8) IEA, ETSAP, *Syngas Production from Coal*, www.etsap.org, **2010**

9) The Department of Chemistry at the University of Illinois, *Electrolysis of water using an electrical current*, www.chem.uiuc.edu, **2009**

10) Yürüm Y., *Hydrogen production from Non-fossil Hydrocarbon sources*, Hydrogen Energy System: Production and Utilization of Hydrogen and Future Aspects, **1994**, p. 24-25

11) Praxair, *Buy Compressed Hydrogen Gas or Liquid Hydrogen (H_2)*, www.praxair.com, **2015**

12) Azzouz A., *Achievement in hydrogen storage on adsorbents with high surface-to-bulk ratio - Prospects for Si-containing matrices*, Int. J. Hydrogen Energy, **2012**, Vol. 37, p. 5032-5049

13) Goldsmith J., Wong-Foy A.G., Cafarella M.J. and Siegel D.J., *Theoretical Limits of Hydrogen Storage in Metal−Organic Frameworks: Opportunities and Trade-Offs*, Chem. Mater., **2013**, Vol. 25, Iss. 16, p. 3373–3382

14) Avtar Jat R., Singh R., Parida S.C., Das A., Agarwal R., Mukerjee S.K., Ramakumar K.L., *Structural and hydrogen isotope storage properties of Zr–Co–Fe alloy*, Int. J. Hydrogen Energy, **2015**, Vol. 40, Iss. 15, p.5135-5143

15) Silambarasan D., Surya V.J., Vasu V. and Iyakutti K., *Single Walled Carbon Nanotube–Metal Oxide Nanocomposites for Reversible and Reproducible Storage of Hydrogen*, Appl. Mater. Interfaces, **2013**, Vol. 5, Iss. 21, p. 11419–11426

16) Millet P., *Hydrogen storage in hydride-forming materials*, Advances in Hydrogen Production, Storage and Distribution, **2014**, p. 368-409

17) Cormier T.E. et al., *Process for producing ultra-high purity oxygen*, US Patent, **1986**, Patent n° 4,615,716

18) Air products, *solution d'oxygène*, www.airproducts.be, **2009**

19) Rifair, *Processus de production d'oxygène*, www.rifair.fr, **2012**

20) Friesen R.M., Raber M.B., Reimer D.H., *Oxygen concentrators: a primary oxygen supply source*, Can. J. Anesth., **1999**, Vol. 46, Iss. 12, p. 1185-1190

21) Pure Energy Centre, *oxygen storage*, http://pureenergycentre.com, **2015**

22) Air products, *liquid oxygen*, www.airproducts.com, **2013**

23) Gilleßen M., Lumeij M., George J., Stoffel R., Motohashi T., Kikkawa S. and Dronskowskiet R., *Oxygen-Storage Materials $BaYMn_2O_{5+\delta}$ from the Quantum-Chemical Point of View*, Chem. Mater., **2012**, Vol. 24, p. 1910−1916

24) Kudo A., Miseki Y., *Heterogeneous photocatalyst materials for water splitting*, Chem. Soc. Rev., **2009**, Vol. 38, p. 253-278

25) Xin L., Jiaguo Y., Jingxiang L., Yueping F., Jing X. and Xiaobo C., *Engineering heterogeneous semiconductors for solar water splitting*, J. Mater. Chem. A, **2015**, Vol. 3, p. 2485–2534

26) Osterloh F.E., *Inorganic materials as catalysts for photochemical splitting of water*, Chem. Mater., **2008**, Vol. 20, p. 35-54

27) American Society for Testing and Materials, *Terrestrial Reference Spectra for Photovoltaic Performance Evaluation, Reference Solar Spectral Irradiance: Air Mass 1.5*, http://rredc.nrel.gov/solar/spectra/am1.5/, **2015**

28) Hisatomi T., Kubota J. and Domen K., *Recent advances in semiconductors for photocatalytic and photoelectrochemical water splitting* , Chem. Soc. Rev., **2014**, Vol. 43, p. 7520—7535

29) Fujishima A., Honda K., Electrochemical photolysis of water at a semiconductor electrode, Nature, **1972**, Vol. 238, p. 37-39

30) Prévot M.S. and Sivula K., *Photoelectrochemical Tandem Cells for Solar Water Splitting*, J. Phys. Chem. C, **2013**, Vol. 117, p. 17879−17893

31) Heller A., Vadimsky R.G., *Efficient Solar to Chemical Conversion: 12% Efficient Photoassisted Electrolysis in the [p-type InP(Ru)]/HCl-KCl/Pt(Rh) Cell*, Phys. Rev. Lett., **1981**, Vol. 46, Iss. 17, p. 1153-1156

32) Zhang H., Chen G., Bahnemann D.W., *Photoelectrocatalytic materials for environmental applications*, J. Mater. Chem., **2009**, p. 5089-5121

33) Amtout A. and Leonelli R., *Optical properties of rutile near its fundamental band gap*, Phys. Rev. B, **1995**, Vol. 51, Iss. 11, p. 6842

34) Tezuka Y., Shin S., Lshii T., Ejima T., Suzuki S. and Sato S., *Photoemission and Bremsstrahlung Isochromat Spectroscopy Studies of TiO_2 (Rutile) and $SrTiO_3$*, J. Phys. Soc. Jpn., **1994**, Vol. 63, p. 347

35) Maeda K., Teramura K., Lu D., Takata T., Saito N., Inoue Y. and Domen K., *Photocatalyst releasing hydrogen from water*, Nature, **2006**, Vol. 440, p. 295

36) Maeda K., Takata T., Hara M., Saito N., Inoue Y., Kobayashi H. and Domen K., *GaN:ZnO Solid Solution as a Photocatalyst for Visible-Light-Driven Overall Water Splitting*, J. Am. Chem. Soc., **2005**, Vol. 127, p. 8286–8287

37) Maeda K., Teramura K., Saito N., Inoue Y. and Domen K., *Improvement of photocatalytic activity of $(Ga_{1-x}Zn_x)(N_{1-x}O_x)$ solid solution for overall water splitting by co-loading Cr and another transition metal*, J. Catal., **2006**, Vol. 243, p. 303–308

38) Hao J.-Y., Wang Y.-Y., Tong X.-L., Jin G.-Q. and Guo X.-Y., *Photocatalytic hydrogen production over modified SiC nanowires under visible light irradiation*, Int. J. Hydrogen Energy, **2012**, Vol. 37, p. 15038–15044

39) Vrubel H., Merki D. and Hu X., *Hydrogen evolution catalyzed by MoS_3 and MoS_2 particles*, Energy Environ. Sci., **2012**, Vol. 5, p. 6136–6144

40) Jaramillo T.F., Jorgensen K.P., Bonde J., Nielsen J.H., Horch S. and Chorkendorff I., *Identification of Active Edge Sites for Electrochemical H_2 Evolution from MoS_2 Nanocatalysts*, Science, **2007**, Vol. 317, p. 100–102

41) Hinnemann B., Moses P.G., Bonde J., Jorgensen K.P., Nielsen J.H., Horch S., Chorkendorff I. and Norskov J.K., *Biomimetic Hydrogen Evolution: MoS_2 Nanoparticles as Catalyst for Hydrogen Evolution*, J. Am. Chem. Soc., **2005**, Vol. 127, p. 5308–5309

42) Toussaint C., Tran H.L.L., Colson P., Dewalque J., Vertruyen B., Gilbert B., Nguyen N.D., Cloots R. and Henrist C., *Combining Mesoporosity and Ti-Doping in Hematite Films for Water Splitting*, J. Phys. Chem. C, **2015**, vol.119, p.1642−1650

43) Li J., Singh U.G., Schladt T.D., Stalick J.K., Scott S.L. and Seshadri R., *Hexagonal $YFe_{1-x}Pd_xO_{3-\delta}$: nonperovskite host compounds for Pd^{2+} and their catalytic activity for CO oxidation*, Chem. Mater., **2008**, Vol. 20, p. 6567–6576

44) Wang W, Li S., Wen Y., Gong M., Zhang L., Yao Y., Chen Y., *Synthesis and characterization of $TiO_2/YFeO_3$ and its photocatalytic oxidation of gaseous benzene*, Acta Phys. Chim. Sin., **2008**, Vol. 24, p. 1761–1766

45) Tang P., Chen H., Cao F., Pan G., *Magnetically recoverable and visible-light-driven nanocrystalline $YFeO_3$ photocatalysts*, Catalysis Science and Technology, **2011**,Vol. 1, p.1145–1148

46) Lü X., Xie J., Shu H., Liu J., Yin C., Lin J., *Microwave-assisted synthesis of nanocrystalline $YFeO_3$ and study of its photoactivity*, Mater. Sci. Eng., B, **2007**, Vol. 138, p. 289–92

47) Wu L., Yu J.C., Zhang L., Wang X., Li S., *Selective self-propagating combustion synthesis of hexagonal and orthorhombic nanocrystalline yttrium iron oxide*, J. Solid State Chem., **2004**, Vol. 177, p. 3666–3674

48) Butler M.A., Ginley D.S., Photoelectrolysis with $YFeO_3$ electrodes., J. Appl. Phys., **1977**, Vol. 48, p. 3070–3072

49) Geller S. and Wood E.A., *Crystallographic studies of perovskite-like compounds. I. Rare earth orthoferrites and $YFeO_3$, $YCrO_3$, $YAlO_3$*, Acta Crystallogr., **1956**, Vol. 9, p. 563-568

50) Li C.H., Soh K.C.K., Wu P., *Formability of ABO_3 perovskites*, J. Alloys Compd., **2004**, Vol. 372, p. 40–48

51) Misch L.M., Birkel A., Figg C.A., Fors B.P., Hawker C.J., Stucky G.D., Seshadri R., *Rapid microwave-assisted sol–gel preparation of Pd-substituted $LnFeO_3$ (Ln = Y, La): phase formation and catalytic activity*, Dalton Trans., **2014**, Vol. 43, p. 2079-2087

Chapter 1: Yttrium orthoferrite powder: Precursor selection

This second chapter, is mainly based on a paper that is already published[1] and will explore the best synthesis methods to obtain the purest orthorhombic yttrium orthoferrite.

Many synthesis methods for orthorhombic $YFeO_3$ have been reported: sol–gel[2-5], microwave-assisted[6,7], self-propagating combustion synthesis[8], solid state reaction[9], alkoxide method[10], sonochemical synthesis[11], pulsed laser deposition[12], etc. Our target is to coat this compound onto a substrate. We have selected the synthesis method based on a liquid route because we plan to coat the substrate with a precursor solution before heating the samples to finally obtain the desired composite material.

1.1 Synthesis protocols for powders

Two kinds of precursor solutions are explored: the "chloride route" and the "nitrate route". These two routes start from a liquid phase – the precursor – and finally produce a powder. These powders allow us to study the purity of the final compound.

1.1.1 Chlorides route

For this synthesis, we mix 50 ml of $FeCl_3$ 0.1 M in ethanol and 50 ml of YCl_3 0.1 M in ethanol. These solutions were prepared by dissolving $FeCl_3.6H_2O$ and $YCl_3.6H_2O$ in absolute ethanol respectively. The mixture is stirred overnight before adding ammonium hydroxide (NH_4OH) to reach a pH of 7. The sample is heated at 60°C for 10 hrs to evaporate the liquid phase obtaining an orange paste. This paste is then transferred to a furnace with a heating ramp of 300°C/h, and is heated up to a fixed temperature. The resulting brown solid is then ground and analyzed. This sample is named "Cl."

1.1.2 Nitrates route

20 ml of $Fe(NO_3)_3$ 0.1 M (fig. 1.1a) and 20 ml solution of $Y(NO_3)_3$ 0.1 M (fig. 1.1b) were prepared by dissolving $Fe(NO_3)_3.9H_2O$ and $Y(NO_3)_3.6H_2O$ in de-ionized water, respectively. These two solutions are mixed and stirred overnight (fig. 1.1c). Ammonium hydroxide (NH_4OH) was added to reach a pH of 7 (fig. 1.1d). The mixture is heated at 60°C overnight to obtain a brown gel (fig. 1.1e). Then the gel is heated at 450°C, 650°C or 850°C. Every temperature was reached with a heating ramp of 300°C/h and was then maintained for 2 hrs. The resulting fluffy brown solid (fig. 1.1f) is then ground prior to characterization. This sample is named "N".

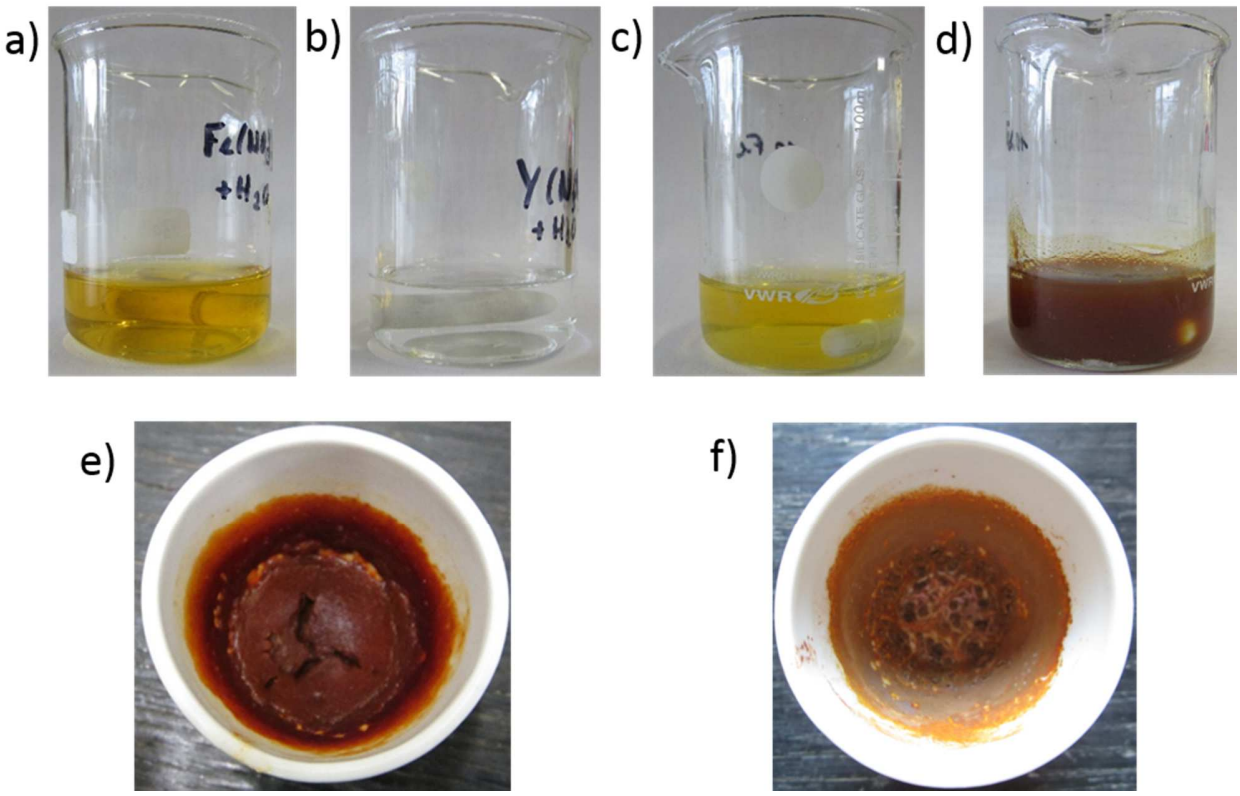

Figure 1.1: Solutions of (a) iron nitrate, (b) yttrium nitrate, (c) mixed iron and yttrium nitrate and (d) mixed iron and yttrium nitrate basified to pH 7. The mixture of iron and yttrium nitrate at pH 7 was treated at (e) 60°C overnight (gel) and (f) 850°C for 2hrs (powder).

1.2 Study of sample

This section treats the subject of the purity and homogeneity of our compound at different steps of the synthesis. The crystallization and optical band gap are also investigated in order to estimate their usefulness for future applications.

1.2.1 Mass analysis of the precursors

A problem that could be encountered during the synthesis is the strong hygroscopy of the precursors. This property could lead to an overestimation of the number of moles of iron or yttrium that will actually react.

The solid precursors are weighed before and after heat treatment to quantify the proportion of water in the initial powder. Samples are heated very slowly to prevent ebullition and a loss of compound: 60°C overnight, then 100°C during 10 hours and finally heated to 850°C at a ramp speed of 100°C per hour that is maintained at 850°C for two hours. They are heated to such a high temperature to ensure full oxidization: Yttrium nitrate produces Y_2O_3[13] (eq. 1.1) and iron nitrate produces Fe_2O_3 [14] (eq. 1.2).

$$4\,Y(NO_3)_3.6H_2O \xrightarrow{\Delta} 2Y_2O_{3\,(s)} + 6N_2O_{5\,(g)} + 24H_2O_{\,(g)} \qquad \textit{Equation 1.1}$$

$$2\,Fe(NO_3)_3.9H_2O \xrightarrow{\Delta} Fe_2O_{3\,(s)} + 3N_2O_{5\,(g)} + 18H_2O_{\,(g)} \qquad \textit{Equation 1.2}$$

This study is only performed on the nitrate precursor sample because of the higher impurity content of chlorinated precursor (see X-ray diffraction study: fig. 1.6). The result of the thermal analysis is presented in tab. 1.1.

Table 1.1: Thermogravimetric analysis of the water content in the Iron Nitrate and Yttrium Nitrate reactants.

Expected formula	Weighed nitrate mass at RT (g)	Weighed mass after heating (g)	Expected Mass loss (g)	Error on mass (%)	Calculated stoichiometry
$Y(NO_3)_3.6H_2O$	0,6358	0,1872	0,4479	0,16 %	$Y(NO_3)_3.6{,}03H_2O$
$Fe(NO_3)_3.9H_2O$	0,5714	0,1098	0,4458	3,42 %	$Fe(NO_3)_3.9{,}65H_2O$

The iron nitrate, more than the yttrium nitrate, contains a quantity of supplementary water. The weighed compound possesses less iron than expected. Therefore, for all the following experiments and analysis containing nitrate precursor samples, it has to be kept in mind that there is a deficiency of iron in our samples.

1.2.2 pH monitoring

During the synthesis, the solution must reach a pH of 7. This is obtained by adding ammonium hydroxide (NH_4OH) and the pH evolution progresses in different steps (fig. 1.2). Indeed, Fe^{3+} is a weak acid characterized by a pKa value of 2.2 at 25°C. This acidic form must, in a first time, be transformed in $Fe(OH)^{2+}$ before precipitating out as the $Fe(OH)_3$ form. The solubility products of iron hydroxide ($K_{PS}(Fe(OH)_3) = 4.10^{-38}M^4$) and of yttrium hydroxide ($K_{PS}(Y(OH)_3) = 10^{-22}M^4$) have widely differing values. Therefore the probability of having a coprecipitation is quite low, which could lead to an inhomogeneous repartition of cations in the obtained gel.

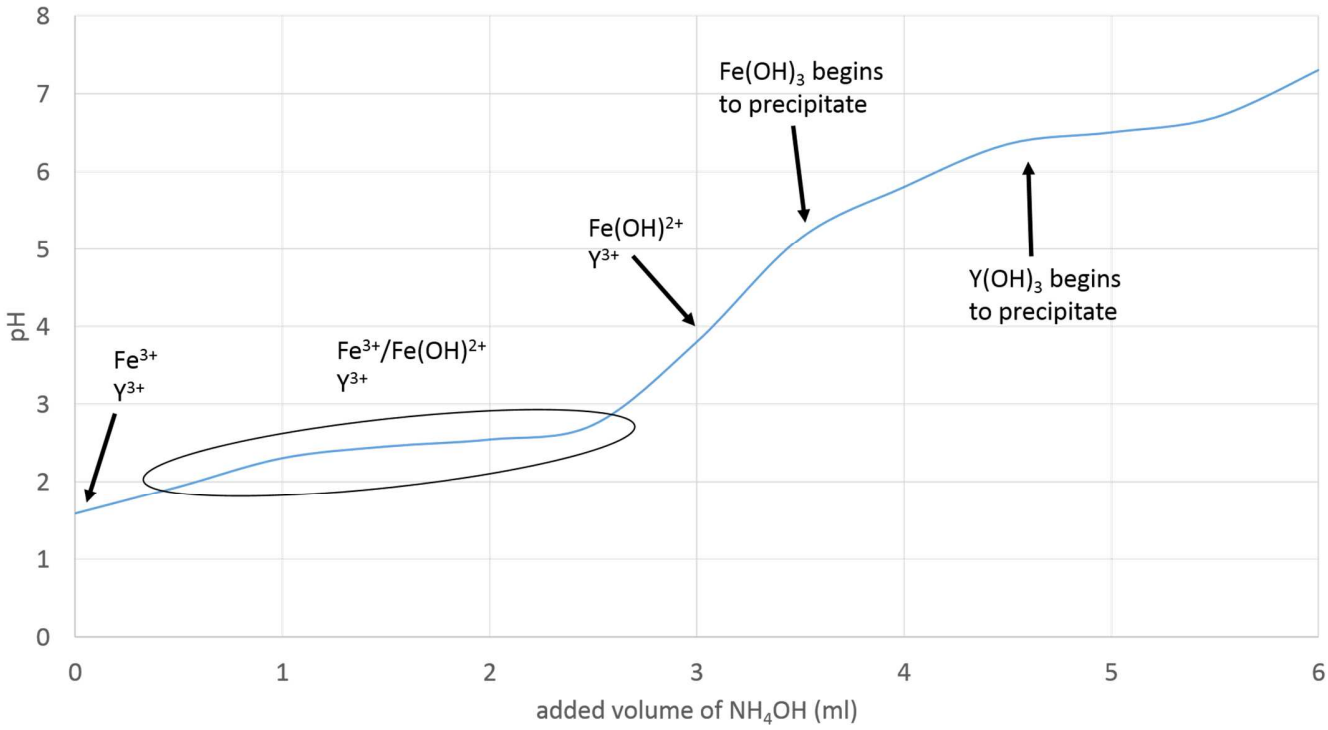

Figure 1.2: The pH evolution of a 50 mL solution based on a nitrate precursor ($[Y^{3+}]=[Fe^{3+}]=0,1M$) dependant on the added volume of NH_4OH 2,5M.

The volume of added ammonium hydroxide (NH_4OH) 2,5M, in the particular case of a 50 mL solution based on nitrate precursor ($[Y^{3+}]=[Fe^{3+}]=0,1M$) (fig. 1.2), is more or less equal to 1ml between the beginning of the precipitation of iron hydroxide and the precipitation of yttrium hydroxide. This difference in the added volume induces an inhomogeneous coprecipitation.

1.2.3 Phase composition

The synthesis process progressively basifies the mixture, adding hydroxide to the iron and yttrium cations (eq. 1.3 and 1.4).

$$Fe^{3+} + 3OH^- \leftrightarrows Fe(OH)_3 \qquad pK_{PS} = 37 \qquad \text{Equation 1.3}$$

$$Y^{3+} + 3OH^- \leftrightarrows Y(OH)_3 \qquad pK_{PS} = 22 \qquad \text{Equation 1.4}$$

The solubility products differ between iron and yttrium hydroxides, so that precipitation begins at different hydroxide concentration, the iron hydroxide precipitating before yttrium hydroxide. When yttrium hydroxide begins to precipitate, the quantity of unprecipitated iron is lower than unprecipitated yttrium. The

solid compound formed from this point contains less iron than yttrium, leading to an inhomogeneity and a stoichiometric ratio Y:Fe not equal to 1:1 in the solid phase.

1.2.4 Crystallinity

X-ray diffraction will provide information on the kind of compounds that are crystalized in our sample when they are heated at various temperatures.

The orthorhombic $YFeO_3$ (o-$YFeO_3$) phase has 4 main peaks at 2Θ = 32°; 33,1° (the more intense); 33,8° and 34,1° ($YFeO_3$, PDF 04-010-6423, fig. 1.3). The two peaks at 33,8° and 34,1° generally overlap. Consequently, we consider the presence of this phase when 3 peaks (~32°, ~33° and ~34°) are observed. The peaks belonging to this phase will be mentioned on the diffractogram with the "∗" symbol.

Another compound has nearly the same diffractogram, especially when we focus on the 2Θ region between 30° and 35°. Indeed, yttrium iron garnet (YIG), the orthorhombic $Y_3Fe_5O_{12}$ (PDF 00-021-1450) (fig. 1.3) compound possesses 3 peaks localized at 32,1°; 33,2° and 34°. But the synthesis conditions[15] and the proportions of precursors to obtain such a compound differ from our synthesis process. The orthorhombic $Y_3Fe_5O_{12}$ is absent from all of our samples. Indeed, this compound contains more iron than yttrium and according to our previous mass analysis we have concluded that iron could not be in a sufficient quantity for the compound to form. In addition, this compound only appears at high pressures (20kbar) and we work at ambient pressure (~1bar). Furthermore, energy-dispersive X-ray spectroscopy (EDX) results in an elemental ratio Y:Fe of between 1,05 and 1,13. These values are closer to 1, corresponding to $YFeO_3$, as opposed to 0,6, which would then indicate $Y_3Fe_5O_{12}$.

The hexagonal $YFeO_3$ (h-$YFeO_3$) phase (PDF: 00-048-0529) possesses 2 main peaks at 2Θ = 30,4° and 33,2°. The first mentioned peak (30,4°) does not overlap with peaks from other yttrium orthoferrite compounds. Peaks belonging to this phase were not found in any of our powder diffractograms. We conclude that this phase (h-$YFeO_3$) of yttrium orthoferrite was not crystallized during the powder synthesis. In following chapters about film synthesis, the peaks belonging to this phase will be mentioned on the diffractogram with the "h" symbol.

Some other phases of similar compounds may appear on diffractograms as follows:

- Cubic Y_2O_3 (PDF: 04-005-4378, fig. 1.3): this has a peak situated at 2Θ = 29,3° that does not overlap with any peak of the o-$YFeO_3$. The peaks belonging to this phase will be mentioned on the diffractogram with the "+" symbol.

- Hematite, rhombohedric Fe_2O_3 (PDF 04-003-2900, fig. 1.3): this has a peak at 33,3° overlapping with the main peak of o-$YFeO_3$, and another one at 35,7° that is clearly different from the peaks belonging to o-$YFeO_3$. The peaks belonging to this phase will be mentioned on the diffractogram with the "H" symbol.

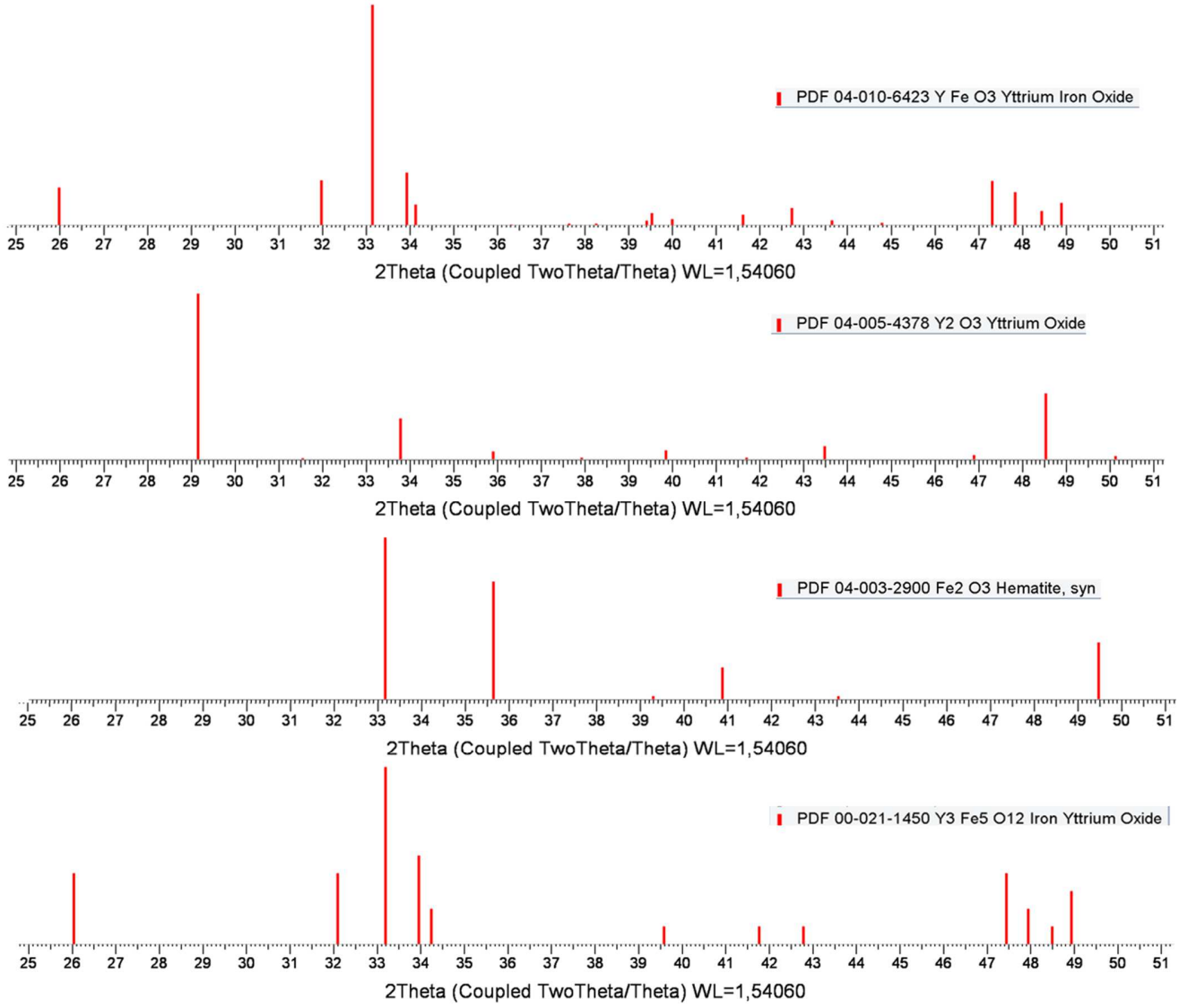

Figure 1.3: The position and relative intensity of diffractogram peaks within crystallized o-$YFeO_3$, Y_2O_3, Fe_2O_3 and o-$Y_3Fe_5O_{12}$.

The desired phase (o-$YFeO_3$) progressively crystallizes after 785°C for Cl samples (fig. 1.4). Unfortunately, even at 850°C some unwanted phases like yttrium oxide or hematite still remain in our sample.

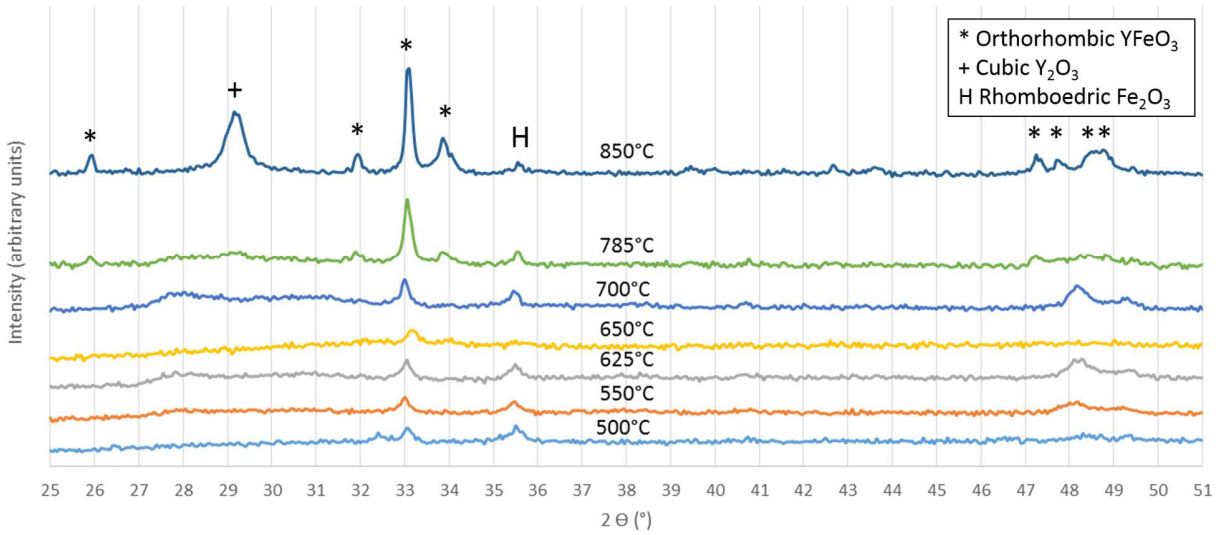

Figure 1.4: XRD patterns of Cl samples treated at various temperature. Referenced peaks correspond to PDF: 04-010-6423 for o-$YFeO_3$, PDF: 04-005-4378 for c-Y_2O_3 and PDF:04-003-2900 for r-Fe_2O_3.

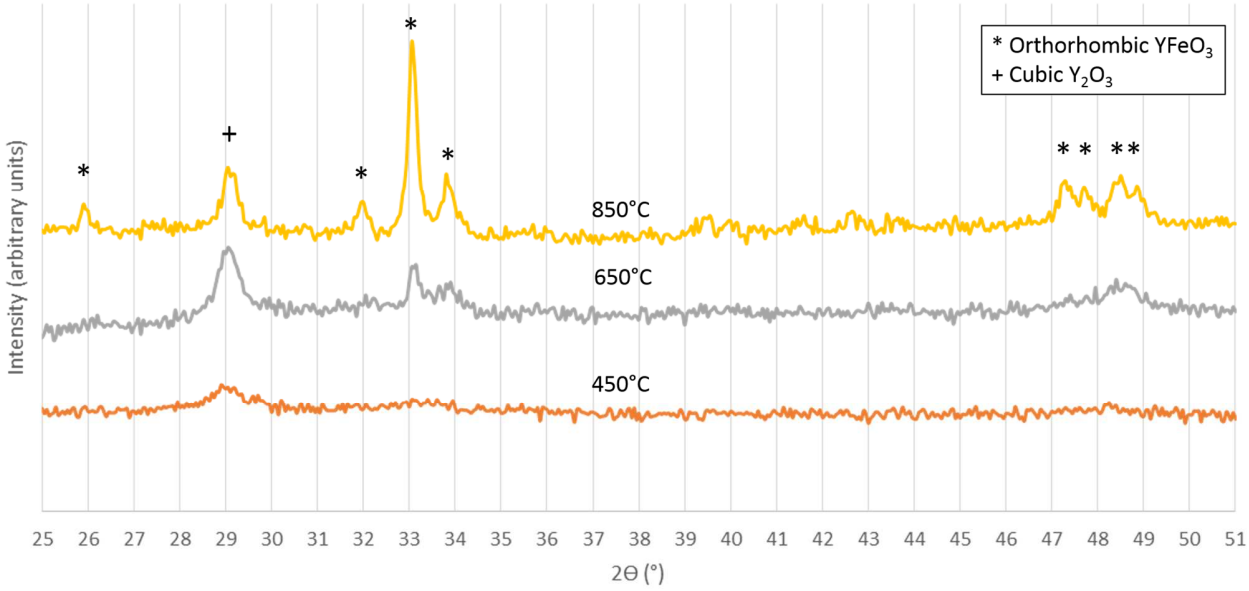

Figure 1.5: XRD patterns of N samples treated at various temperature. Referenced peaks correspond to PDF: 04-010-6423 for o-$YFeO_3$ and PDF: 04-005-4378 for c-Y_2O_3.

Yttrium orthoferrite crystallizes at 850°C when the starting precursors are nitrates. But in a similar manner to Cl samples, this compound is still not pure at 850°C. Indeed we can observe in fig. 1.5 the presence of Y_2O_3.

Yttrium oxide crystallizes in nearly all our samples. The low crystallization temperature (280°C)[16] of Y_2O_3 and the inhomogeneity of the gel before the heating treatment explains its presence.

The percentage of crystalline phases was estimated by using the Rietveld refinement within the TOPAS software, using the fundamental parameters approach to model the instrumental contribution[17]. The weight percentage of the different crystalline phases have been estimated by refining the scale factors and profile parameters using the cell parameters, atomic positions and occupation factors reported in references 04-010-6423 ($YFeO_3$), 04-005-4378 (Y_2O_3) and 04-003-2900 (Fe_2O_3) of the PDF-4+ database (International Center for Diffraction Data).

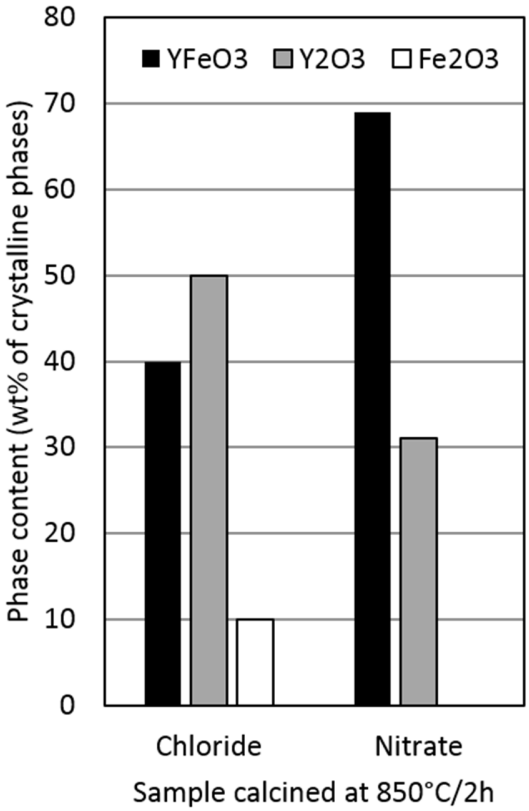

Figure 1.6: Influence of the precursor on the phase content ($YFeO_3$, Y_2O_3 and Fe_2O_3) for samples calcinated at 850°C for 2h.

In fig. 1.6, the nitrate route (N 850°C) shows a smaller peak characteristic of Y_2O_3 than that shown by the chloride route (Cl 850°C). Furthermore, iron oxide (Fe_2O_3) is not detected in N samples. As a means of comparison between the different synthesis routes, the phase content of crystallized $YFeO_3$, Y_2O_3 and Fe_2O_3 (fig. 1.6) was determined via TOPAS software. This confirms that the N route gives rise to a lower contamination by Y_2O_3 than that by the Cl route. Therefore all the future work will mainly focus on the nitrate precursors.

The average crystallite size (tab. 1.2) is estimated via Sherrer's formula[18] (eq. 1.5).

$$D = \frac{0{,}9\lambda}{\beta cos\theta} \qquad \text{Equation 1.5}$$

Where D is the average crystallite size in nm, λ = 0,15418nm, the wavelength of monochromatic radiation Cu K_α X-rays and β is the width of the diffraction peak at half maximum for the diffraction angle 2Θ, β is also often mentioned as FWHM (full width at half maximum).

Actually, there is also an instrumental contribution to the FWHM. In the present case, the instrumental resolution of the D8 diffractometer is such that the contribution of the crystallite size becomes small by comparison with the instrumental contribution for crystallite sizes above approx. 40 nm. In such cases the values obtained with the Scherrer formula will be given for information and a 'large crystallites' tag will be added as a comment.

Table 1.2: Average crystallite size in Cl and N samples calcined at 850°C

Sample	Average crystallite size (nm)
Cl 850°C	53 (large crystallites)
N 850°C	43 (large crystallites)

1.2.4 Morphology of the powders analyzed by electronic microscopy

Precursors also influence the morphology of the powders. The nitrate-based sample (N 850°C) seems, according to transmission electron microscopy (TEM) and scanning electron microscopy (SEM) images (fig. 1.7c and 1.7d), to be more porous than the chloride-based one (Cl 850°C) (fig. 1.7a and 1.7b).

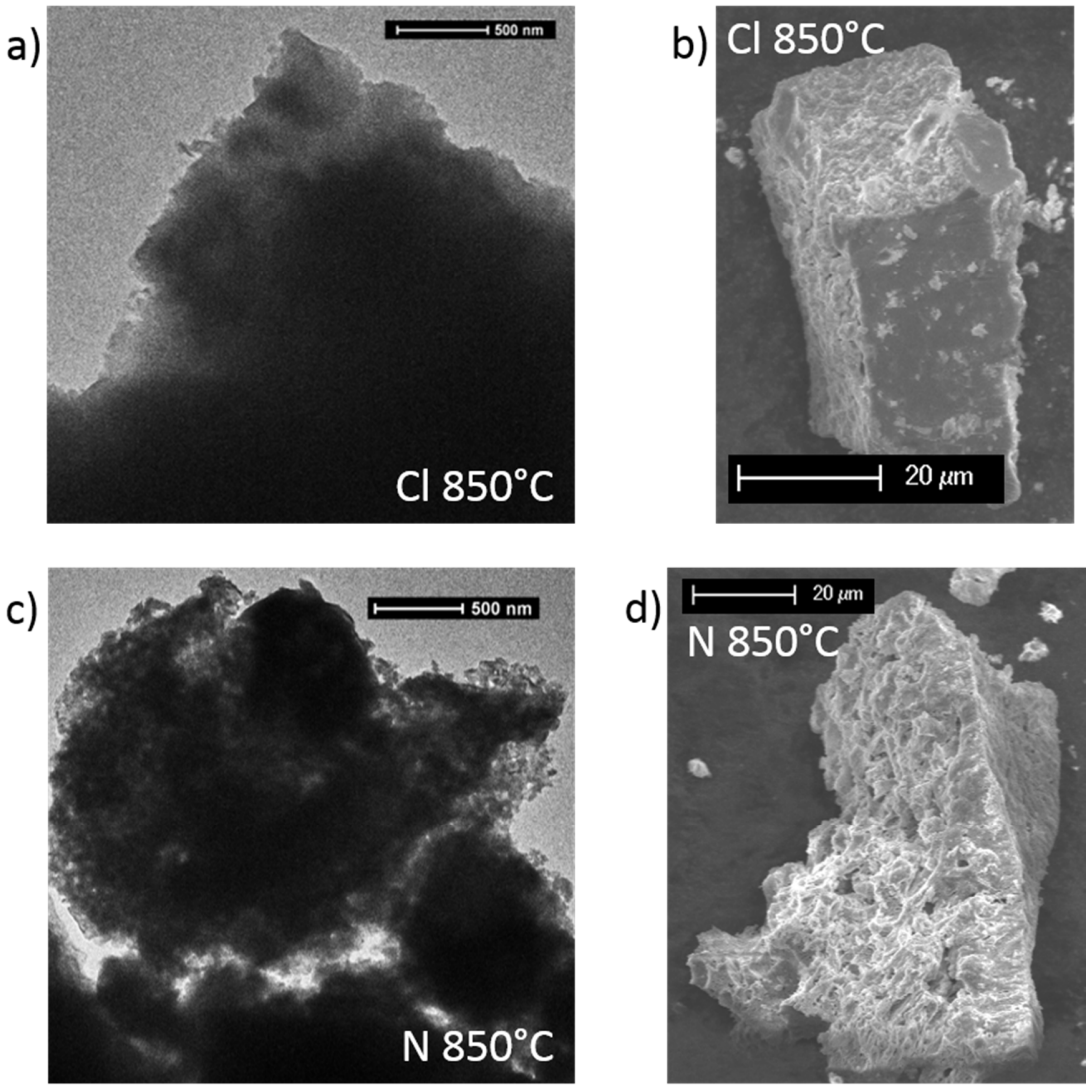

Figure 1.7: TEM (a) and SEM (b) images of powders obtained by the chloride route and TEM (c) and SEM (d) images of powders from the nitrate route.

Sometimes, during the nitrate route, self-ignition is observed and high quantities of gases are evolved in a short period of time (see eq. 1.1 and 1.2). The sudden decomposition of nitrate ions into nitrogen oxides and water is exothermic[19] and locally causes a strong increase of temperature favoring the crystallization of the desired compound. This also results in the formation of numerous pores in the final mixed oxide particles, giving them the structure of ashes with a high specific surface area. This reaction is even more intense when organic acids are added, thanks to their role as organic combustion agents (see Influence of additives).

As we plan to use this compound as a catalyst, a higher porosity is an advantage. We estimate that this will be an active surface, reachable by the water in contact with the water splitting electrode. Indeed as gas evacuation creates accessible channels, all the surface of our compound will thus be in contact with the water.

1.2.5 Determination of optical band gap

The optical band gap of o-$YFeO_3$ obtained from the nitrate precursor, heated at 850°C for 2h was obtained via a Tauc Plot (fig. 1.8) derived from Diffuse Reflectance Spectroscopy (DRS) data and the Kubelka–Munk function (eq. 1.6) for an indirect band gap[20].

$$F(R_\infty) = \frac{(1-R_\infty)^2}{2R_\infty} \qquad \text{Equation 1.6}$$

Where R_∞ is the diffuse reflectance for an infinitely thick sample.

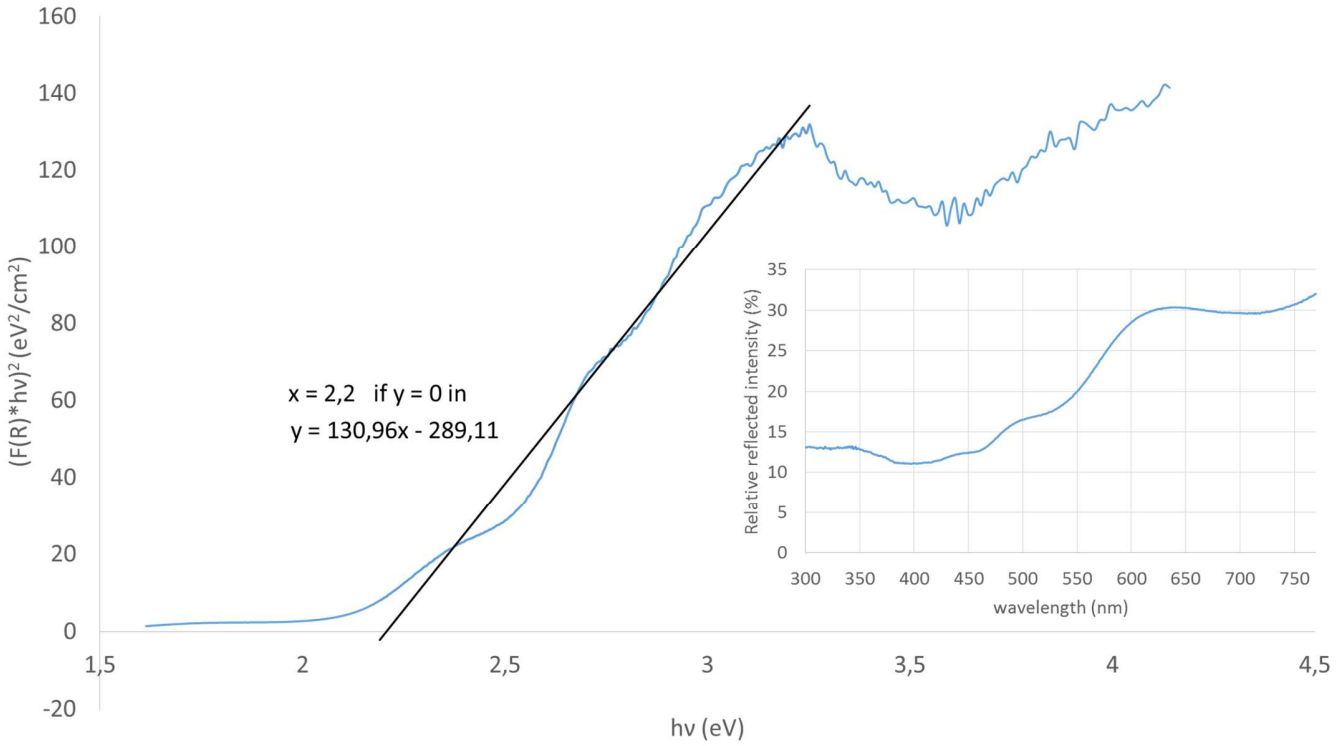

Figure 1.8: Determination of the optical band gap (2.2eV). This is the x value when y = 0 in the linear regression, via a Tauc plot obtained from diffuse reflectance spectroscopy (side view) for a sample prepared from a nitrate precursor heated at 850°C for 2h.

The obtained value is 2.2 eV (fig. 1.8), which is comparable to the value of 2.3 eV reported in the literature[3].

This band gap is suitable for visible-light water splitting photoanode purposes. Note that Y_2O_3 should be avoided for this application because its band gap is too large (5.5 eV[16]) to be efficient for visible light operation.

1.3 Conclusion

We tested two kind of precursors, chlorides and nitrates, to obtain orthorhombic yttrium orthoferrite. Even if we can encounter some problems during the coprecipitation of hydroxides, heating this gel at 850°C made us obtain the desired compound. Subsequent analysis shows that the best way to obtain the purest o-$YFeO_3$ is the synthesis based on a nitrate precursor. This compound, according to a Tauc plot, has a suitable band gap for a water splitting application. Furthermore, the specific surface area is bigger, according to SEM and TEM images, when comparing nitrate against chloride-based precursors that is a beneficial advantage for catalytic applications.

1.4 Bibliography

1) Stevens F., Cloots R., Poelman D., Vertruyen B., Henrist C., *Low temperature Orthoferrite by organic acid-assisted sol-gel synthesis*, Mater. Lett., **2014**; Vol. 114, p. 136-139.

2) Li J., Singh U. G., Schladt T. D., Stalick J. K., Scott S. L. and Seshadri R., *Hexagonal $YFe_{1-x}Pd_xO_{3-\delta}$: nonperovskite host compounds for Pd^{2+} and their catalytic activity for CO oxidation*, Chem. Mater., **2008**; Vol. 20, p. 6567–6576.

3) Wang W., Li S., Wen Y., Gong M., Zhang L., Yao Y., Chen Y., *Synthesis and characterization of $TiO_2/YFeO_3$ and its photocatalytic oxidation of gaseous benzene*, Acta Phys.-Chim. Sin., **2008**; Vol. 24, p.1761–1766.

4) Mathur S., Veith M., Rapalaviciute R., Shen H., Goya G. F., Martins Filho W. L. and Berquo T. S., *Molecule derived synthesis of nanocrystalline $YFeO_3$ and investigations on its weak ferromagnetic behavior*, Chem. Mater., **2004**; Vol. 16, p. 1906–1913.

5) Rajendran M., Bhattacharya A.K., *Nanocrystalline orthoferrite powders: synthesis and magnetic properties*, J. Eur. Ceram. Soc., **2006**; Vol. 26, p. 3675–3679.

6) Tang P., Chen H., Cao F., Pan G., *Magnetically recoverable and visible-light-driven nanocrystalline $YFeO_3$ photocatalysts*, Catal. Sci. Technol., **2011**; Vol. 1, p.1145–1148.

7) Lü X., Xie J., Shu H., Liu J., Yin C. and Lin J., *Microwave-assisted synthesis of nanocrystalline $YFeO_3$ and study of its photoactivity*, Mater. Sci. Eng., B, **2007**; Vol. 138, p. 289–292.

8) Wu L., Yu J. C., Zhang L., Wang X., Li S., *Selective self-propagating combustion synthesis of hexagonal and orthorhombic nanocrystalline yttrium iron oxide*, J. Solid State Chem., **2004**; Vol. 177, p.3666–3674.

9) Buscaglia V., Caracciolo F., Bottino C., Leoni M., Nanni P., *Reaction diffusion in the Y_2O_3–Fe_2O_3 system*, Acta Mater., **1997**; Vol. 45, p. 1213–1224

10) Taketomi S., Dai Z. R., Ohuchi F. S., *Electron diffraction of yttrium iron oxide nanocrystals prepared by the alkoxide method*, J. Magn. Magn. Mater., **2000**; Vol. 217, p. 5–13

11) Pinkas J., Reichlova V., Serafimidisova A., Moravec Z., Zboril R., Jancik D. and Bezdicka P., *Sonochemical synthesis of amorphous yttrium iron oxides embedded in acetate matrix and their controlled thermal crystallization toward garnet ($Y_3Fe_5O_{12}$) and perovskite ($YFeO_3$) nanostructures*, J. Phys. Chem. C, **2010**; Vol. 114, p. 13557–13564.

12) Krishnan R., Lisfi A., Guyot M., Cagan V., *Preparation and some properties of pulsed laser deposited $YFeO_3$ films*, J. Magn. Magn. Mater., **1995**; Vol. 147, p. L221–224

13) Melnikov P., Nascimento V. A., Consolo L. Z. Z., Silva A. F., *Mechanism of thermal decomposition of yttrium nitrate hexahydrate, $Y(NO_3)_3.6H_2O$ and modeling of intermediate oxynitrates*, J. Therm. Anal. Calorim., **2013**; Vol. 111, p. 115-119

14) Wieczorek-Ciurowa K., Kozak A. J., *The Thermal decomposition of $Fe(NO_3)_3.9H_2O$*, J. Therm. Anal. Calorim., **1999**; Vol. 58, p. 647-651

15) Shimada M., Kume S., Koizumi M*., Possible Existence of Dense Ferrimagnetic Perovskite Allotropic Form of Yttrium Iron Garnet*, J. Am. Ceram. Soc., **1968**; Vol. 51, p. 713.

16) de Rouffignac P., Park J.-S., Gordon R.G., *Atomic layer deposition of Y_2O_3 thin films from yttrium tris(N,N'-diisopropylacetamidinate) and water*, Chem. Mater., **2005**; Vol. 17, p.4808–4814.

17) Cheary R.W., Coelho A., *A fundamental parameters approach to X-ray line-profile fitting*, J. Appl. Crystallogr., **1992**; Vol. 25, p. 109–121.

18) Lü X., Xie J., Shu H., Liu J., Yin C., Lin J., *Microwave-assisted synthesis of nanocrystalline $YFeO_3$ and study of its photoactivity*, Mater. Sci. Eng., B, **2007**; Vol. 138, p. 289-292

19) Wu L., Yu J.C., Zhang L., Wang X., Li S., *Selective self-propagating combustion synthesis hexagonal and orthorhombic nanocrystalline yttrium iron oxide*, J. Solid State Chem., **2004**; Vol. 177, p. 3666-3674

20) Kubelka P.and Munk F., *Ein Beitrag zur Optikder Farbanstriche*., Z. tech. Phys., **1931**; Vol. 12, p. 593-601.

Chapter 2: Yttrium Orthoferrite powder: Influence of organic additives

Different groups mention the role of citric acid as a chelating agent to stabilize metal cations via the carboxylic acid group[1,2]. This synthesis path is also known as "Pechini method"[3]. Others use urea as a homogeneous precipitator[4]. In this work, various compounds (oxalic acid, malonic acid, tartaric acid, citric acid or urea (fig. 2.1)) were tested in order to obtain the purest $YFeO_3$. Moreover, we noticed that the crystallization temperature is considerably lowered when organic acids are used. A process, known as the Merck process, generates in situ heat when nitrates and organics are mixed[5].

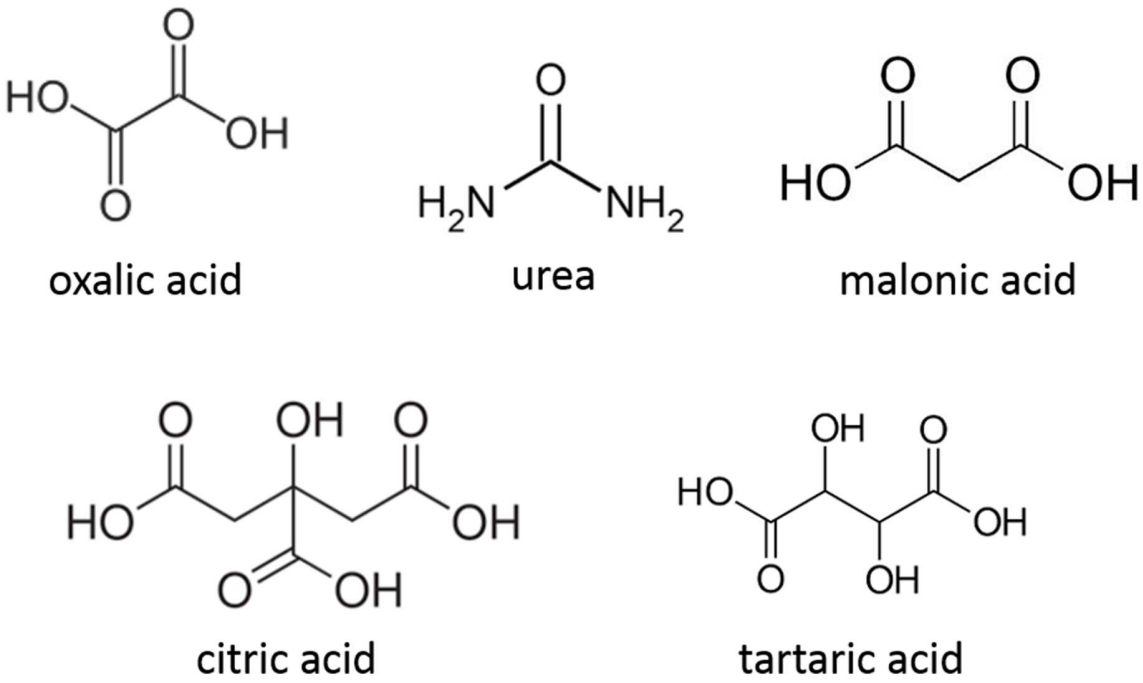

Figure 2.1: Representation of additives' chemical structure

These molecules contain carbon and can play the role of fuel in the self-ignition process. Higher local temperatures induce the crystallization of our compound.

The Pechini method is based on complexation and polymerization. These additives, if they contain carboxylic groups, may interact with cations. According to this way of thinking, urea will probably not really influence the reaction.

As a complexing agent, some of these molecules may help to bring the yttrium and iron cations closer to each other. This may favor the formation of a crystalline structure. The more flexible the molecule is, the closer the cations are. If the cations are close to each other, crystallization into their oxide structures requires a reduced amount of energy, a lower thermal treatment. The oxalic and malonic acids are less flexible, and thus have lesser possibilities than tartaric or citric acid to gather yttrium and iron with their carboxylic extremities. We expect a better result for these last two acids.

2.1 Synthesis protocol based on nitrate cations and additives

Solutions of 20 ml of $Fe(NO_3)_3$ 0.1 M and 20 ml of $Y(NO_3)_3$ 0.1 M were prepared by dissolving $Fe(NO_3)_3.9H_2O$ and $Y(NO_3)_3.6H_2O$ in de-ionized water, respectively. These two solutions were then mixed. We added a solid organic compound (oxalic acid, malonic acid, tartaric acid, citric acid or urea) at a concentration of 0.1 M and the final solution was stirred overnight. We added NH_4OH to reach a pH of 7. The mixture was heated at 60°C overnight to obtain a gel. The color of the obtained gel depends on the additive. This gel, still containing organic compounds, was heated at 150°C for 1 h on a sand bath because self-ignition occurs in some cases. Then, all the gel samples were heated to 450°C, 650°C or 850°C. Every temperature was reached with a heating ramp of 300°C/h and was kept for 2 h. The resulting fluffy brown solid was then ground prior to characterization. The samples were named N, N+oxalic, N+malonic, N+tartaric, N+citric and N+urea.

2.2 Characterizations

We will compare the results obtained by the techniques used in the first chapter to the samples prepared with additives. The influence of these additives will be discussed here.

2.2.1 pH monitoring

The urea pH curve fits most closely to the curve related to the solution without any additive (fig. 2.2). The inflections in this curve are more pronounced.

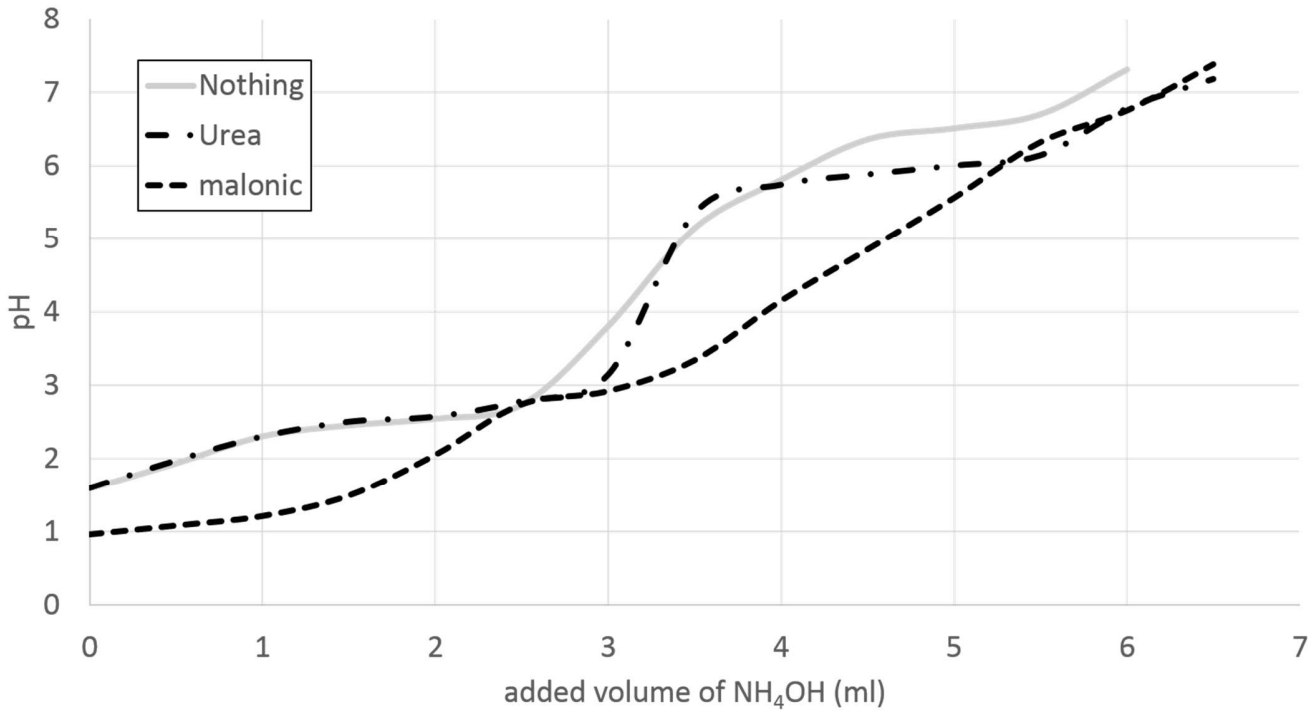

Figure 2.2: pH evolution, depending on an added volume of NH_4OH 2,5M, of 50 ml solutions based on a nitrate precursor ($[Y^{3+}]=[Fe^{3+}]=0,1M$) compared to similar solutions containing urea or malonic acid

Two milliliters more of NH_4OH are necessary to begin the precipitation of yttrium following the beginning of the precipitation of iron, when the sample contains urea. Without urea, only 1 ml is required (see previous chapter: fig. 1.2). A larger quantity of iron precipitates before the yttrium starts to precipitate and the inhomogeneity in the gel is increased.

Malonic acid (fig. 2.2), like all the other acids (fig. 2.3), reduces the pH of the solution before the addition of ammonium hydroxyde. Addition of acid in solution increases the concentration of H_3O^+ in this solution and the pH value decreases.

The malonic and oxalic acids show more or less the same curve structures: an initial horizontal portion attributed to the progressive neutralization of their first acidic function. Then, they reach and stabilize at a value close to the pKa of $Fe^{3+}/Fe(OH)^{2+}$. But this second step seems to be delayed, approximatively 1,5 ml later for malonic acid and 2 ml later in the case of oxalic acid. Furthermore, this step is also smaller with malonic acid, reducing from 1,5 ml in the solution without any additive to 0,75 ml for the considered additive. After this step, these two curves, for the oxalic and malonic additives, rise quite regularly. Inflexions are not

as visible as in the sample without any additive, making us think that both the hydroxylation of iron and yttrium happen at the same speed, leading to a possibly more homogeneous mixture.

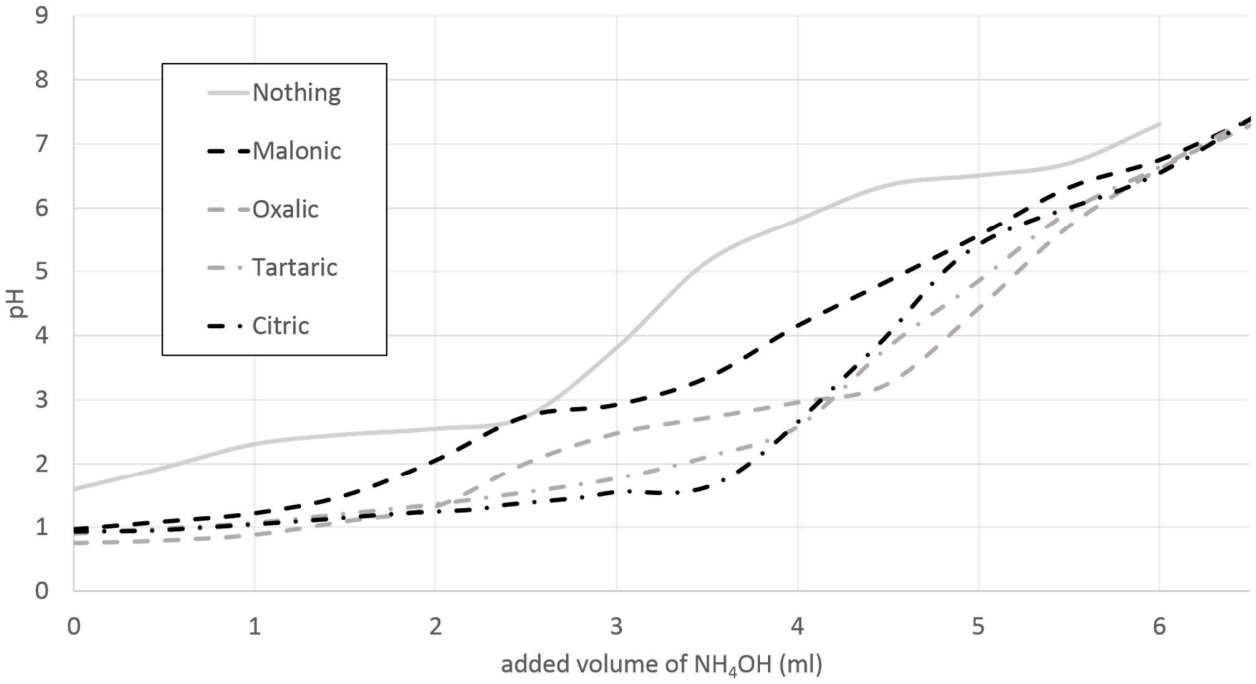

Figure 2.3: pH evolution, depending on an added volume of NH_4OH 2,5M, of 50 ml solutions based on a nitrate precursor ($[Y^{3+}]=[Fe^{3+}]=0,1M$) compare to similar solutions containing various organic acid

The tartaric and citric acids curves don't show any plateau at the pKa value of $Fe^{3+}/Fe(OH)^{2+}$. We may think that these compounds produce complex cations. Fe^{3+} is not available anymore to form $Fe(OH)^{2+}$. Indeed the pH remains quite stable until 2 (for tartaric acid) or 3 milliliters (for citric acid) before rising regularly to a pH of 7.

2.2.2 Crystallinity and phase composition

In addition to the previously mentioned compounds (hexagonal $YFeO_3$, cubic Y_2O_3 or hematite), we also checked for the possible presence of oxycarbonates ($Y_2O_2CO_3$ (PDF: 00.058-0472)) but these compounds were not detected in our samples.

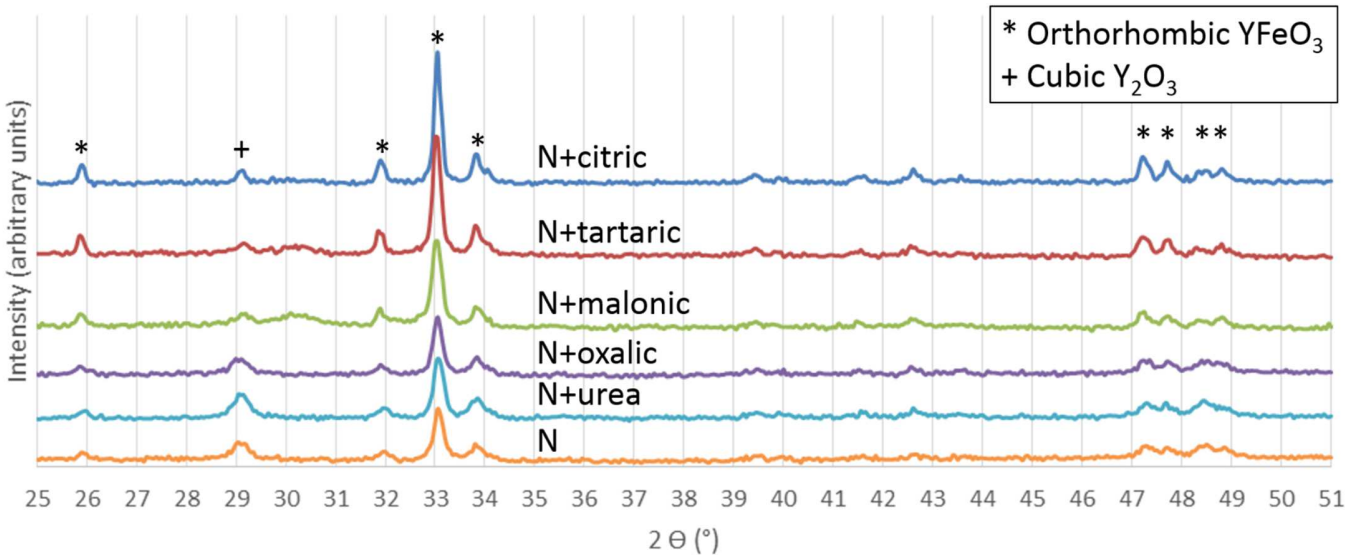

Figure 2.4 : XRD patterns of powders based on a nitrate precursor with and without additives (citric acid, tartaric acid, malonic acid, oxalic acid or urea) treated at 850°C for 2h

The average crystallite size, based on Sherrer's equation (eq. 1.6), for each sample is reported in tab. 2.1.

Table 2.1: The average crystallite size in N(+additives) of samples calcined at 850°C

Sample	Average crystallite size (nm)
N+urea 850°C	39 (~large crystallites)
N+malonic 850°C	39 (~large crystallites)
N 850°C	43 (large crystallites)
N+oxalic 850°C	43 (large crystallites)
N+tartaric 850°C	48 (large crystallites)
N+citric 850°C	56 (large crystallites)

At 850°C, all the samples are very well crystallized. The sample prepared with citric acid presents the best-resolved peaks of its X-ray diffraction (fig. 2.4). The high intensity and narrow FWHM of the diffraction peaks suggest that this sample contains less amorphous phase, if any, than all the other samples. However, the amorphous content was not experimentally verified by mixing the powder with an internal standard.

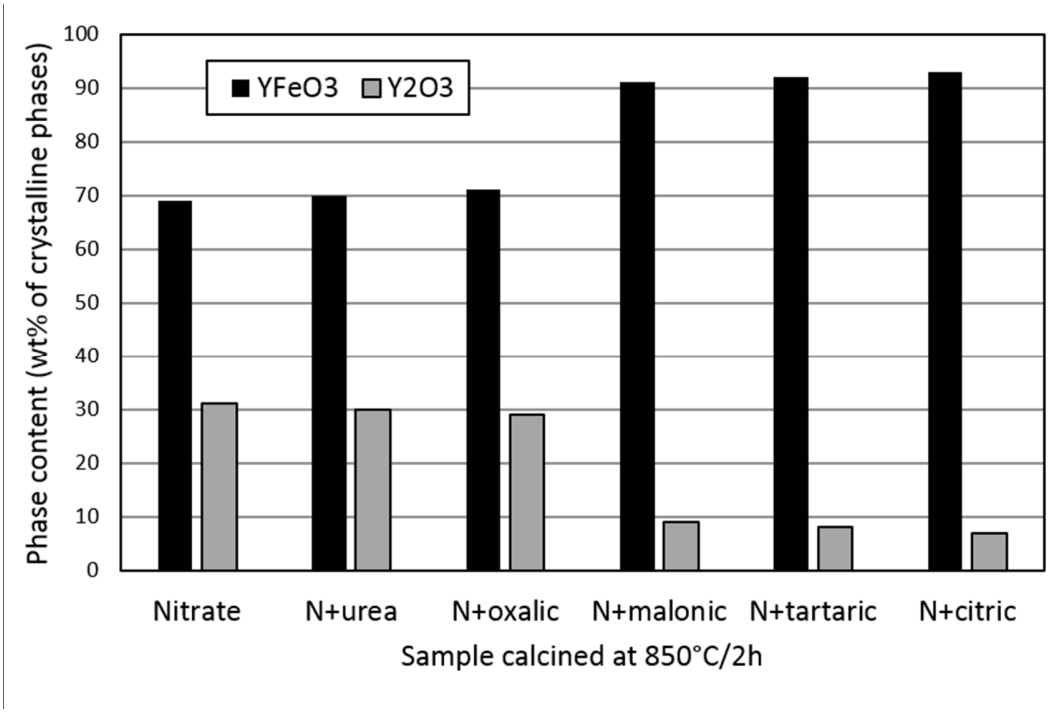

Figure 2.5: The influence of precursor on the phase content ($YFeO_3$ and Y_2O_3) for N(+additives) with samples calcinated at 850°C for 2h

The proportion of desired crystallized compound (o-$YFeO_3$) is clearly best with citric, tartaric or malonic acid when samples are treated at 850°C.

2.2.3 Crystallinity and phase composition at various temperatures

Yttrium Orthoferrite crystallizes at a lower temperature when organic acid are added (fig. 2.6).

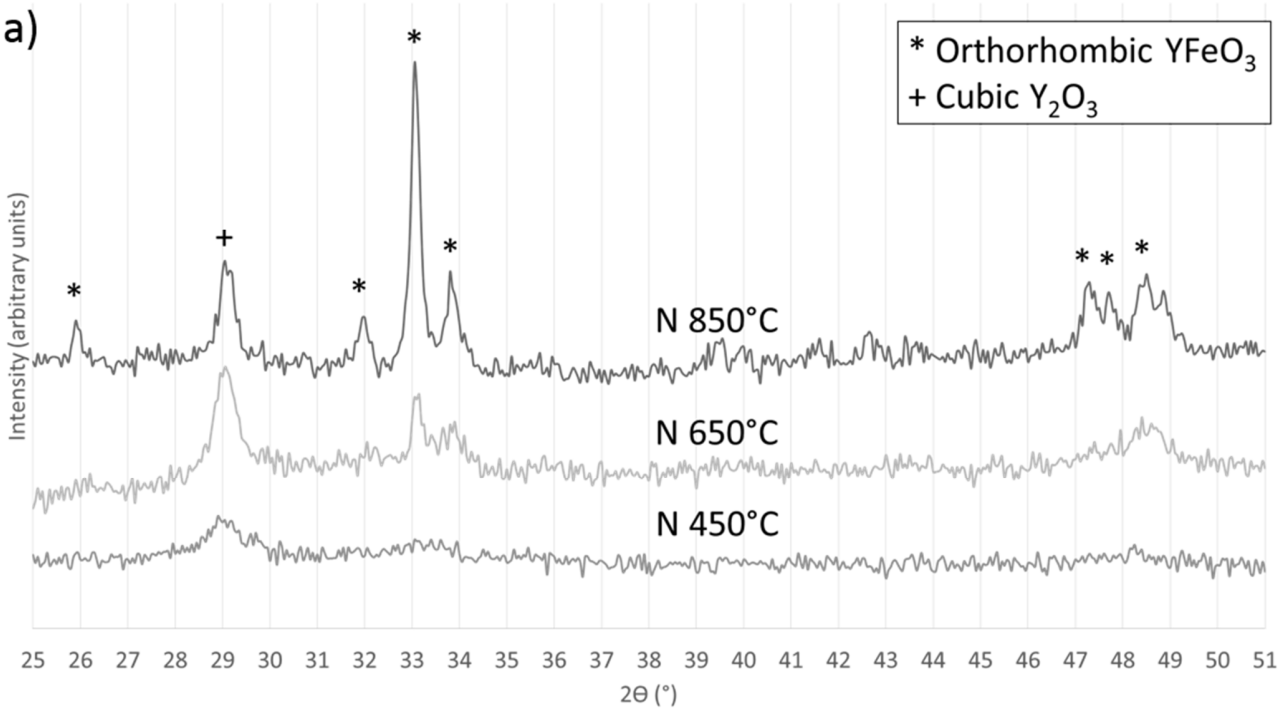
a)
* Orthorhombic YFeO3
+ Cubic Y2O3
Intensity (arbitrary units)
N 850°C
N 650°C
N 450°C
25 26 27 28 29 30 31 32 33 34 35 36 37 38 39 40 41 42 43 44 45 46 47 48 49 50 51
2Θ (°)

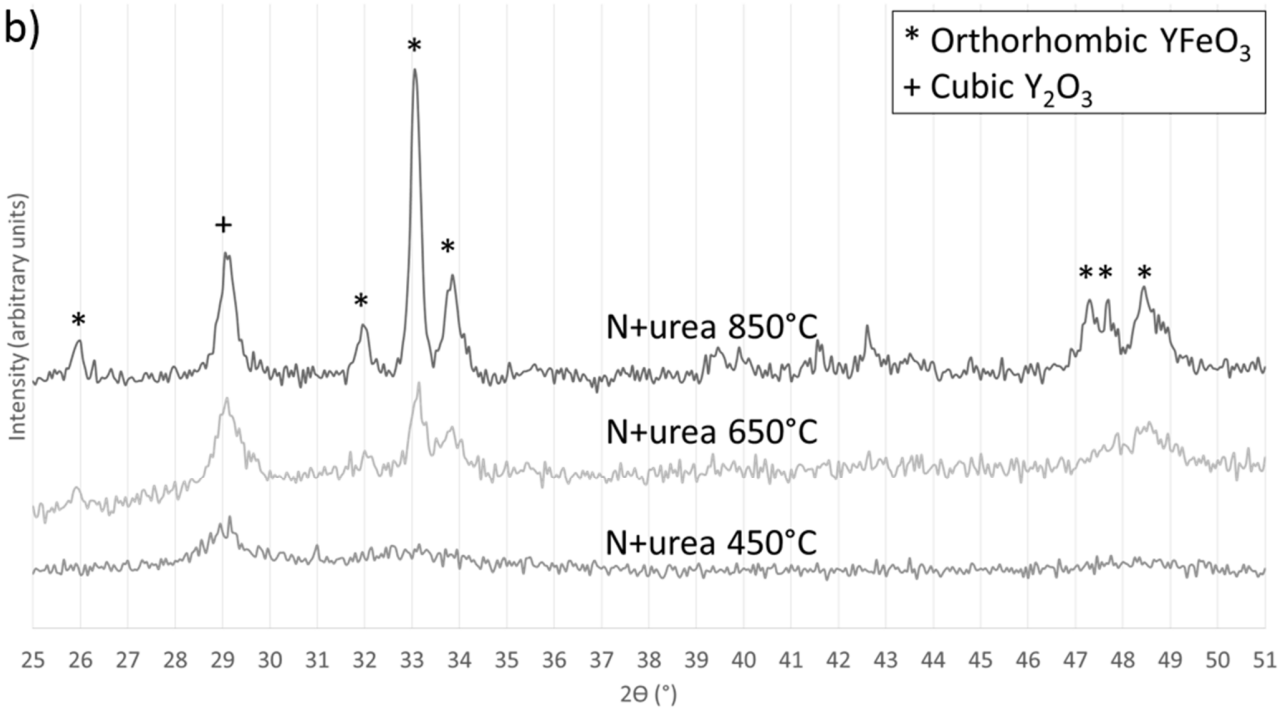
b)
* Orthorhombic YFeO3
+ Cubic Y2O3
Intensity (arbitrary units)
N+urea 850°C
N+urea 650°C
N+urea 450°C
25 26 27 28 29 30 31 32 33 34 35 36 37 38 39 40 41 42 43 44 45 46 47 48 49 50 51
2Θ (°)

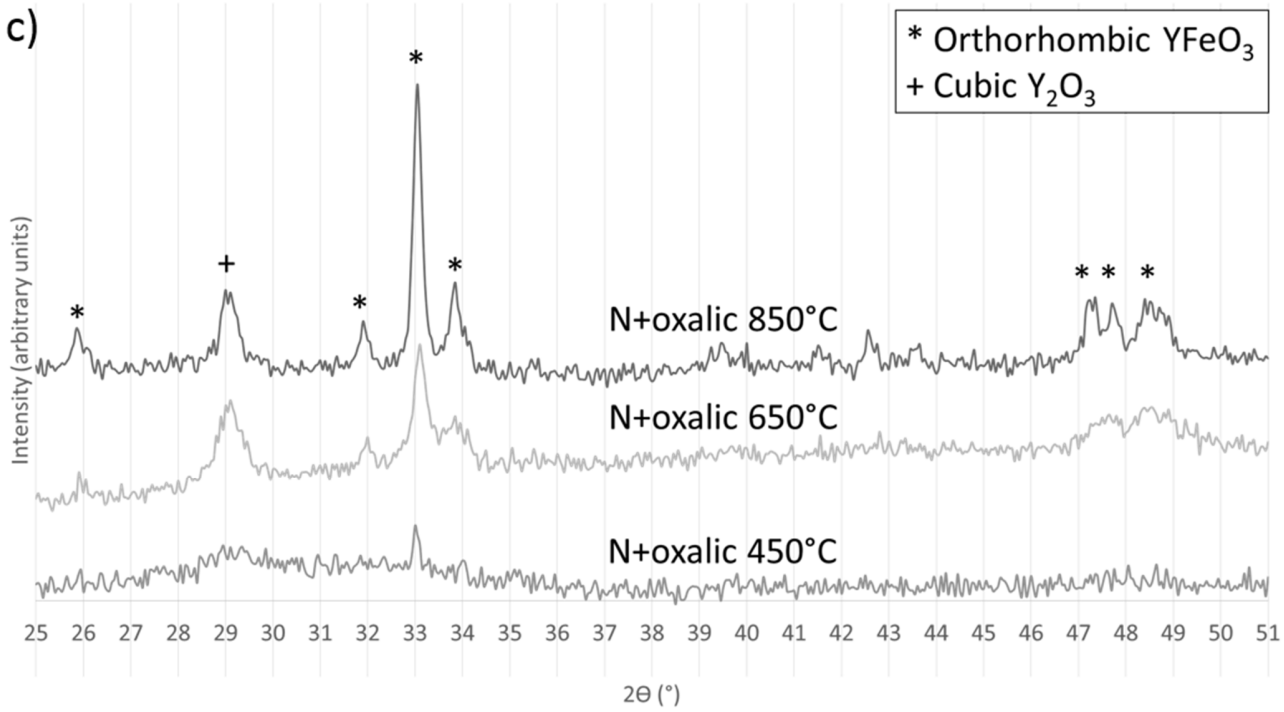
c)
* Orthorhombic YFeO3
+ Cubic Y2O3
Intensity (arbitrary units)
N+oxalic 850°C
N+oxalic 650°C
N+oxalic 450°C
25 26 27 28 29 30 31 32 33 34 35 36 37 38 39 40 41 42 43 44 45 46 47 48 49 50 51
2Θ (°)

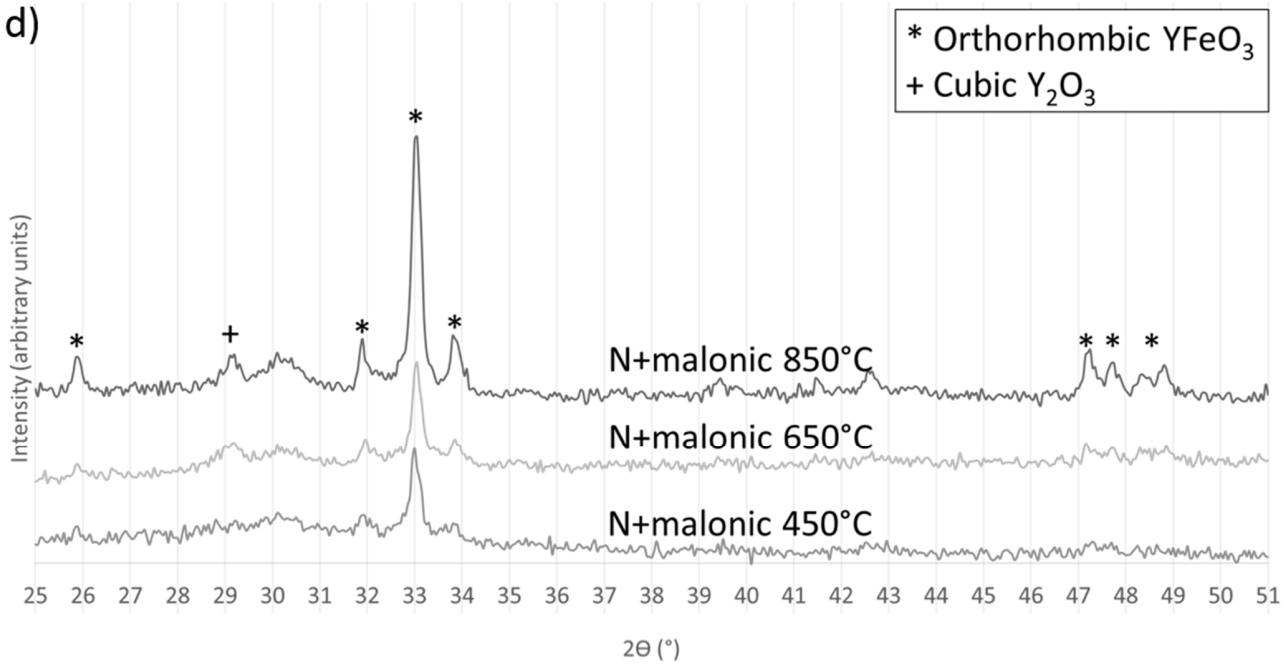
d)
* Orthorhombic YFeO3
+ Cubic Y2O3
Intensity (arbitrary units)
N+malonic 850°C
N+malonic 650°C
N+malonic 450°C
25 26 27 28 29 30 31 32 33 34 35 36 37 38 39 40 41 42 43 44 45 46 47 48 49 50 51
2Θ (°)

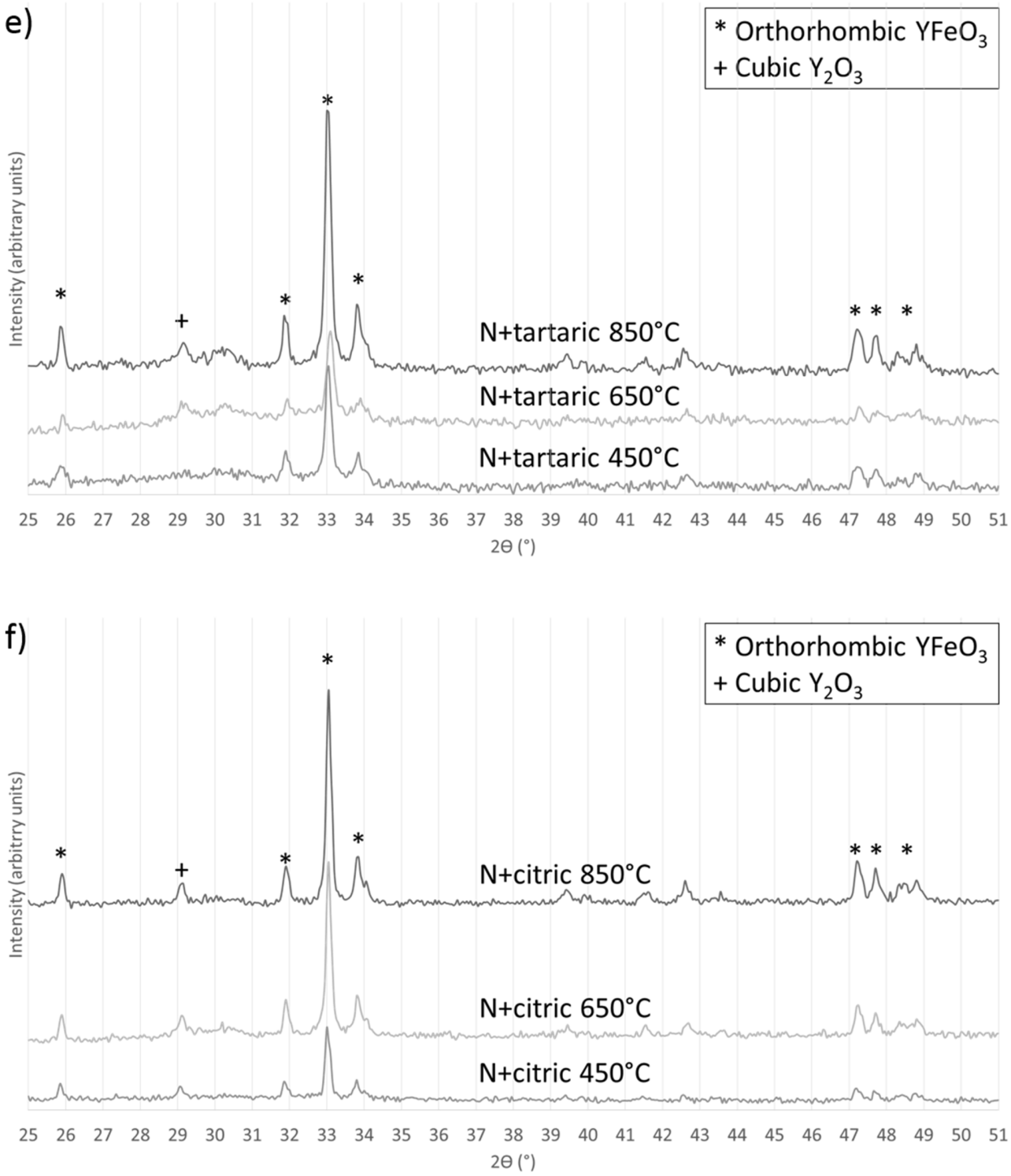

Figure 2.6: XRD patterns of samples based on (a) a nitrate precursor, on a nitrate precursor with (b) urea, (c) oxalic acid, (d) malonic acid, (e) tartaric acid or (f) citric acid treated at 850°C, 650°C or 450°C for 2h

Adding urea to the nitrate initial mixture does not affect the crystallization temperature, the X-ray diffractograms with urea (fig. 2.6 b) or without (fig. 2.6 a) are nearly superimposable. Organic acids (fig. 2.6 c to f) allow our compound to crystallize at lower temperatures (tab. 2.2). Indeed, self-ignition occurs at temperatures between 100°C and 200°C, depending on which acid was added and/or distribution of the dried gel in the crucible, inducing or not a confinement of gases that burn when the concentration and temperature allow them to do so. The temperature locally increases and generates crystallization. After self-ignition, the crystals just grow.

Table 2.2: The average crystallite size in samples based on nitrates additives with and without additives at various temperatures. Crystallites above a 40nm size are considered as large crystallites (l.c.).

Sample	Average crystallite size (nm) at 850°C	Average crystallite size (nm) at 650°C	Average crystallite size (nm) at 450°C
Nitrates	$YFeO_3$: 43 (l.c.) Y_2O_3: 27	$YFeO_3$: 45 (l.c.) Y_2O_3: 18	$YFeO_3$: amorphous Y_2O_3: 11
N + urea	$YFeO_3$: 39 (~l.c.) Y_2O_3: 24	$YFeO_3$: 42 (l.c.) Y_2O_3: 17	$YFeO_3$: amorphous Y_2O_3: 17
N + oxalic acid	$YFeO_3$: 43 (l.c.) Y_2O_3: 23	$YFeO_3$: 35 Y_2O_3: 15	$YFeO_3$: 60 (l.c.) Y_2O_3: amorphous
N + malonic acid	$YFeO_3$: 38 (~l.c.) Y_2O_3: 39 (~l.c.)	$YFeO_3$: 42 (l.c.) Y_2O_3: 19	$YFeO_3$: 39 (~l.c.) Y_2O_3: amorphous
N + tartaric acid	$YFeO_3$: 48 (l.c.) Y_2O_3: 37	$YFeO_3$: 44 (l.c.) Y_2O_3: 36	$YFeO_3$: 39 (~l.c.) Y_2O_3: amorphous
N + citric acid	$YFeO_3$: 57 (l.c.) Y_2O_3: 49 (l.c.)	$YFeO_3$: 56 (l.c.) Y_2O_3: 50 (l.c.)	$YFeO_3$: 56 (l.c.) Y_2O_3: 48 (l.c.)

Samples containing an organic acid have crystallized yttrium orthoferrite even at a low temperature (450°C). Self-ignition occurs every time organic acids are present in our samples. This is not the case in the samples containing just nitrates or nitrates mixed with urea. Self-ignition induces the formation of the first crystallites that continue to grow during the thermal increase.

Y_2O_3 needs a fairly low temperature to crystallize[6]. But its quantity (fig. 2.5) decreases when organic acids are added. The high localized increase in temperature and the molar ratio of Y:Fe are more favorable to the orthorhombic $YFeO_3$ crystallization.

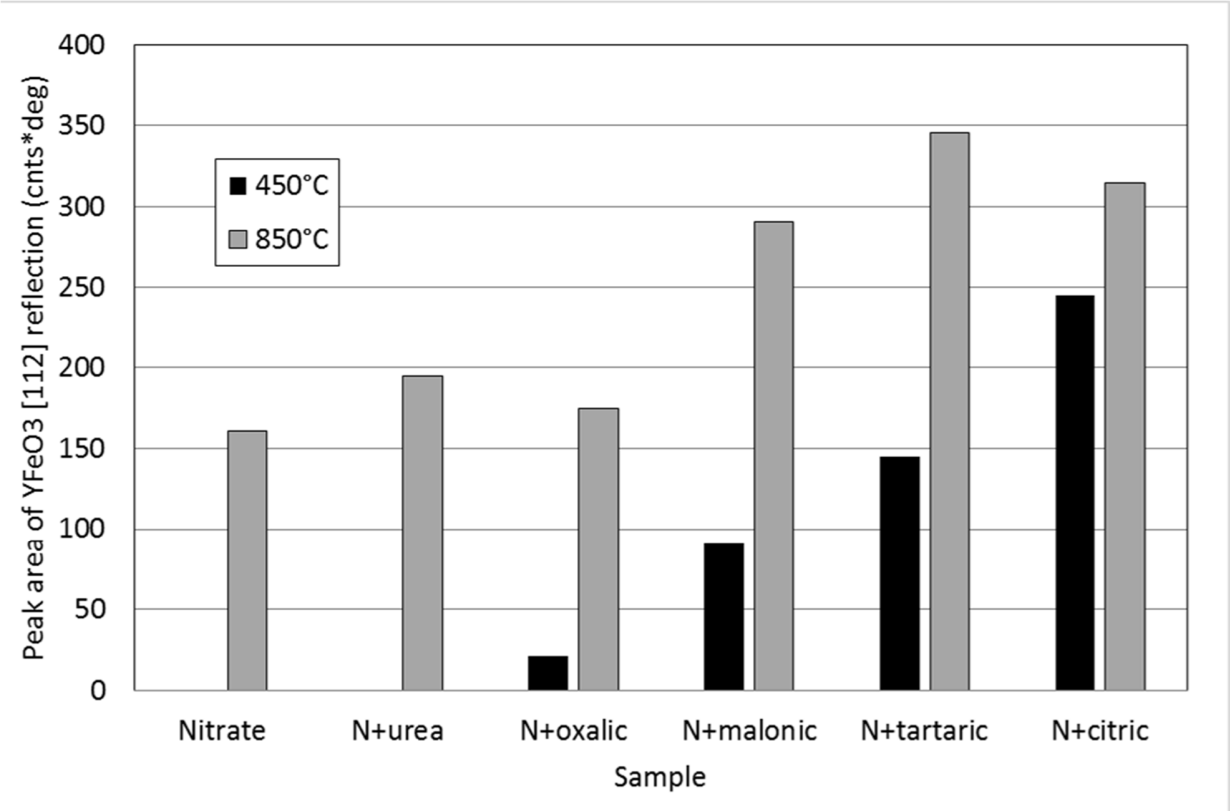

Figure 2.7: The quantity of crystallized o-$YFeO_3$ estimated by the peak area under the [112] reflection on X-ray diffractograms at various temperatures

Most of the organic acids added, increase the proportion of crystallized orthorhombic yttrium orthoferrite. Once again, this is due to self-ignition reaction. The best crystallized sample at 450°C was the one prepared with citric acid. Citric acid has 3 carboxylic groups allowing better complexation of cations. Due to this complexation capacity, yttrium and iron cations are closer together than if they are not complexed. The closer they are, the less energy is required to crystallize them into oxides. Complexing agents work better if they are flexible and if their carboxylic group can interact easily with cations.

2.2.4 Determination of optical band gap

The Tauc plot (fig. 2.8) derived from DRS and the Kubelka–Munk function for indirect band gap of the sample prepared from the nitrate precursors mixed with citric acid heated at 450°C for 2hrs, gives an optical band gap value of 2,2eV.

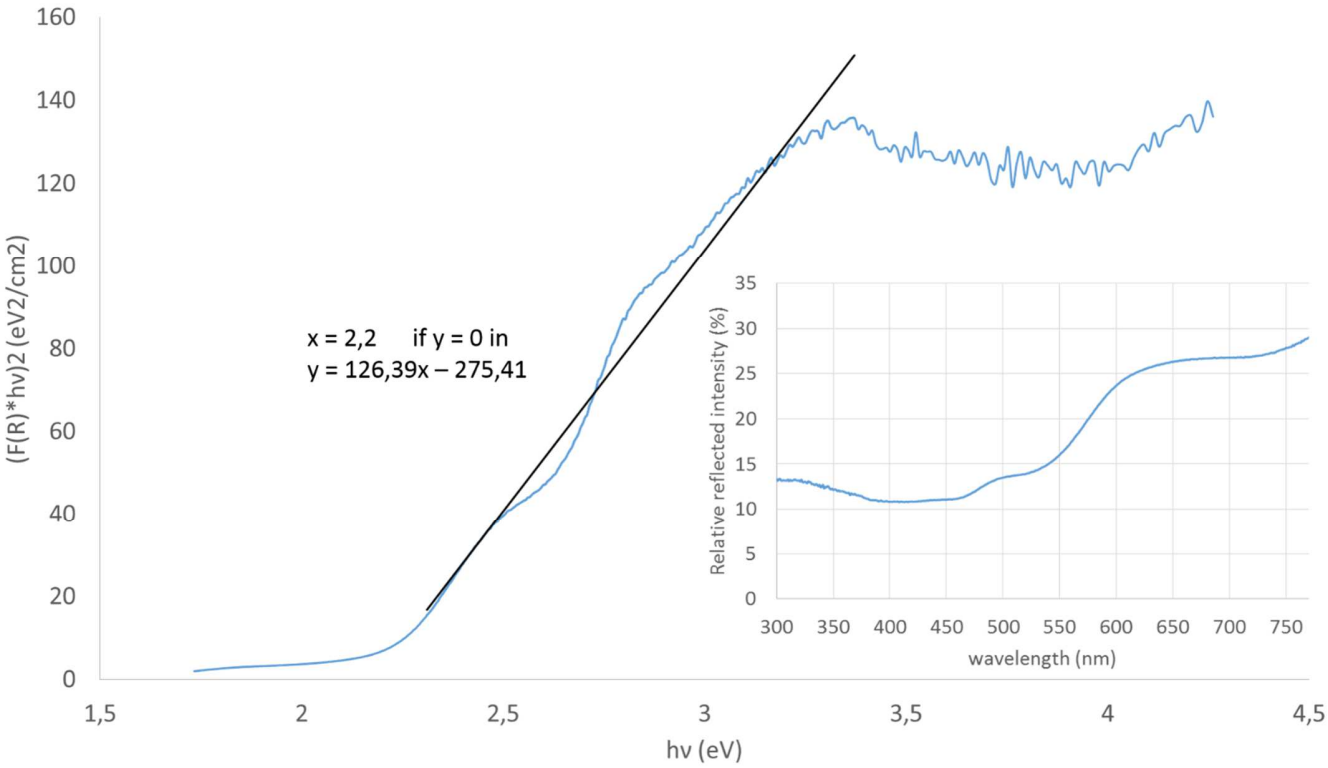

Figure 2.8: The determination of optical band gap value of x when y = 0 in the linear regression, via a Tauc plot obtained from diffuse reflectance spectroscopy (see insert) for a sample prepared from the nitrate precursors mixed with citric acid heated at 450°C for 2hrs.

The optical band gap has the same value (2,2 eV) for samples without citric acid and heated at higher temperature (850°C). The presence of carbonated compound in the precursor's solution leaves no trace in the final heated compound.

2.3 Conclusion

The addition of an organic compound influences the crystallization. This study reveals that citric acid improves the phase content in o-$YFeO_3$ and decreases its crystallization temperature by 400°C, starting from 850°C. Such a reduction could be interesting for coating applications, especially as glass melts at 850°C. The ability to crystallize o-$YFeO_3$ at lower temperatures opens the possibility to use glass as a potential substrate.

2.4 Bibliography

1) Kudo A., Miseki Y., *Heterogeneous photocatalyst materials for water splitting*, Chem. Soc. Rev., **2009**, Vol. 38, p.253–278

2) Zhang Y., Yang J., Xu J., Gao Q., Hong Z., *Controllable synthesis of hexagonal and orthorhombic $YFeO_3$ and their visible-light photocatalytic activities*, Mat. Lett. **2012**, Vol. 81, p. 1-4

3) Pechini M. P., US Patent 3,3306,97. **1967**

4) Lü X., Xie J., Shu H., Liu J., Yin C., Lin J., *Microwave-assisted synthesis of nanocrystalline $YFeO_3$ and study of its photoactivity*, Mater. Sci. Eng., B, **2007**, Vol. 138, p.289-292

5) Messing G.L., Zhang S.-C., Jayanthi G.V., *Ceramic Powder Synthesis by Spray Pyrolysis*, J. Am. Ceram. Soc., **1993**, Vol. 76, Iss. 11, p. 2707-2726

6) de Rouffignac P., Park J.-S., Gordon R.G., *Atomic layer deposition of Y_2O_3 thin films from yttrium tris(N,N'-diisopropylacetamidinate) and water*. Chem. Mater., **2005**, Vol. 17, p.4808–4814

Chapter 3: Dip coated films

We succeeded to synthetize crystallized o-$YFeO_3$ in powder form. Our target is to have this compound coated on a substrate. Lots of coating techniques are reported in the literature: spin and dip coating[1-5], (ultrasonic) spray pyrolysis[3,6], infiltration of precursor's solution in 3D-ordered latex film[7], Plasma vapor deposition[2] and Pulsed laser deposition[8]. All these techniques can be divided into two groups based on the nature of the coating process: physical or chemical deposition. Out of all these techniques, we use the sol-gel dip-coating technique that is a chemical deposition technique[10,11].

3.1 Dip coating process

Dip coating is a technique used to coat a substrate with a film of solution or a stable suspension of nanoparticles. The process consists in the immersion and withdrawal of a substrate in and out of a precursor's solution[12,13].

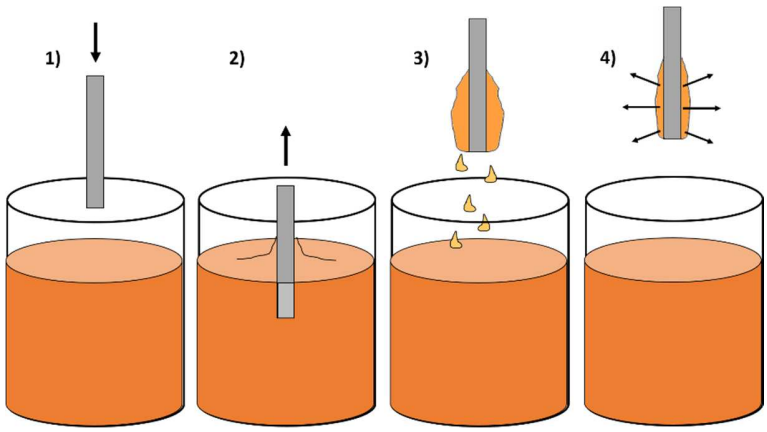

Figure 3.1: The four steps of dip coating process: 1) substrate immersion, 2) deposition and removal, 3) drain, 4) solvent evaporation.

It includes several steps (fig. 3.1): a substrate is immersed in a solution until a fixed depth is reached (1). Then, the substrate is pulled out of the solution with a well-defined withdrawal speed (2). The excess of liquid on the surface is drained during the withdrawal (3). A film of the solution remains on the dipped part of the substrate. The temperature and atmospheric conditions must be controlled, because they define the evaporation rate of the solvent and subsequent film's formation (4). At the end of these four steps, the samples are heated to remove all the remaining solvent and initiate the organization of the deposited particles (fig. 3.2) on the

substrate. This is called the densification step and the temperature of this treatment depends on the film's composition[12]. If the coating is required to be thicker, the whole process, called the dip cycle, is repeated from step one to five as many times as necessary.

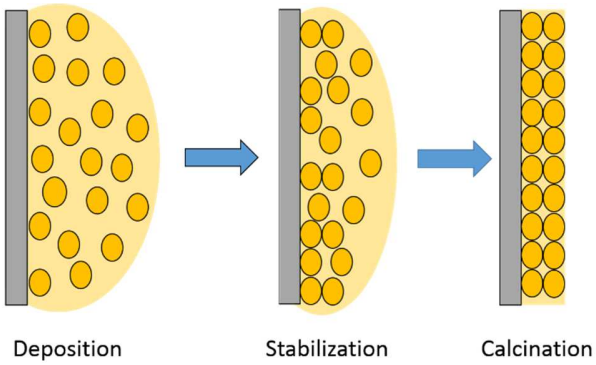

Figure 3.2: Particles repartition upon thermal treatment.

3.2 Tunable parameters

The properties of the coating (homogeneity, thickness and adherence) are influenced by different parameters. These parameters are related to the process, the substrate and the solution.

3.2.1 Process-related parameters

* **Gravity** is a parameter that cannot be changed. It is one of the six forces acting on the coating[12]. The five other are (1) the viscous drag upward on the liquid by moving the substrate, (2) the resultant force of surface tension in the concavely shaped meniscus (fig. 3.3), (3) the inertial force of the boundary layer liquid arriving at the deposition region, (4) the surface tension gradient and (5) the disjoining or conjoining pressure if the film is thinner than 1µm[12].

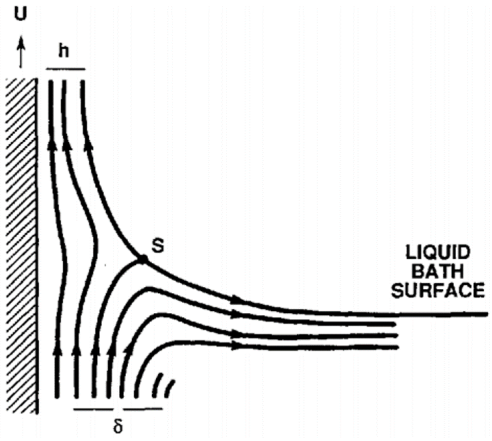

Figure 3.3: The liquid flow pattern during dip coating. U is the withdrawal speed, S is the stagnation point, δ is the boundary layer and h is the thickness of the fluid film.[13]

Due to gravity, the deposit may be reduced in the upper part of the substrate and increased in its lower part. Such deposits are inhomogeneous along the dipping axis (fig. 3.4).

To reduce the impact of gravity, we must decrease the time of solvent evaporation (cfr relative humidity).

Figure 3.4: A sample where the inhomogeneous coating (more material is deposited at the bottom of the substrate) is mainly due to gravity.

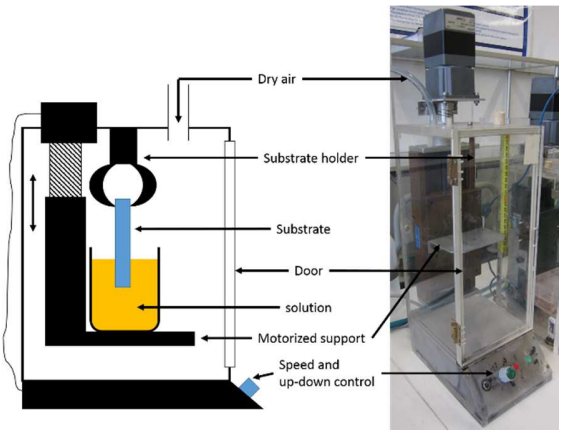

Figure 3.5: Elements of the dip coating room.

* **Speed of removal** influences the thickness of the deposit. The Landau-Levich equation (eq. 3.1)[15] describes the relation between the substrate withdrawal speed (U) and the deposited film thickness (h). This equation is obtained when the viscous drag (a function of the fluid viscosity and the speed of removal) balances the gravitational force[12,13,14].

$$h = c_1.(\frac{\eta.U}{\rho.g})^{1/2} \qquad \textit{Equation 3.1}$$

where h is the deposited film thickness, c_1 is a constant (about 0,8 for Newtonian liquids), η is the fluid viscosity, U is the substrate withdrawal speed, ρ is the fluid density and g is the acceleration due to gravity at the Earth's surface. This equation is modified in this dip coating case (eq. 3.2) because the withdrawal speed and fluid viscosity are both low in this process and additionally another parameter has to be taken into account: the liquid-vapor surface tension (γ_{LV})[12,13].

$$h = 0{,}94.\frac{(\eta.U)^{2/3}}{\gamma_{LV}^{\frac{1}{6}}.(\rho.g)^{1/2}} \qquad \textit{Equation 3.2}$$

Despite this correction, the experimental results deviate from this model. These deviations have been attributed to a variety of reasons including effects of inertia, substrate charge and pre-treatment procedures (i.e., cleaning), and surfactants[16].

* **Relative humidity (RH)** in the dip coating room (fig. 3.5) influences the solvent evaporation. If the RH is low (5 to 10% for example), solvent leaves the coated solution relatively fast without leaving time for the particles to organize themselves or time for the solution to be affected by gravity. A too high RH induces a slow solvent evaporation. It increases the time the process takes and increases the influence of gravity.

The relative humidity is reduced by flushing dry air in the dip coating room. Our experiments do not focus on the organization of particles, but on the film homogeneity. We thus need a low RH. Water evaporation at room humidity is very slow, so we decided to work with a relative humidity of 10%. This corresponds to an evaporation time of 5 seconds. The complete evaporation of the solvent is visually observed on a silicon substrate. Indeed, when the solvent evaporates, the thickness of the coating varies inducing changes in its perceived color. This color change is caused by variations in the reflectance of the thin dielectric film with the wavelength of light[17].

* The **stabilization step** takes place out of the dip coating room, on a heating device. This promotes solvent evaporation (fig. 3.2), adherence to the substrate and may induce other chemical reactions. As mentioned in the previous chapter, self-ignition occurs at temperature around 150°C. This phenomenon is observed during the stabilization step.

* A **final calcination** step in an oven is applied after all the dip cycles. This step continues the chemical reaction and increases the crystallinity of the material.

3.2.2 Substrate-related parameters

* The **substrate surface** can have hydrophobic or hydrophilic properties. It affects the affinity between the solution and the substrate and thus the wettability of the deposited film. The substrate must be chosen according to the targeted applications in terms of the following properties: conductivity, transparency and price.

* **Roughness** influences the adherence of the solution on the substrate. It also influences the crystal growth during heat treatment. Fluorine-doped tin oxide (FTO) coated glass is one of the substrates used during this study. FTO coated on glass makes the substrate conductive. A thicker coating increases the conductivity of the substrate. Crystal domains in FTO are bigger for a thicker coating but also increase the roughness, thus affecting the adherence of the solution on such FTO-coated glass.

* The **washing process** is important in order to obtain a clean surface able to give a homogeneous coating with optimal adherence. We use two kinds of substrate: monocrystalline silicon and FTO-coated glass (FTOcG). The silicon substrate is stored in nitric acid 1 mol/L. The FTO-coated glass is stored in a box at room temperature. Before coating them with the solution, the samples were washed according to the same process: first, the surface is washed with de-ionized water, then with ethanol and finally with acetone before being blow-dried with air[9].

* **Thickness** of the substrate is a parameter determining the speed of the stabilization step. Indeed, the temperature of the hot plate, used during the heat treatment, is not equal to the temperature of the coated surface. The surface reaches this temperature after a while depending on its thickness and its thermal conductivity. Sometimes with a thick glass substrate,

due to a high thermal gradient, cracks appear in the substrate (fig. 3.6). Such substrate cannot be used for future applications.

Figure 3.6: A broken glass substrate due to the thermal gradient.

* **Edge effects** alter the homogeneity of the coating. To be negligible, the coated surface must be large enough.

3.2.3 Solution-related parameters

* The **solvent** can have hydrophobic or hydrophilic properties. The quantity of deposited film is influenced by the affinity between the solution and the substrate. This solvent must be removed from the coated solution. The evaporation speed depends on the boiling point of this solvent.

* A homogeneous coating depends on a **homogeneous solution**. If some precipitation occurs in the solution, the coating will not be uniform.

* Viscosity, density and the surface tension of the solution determine the thickness of the film[12]. All these values are included in a parameter called the **stagnation point** (fig. 3.3). Stagnation points are points where the local velocity is equal to zero and gravity is counterbalanced by all other forces. This parameter is a property of the solution. It could be tuned by changing the concentration or the pH within the solution.

3.3 Results and practical issues

In this approach, two substrates were tested, monocrystalline silicon (Si) and FTO-coated glass (FTOcG). The Si substrate was the firstly used because of its cheap price and mostly the fact that the color of the deposit gives an insight of the homogeneity and the thickness of the film[17].

3.3.1 Dip coating on Silicon substrate

In the previous chapter, we prepared orthorhombic yttrium orthoferrite from a solution containing 0,1M yttrium nitrate, 0,1M iron nitrate and 0,2M citric acid. To obtain powders, this precursor solution was stirred overnight and then mixed with ammonium hydroxide to reach a pH of 7, then further heated to promote self-combustion and produce solid particles. We used this precursor solution to prepare supported films by the dip-coating technique. **Dip coating conditions**: withdrawal speed = 1,5mm/s, 10% R.H., stabilization temperature of 150°C. The samples (fig. 3.7) are then put in a furnace and heated to 450°C with a heating ramp of 300°C per hour.

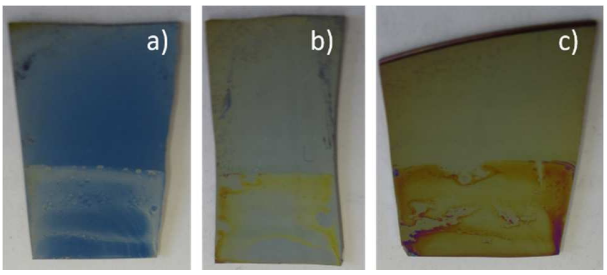

Figure 3.7: Si substrates coated a) 1 time, b) 2 times and c) 3 times with a solution of 0,1 M iron and yttrium, 0,2M citric acid with a pH adjusted to 7. These 3 samples have been heated at 450°C for 2h.

Figure 3.8: A Si substrate coated twice with a solution of 0,1 M iron and yttrium, 0,2M citric acid with a pH adjusted to 7 and then mixed with a spatula tipful of surfactant . The sample has been heated at 450°C for 2h.

As the quantity of solution that remains on the substrate after one cycle of coating is not enough, we increased the number of coating cycles.

Increasing the number of coated layers increases the thickness of the film. From a visual point of view, the color of the sample changes at every coating[17]. Fig. 3.7 shows that the film changes from blue to orange when increasing the number of layers from one to three, after calcination at 450°C. However, we can observe that the coating gets less homogeneous. Therefore, the dip-coating process has to be adapted to deposit more material per cycle.

* Changing the affinity between the solution and the substrate can affect the quantity of the remaining solution on the substrate. This affinity can be changed by adding a small quantity of **surfactant**[18]. We added a spatula tipful of Brij 58[1]. The resulting films contain more material but unfortunately remain inhomogeneous (fig. 3.8)

* Increasing the **concentration** of the solution induces an increase of the deposited quantity. New solutions with the same proportions as the initial solution (Y^{3+}:Fe^{3+}: citric acid = 1:1:2) are prepared with a concentration of metal nitrates of 0,25M. The resulting films are presented in fig. 3.9.

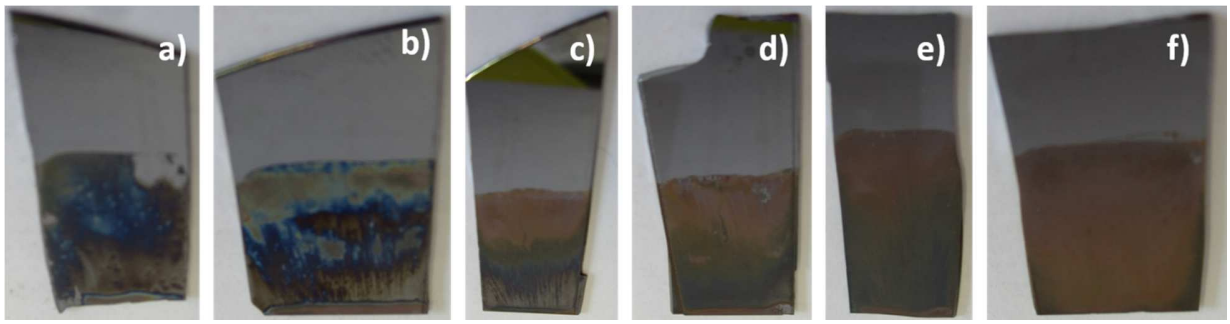

Figure 3.9: Si substrates coated with a) 1, b) 2, c) 3, d) 4, e) 5 and f) 6 times with a solution of 0,25 M iron and yttrium, 0,5M citric acid with a pH adjusted to 7. These 6 samples have been heated at 450°C for 2h.

Such a concentrated solution is unstable and after a while, precipitation of $YFeO_x(OH)_y$ occurs. We observe this phase separation during the dipping process. This precipitation induces a deposit of solid particles on the deposition front (see fig. 3.9 c and d). The quantity of coated material is not uniform. The coating may look uniform for the 6 times coated sample (fig. 3.9 f) but SEM imaging reveals that it exhibits a rough and not adherent surface (fig. 3.10). The color of

[1] Brij 58 = Polyethylene glycol hexadecyl ether

this sample is just due to the fact that for thick film, the treatment at 450°C gives an orange color to the layer.

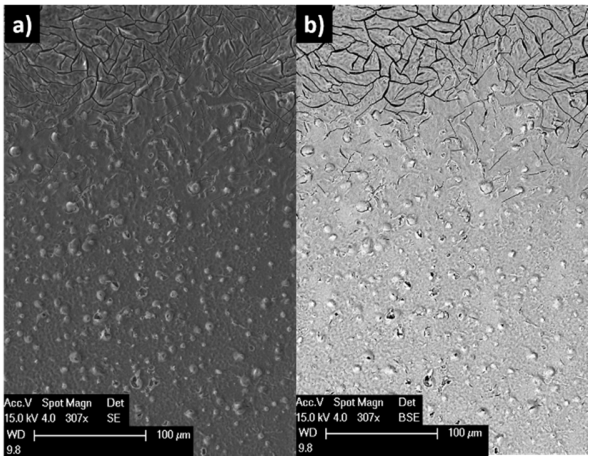

Figure 3.10: SEM images using a) secondary electrons (SE) and b) backscattered electrons (BSE) of a Si substrate coated 6 times with a solution of 0,25 M iron and yttrium, 0,5M citric acid with a pH adjusted to 7. The sample has been heated at 450°C for 2h (fig. 3.9 f).

The quantity of deposited material is more important on the deposition front. The heat treatment induces gas evacuation. When the coating is thin, gas bubbles leave craters behind (lower part of fig. 3.10). When the coating is thicker, layers of solution cover the substrate and cracks (upper part of fig. 3.10) appear during the heat treatment. These cracks result from gas evacuation and film contraction. The chemical composition of the film is homogenous, as confirmed by BSE (fig. 3.10 b). Again, the solution has to be adapted to overcome the appearance of a solid precipitate. This is discussed in the next section.

* **Peptisation** consists in adding a controlled quantity of acid to the solution to avoid the coagulation of the hydroxide species that are present in the precursor solution. Rajendran et al.[4] applied this strategy (fig. 3.11) by adding nitric acid to their precursor solution before dip-coating. They succeeded in obtaining a clear sol after the peptisation of a precipitate. The clear sol that we obtained has a pH of 0,9 and the concentration of this sol at 10^{-2} torr and at room temperature never allowed us to reproduce the redispersible, monolithic translucent gel described in their paper.

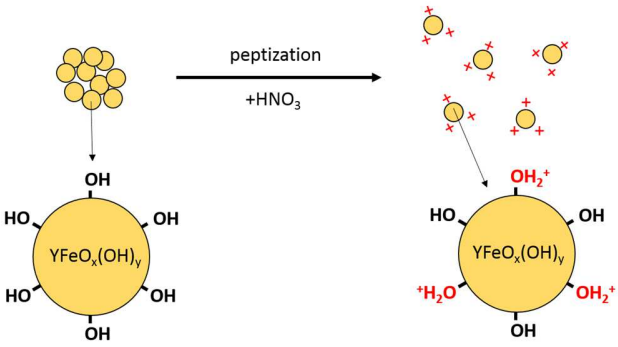

Figure 3.11: A scheme for precursor peptisation from aggregated particles to dispersed particles.

Figure 3.12: A Si substrate coated 2 times with a solution made of peptized precipitate. The sample is then heated at 450°C for 2h.

We peptize the brown gel obtained in the powder synthesis route (see section 1.1.2) with HNO_3 after filtering and washing it with water, until a clear sol is obtained. However, such a sol resulted in almost no deposition of $YFeO_3$ (fig. 3.12). We checked the pH of the sol which was revealed to be far too low (0,9) to preserve hydroxide species in solution. Therefore, a series of sols were prepared with pH varying from 1 to 6. These sols were then coated on a Si substrate (fig. 3.13).

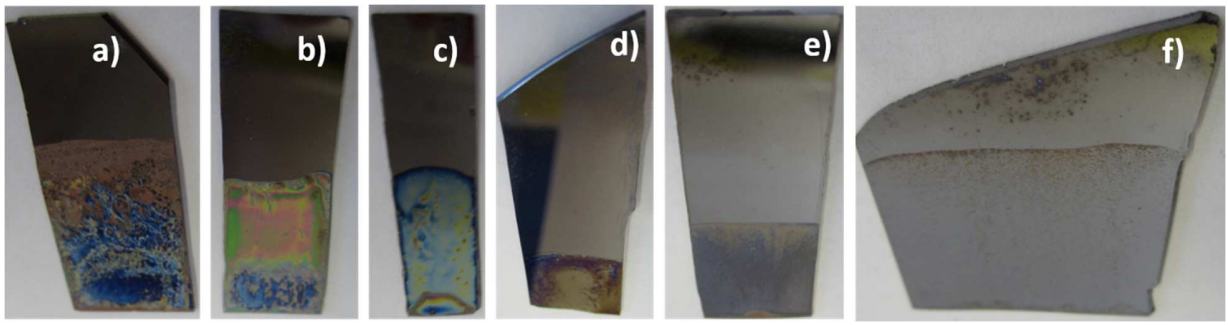

Figure 3.13: Si substrates coated twice with a solution of 0,25 M iron and yttrium, 0,5M citric acid with the pH adjusted to a) 6, b) 5, c) 4, d) 3, e) 2 or f) 1. These 6 samples have been heated at 450°C for 2h.

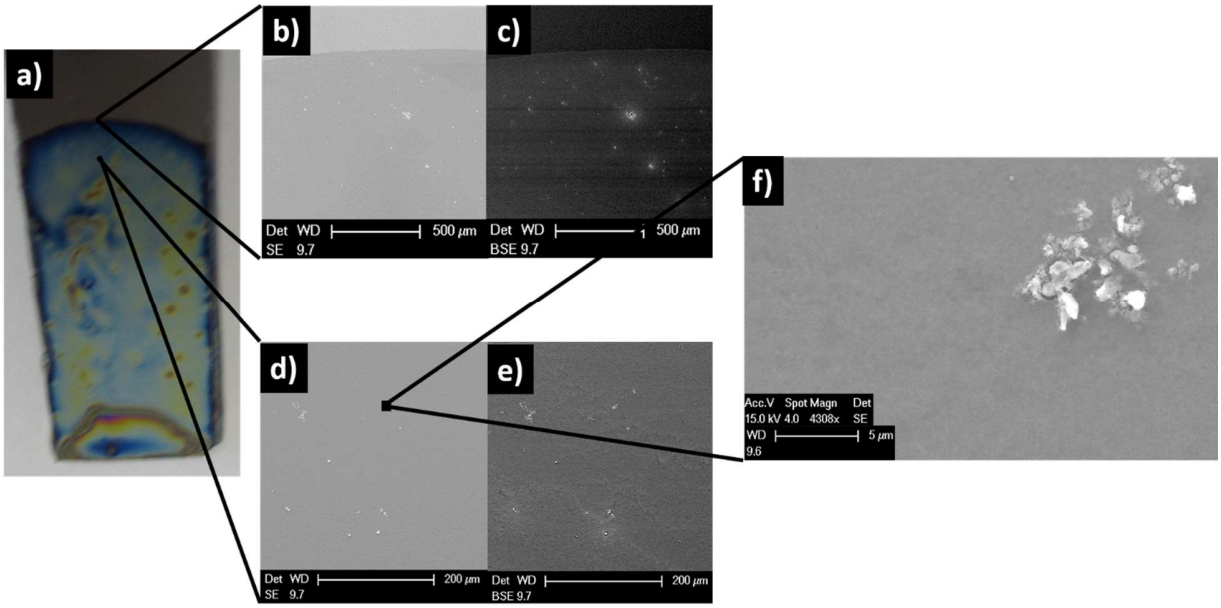

Figure 3.14: A visual picture a) and SEM images of SE b),d),f) and BSE c),e) of a Si substrate coated twice with a solution of 0,25 M iron and yttrium, 0,5M citric acid with a pH adjusted to 4. The sample has been heated at 450°C for 2h.

The sample prepared with a pH 4 (fig. 3.13 c) shows the most homogeneous coating. The topographic and chemical homogeneity is confirmed by SEM analysis (fig. 3.14). We selected this solution for coating the FTO substrates.

3.3.2 Dip coating on FTO

A solution made by mixing 1,91 g of yttrium nitrate hexahydrate, 2,02g of iron(III) nitrate nonahydrate and 1,92 g of citric acid in 20 ml of de-ionized water is mixed overnight. We added NH_4OH to reach a pH of 7, pH is then reduced to 4 by adding nitric acid (2M). This solution is then coated on FTO (fig. 3.15). This substrate has a different chemical composition and surface than Si and the coated solution has a different affinity with FTO. Here, this affinity is weak and results in a very thin deposit. To increase the quantity of deposited material, we perform multiple coating cycles.

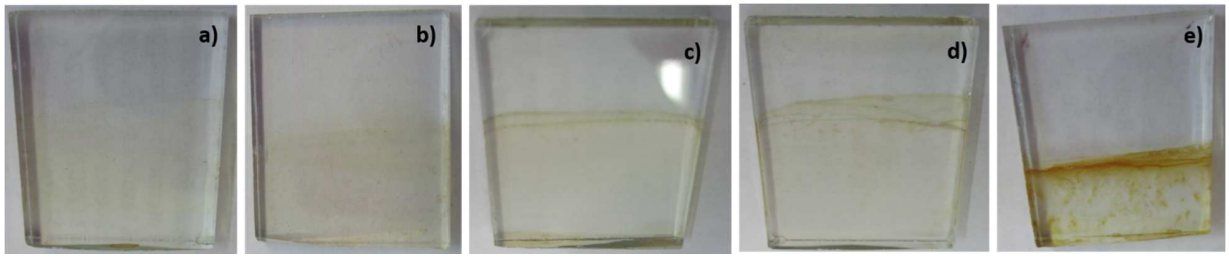

Figure 3.15: FTOcG substrates coated a) 1 time, b) 2 times, c) 3 times, d) 4 times, e) 5 times with a solution of 0,25 M iron and yttrium, 0,5M citric acid with a pH adjusted to 4.

As the coating solution is unstable in time, precipitates appear. They are localized in the supernatant and thus are visible on the deposition front (fig. 3.15 d).

We observe that the addition of surfactant in the solution stabilizes the solution for a longer time (fig. 3.16).

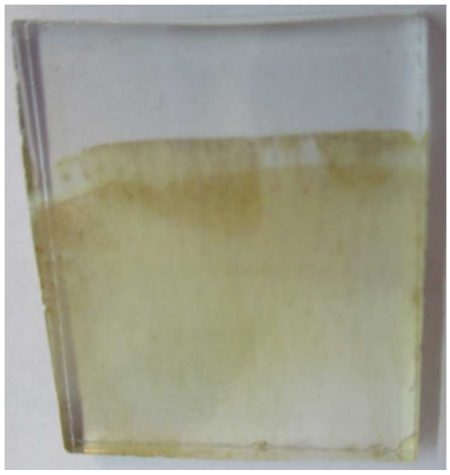

Figure 3.16: An FTOcG substrate coated 5 times with a solution of 0,25 M iron and yttrium, 0,5M citric acid with a pH adjusted to 4 mixed with a tipful of surfactant.

Figure 3.17: An FTO substrate coated 10 times with a solution of 0,25 M iron and yttrium, 0,5M citric acid with a pH adjusted to 4 mixed with a tipful of surfactant. Between the 5th and the 6th coating, the sample is heated at 300°C during 2h. After all the coating cycles, the sample is heated at 450°C for 2h.

Due to the transparency of the substrate, pictures of samples prepared on glass seem to have two deposition fronts. The front face of the substrate is coated with FTO. The other side is not coated, it is just glass. The front and back surfaces have different properties, corresponding to different affinities with the solution. The back face from fig. 3.16 was just not very well washed

before being put on the hot plate for stabilization. The deposition front that seems to be the higher along the dipping axis, is localized at the back of the substrate, on the non-conductive glass surface.

The quantity of coated material is improved if after 5 coating cycles, the samples are heated at 300°C for 2h and then re-coated 5 times (fig. 3.17).

Unfortunately, this sample doesn't contain crystallized o-$YFeO_3$ (fig. 3.18). The peaks localized at 2Θ = 26,5°; 33,7° and 37,9° correspond to the FTO substrate. The peaks belonging to FTO will therefore be referred by "#" symbol. The most intense o-$YFeO_3$ peak, should appear at 2Θ = 33°.

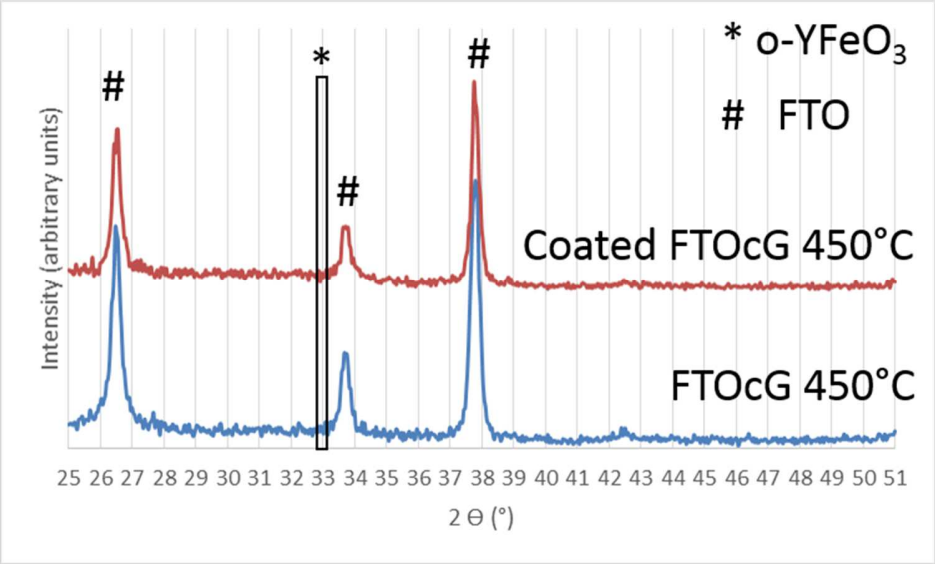

Figure 3.18: XRD patterns of FTO and FTO coated with a solution of 0,25 M iron and yttrium, 0,5M citric acid with a pH adjusted to 4 mixed with a tipful of surfactant. The two samples are then heated at 450°C for 2h.

To address this non-crystallized o-$YFeO_3$ problem, we tried to solve it in two different ways: 1) to use another organic acid additive or 2) to make a thermal study.

3.3.3 Obtaining a crystallized o-$YFeO_3$ film

In chapter 2, we investigated the effect of various **organic acids**. Malonic and tartaric acid, like citric acid, allow the crystallization of o-$YFeO_3$ at 450°C (fig. 2.6 d, e and f). We prepared two solutions based on same concentrations using the same protocol as described in section 3.3.2, but we substituted citric acid with malonic or tartaric acid, which are then coated on to FTO (fig. 3.19).

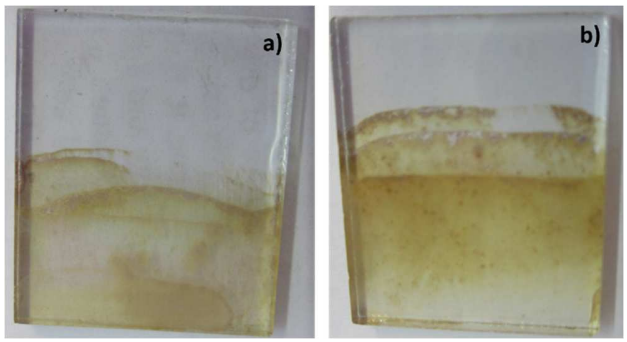

Figure 3.19: FTO substrates coated 5 times with a solution of 0,25 M iron and yttrium, 0,5M a) malonic or b) tartaric acid with a pH adjusted to 4 mixed with a tipful of surfactant.

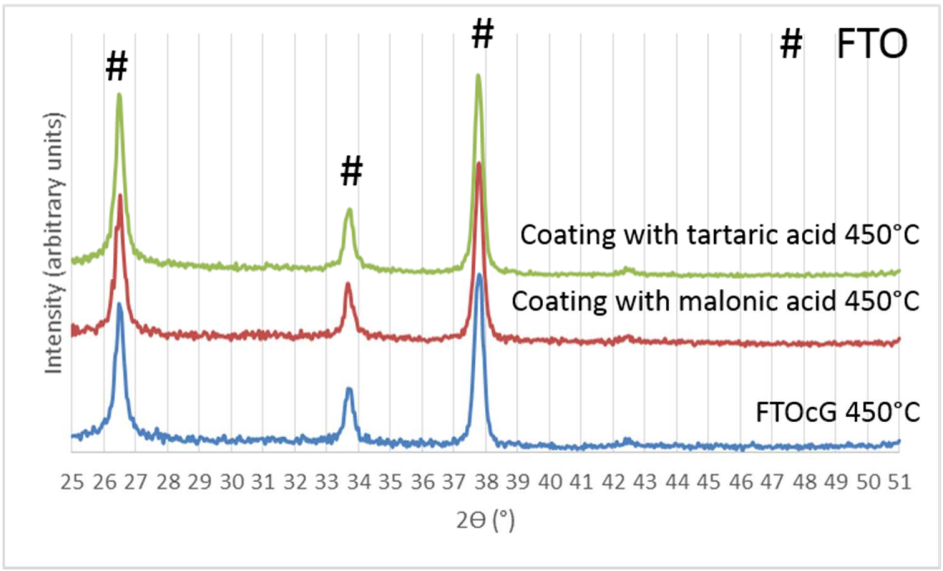

Figure 3.20: XRD patterns of FTO and FTO coated with a solution of 0,25 M iron and yttrium, 0,5M malonic acid (red line) or tartaric acid (green line) with a pH adjusted to 4 mixed with a tipful of surfactant. The two samples are then heated at 450°C for 2h.

No substantial difference appears in the diffractogram (fig. 3.20) of the two solutions prepared with different organic acids.

We decided to continue the study using citric acid. To study the influence of the temperature on crystallization, we use monocrystalline silicon as a substrate because at high temperature, above 600°C, glass melts.

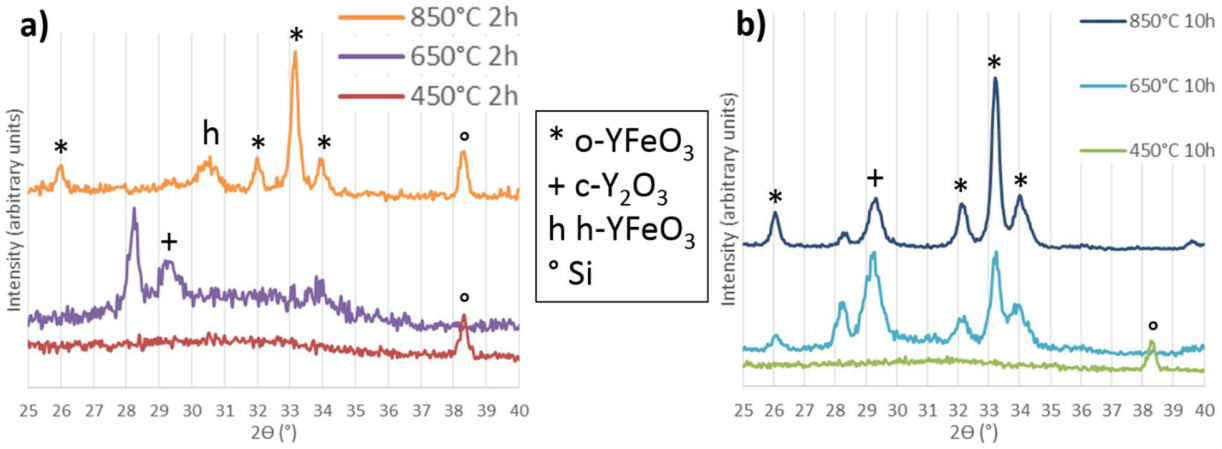

Figure 3.21: XRD patterns of Si substrates coated with a solution of 0,25 M iron and yttrium, 0,5M citric acid with a pH adjusted to 4 mixed with a tipful of surfactant. The samples are then heated at various temperatures for a) 2 hours or b) 10 hours.

We observe that orthorhombic yttrium orthoferrite does not crystallize at 450°C when it is deposited on a silicon substrate from a solution containing organic-acid. This is contradictory to what was demonstrated in chapters 1 and 2 for the preparation of powders from solution.

When deposited as a thin film, o-$YFeO_3$ crystallizes only after a thermal treatment of 2 hours at 850°C (fig. 3.21 a). In this case, $YFeO_3$ is also detected in its hexagonal crystal phase.

A longer treatment at a lower temperature, namely 10 hours at 650°C, also provides $YFeO_3$ but with a significant amount of impurities (fig. 3.21 b), such as c-Y_2O_3, and an additional non-identified impurity giving a peak at 2Θ = 28,2°. The onset of o-$YFeO_3$ crystallization at 650°C is consistent with TG-DTA studies reported by Rajendran et al.[4].

Those results show that the crystallization process differs between bulk solution and thin films. When the bulk solution is heated, the large quantities of gases are confined within the vessel and are readily brought to self-ignition. It seems that thin films of solution quickly

evaporate without reaching the required concentration and temperature to promote the ignition of pyrolytic gases.

3.3.4 Dip coating on FTO coated on borosilicate glass

With such a high temperature requirement, we were obliged to select another kind of substrate: Fluorine-doped tin oxide (FTO)-coated borosilicate glass, also known as Pyrex (FTOcP). Pyrex can handle such a high temperature.

We prepare a solution with an yttrium/iron/citric acid ratio of 1/1/2. We adjust the pH to 4 and coat the substrate with this solution in 5 coating cycles. The quantity of coated material at this point looks sufficient. We then heat the sample at 850°C for 2h.

Figure 3.22: An FTOcP substrate coated 5 times with a solution of 0,25 M iron and yttrium, 0,5M citric acid with a pH adjusted to 4 mixed with a tipful of surfactant and heated at 850°C.

Figure 3.23: An FTOcG substrate covered with 3 drops of a solution of 0,25 M iron and yttrium, 0,5M citric acid with a pH adjusted to 4 mixed with a tipful of surfactant and heated at 500°C.

Unfortunately too small a quantity of coated material remains on the FTOcP (fig. 3.22). Only the FTOcP peaks are visible on the x-ray diffractogram of this sample.

In order to bring the temperature of this sample to 850°C, we placed it in a crucible. After the heat treatment, we found o-$YFeO_3$ powder in this crucible. We believe that self—ignition reaction took place on this substrate. Gas evacuation happening during this treatment reduces the adherence of the material on the substrate. This mechanism is confirmed by doing another experiment:

The same solution was prepared and few drops were deposed on FTOcG, the quantity of solution was more important than in all the previous samples. This sample was heated under a fume hood. Indeed, when self-ignition happens, solid particles were ejected out of the substrate (fig. 3.23).

3.4 Conclusions

We prepare a solution that gives the most homogeneous coating on monocrystalline silicon by the dip coating technique. We try to use this solution on FTO coated glass but the condition to obtain crystallized orthorhombic yttrium orthoferrite requires a heat treatment that could lead to the melting of the substrate. Other samples based on FTO-coated borosilicate glass heated at 850°C show the presence of the desired o-$YFeO_3$.

A combustion reaction takes place during the synthesis and drastically reduces the adherence of the material to the substrate.

We decide to abandon the dip coating technique. We won't test the spin coating technique because same undesired reaction will happen.

3.5 Bibliography

1) Ku A. Y., Heward W. J., Mani V., *Templated synthesis of nanostructured europium-doped yttrium oxide thin films*, J. Mater. Sci., **2006**; Vol. 41, p. 3017-3025

2) Zhang L., *LR Ferrites*, IMS, **2006**, p. 1-20

3) Todorovsky D., Todorovska R., Petrova N., Uzunova-Bujnova M., Milanova M., Anastasova S., Kashchieva E., Groudeva-Zotova S., *Spray-pyrolysis, Deep- and Spin-coating deposition of thin films and their characterization*, Journal of the University of Chemical Technology and Metallurgy, **2006**; Vol. 41,p. 93-96

4) Rajendran M., Ghanashyam Krishna M., Bhattacharya A.K., *Low temperature preparation of orthoferrite thin-films by an inorganic sol-gel process*, Thin Solid Films, **2001**; Vol. 385,p. 230-233

5) Hartridge A., Ghanashyam Krishna M., Bhattacharya A.K., *Optical constants of nanocrystalline lanthanide-doped ceria thin films with the fluorite structure*, J. Phys. Chem. Solids, **1998**; Vol. 59, p. 859-866

6) Guo X.Z., Ravi B.G., Devi P.S., Hanson J.C., Margolies J., Gambino R.J., Parise J.B., Sampath S., *Synthesis of yttrium iron garnet (YIG) by citrate-nitrate gel combustion and precursor plasma spray processes*, J. Magn. Magn. Mater., **2005**; Vol. 295, p. 145-154

7) Xie H., Li Y., Jin S., Han J. and Zhao X., *Facile Fabrication of 3D-Ordered Macroporous Nanocrystalline Iron Oxide Films with Highly Efficient Visible Light Induced Photocatalytic Activity*, J. Phys. Chem. C, **2010**; Vol. 114, p. 9706-9712.

8) Yamaguchi O., Mukaida Y., Hayashida A., *Formation and transformation of tetragonal* $Y_3Fe_5O_{12}$, J. Mater. Sci. Lett., **1990**; Vol. 9, p. 1314-1315.

9) Işık D., Ak M., Durucan C., *Structural, electrochemical and optical comparisons of tungsten oxide coatings derived from tungsten powder-based sols*, Thin Solid Films, **2009**; Vol. 518, p. 104–111.

10) Nakaruk A. and Sorrell C. C., *Conceptual Model for spray pyrolysis mechanism: fabrication and annealing of titania thin films*, J. Coat. Technol. Res., **2010**, Vol. 7, Iss. 5, p. 665-676.

11) Perednis D. and Gauckler L.J., *Thin Film Deposition Using Spray Pyrolysis*, J. Electroceram., **2005**, Vol. 14, p.103-111

12) Attia S.M., Wang J., Wu G., Shen J., Ma J., *Review on Sol-Gel Derived Coatings: Process, Techniques and Optical Applications*, J. Mater. Sci. Technol., **2002**, Vol. 18, p. 211-218.

13) Brinker C. J., Frye G. C., Hurd A. J., Ashley C. S., *Fundamentals of Sol-Gel Dip Coating*, Thin Solid Films, **1991**, Vol. 201, p. 97-108.

14) Spiers R. P., Subaram C. V., Wilkinson W. L., *Free coating of a Newtonian liquid onto a vertical surface*, Chem. Eng. Sci., **1974**, Vol. 29,p. 389-396.

15) Landau L.D., Levich B.G., *Dragging of Liquid by a Moving Plate*, Acta Physiochim. URSS, **1942**, Vol. 17, p. 42-54.

16) Mayer H.C., Krechetnikov R., *Landau-Levich flow visualization: Revealing the flow topology responsible for the film thickening phenomena*, Phys. Fluids, **2012**, Vol. 24, p. 052103(1-33)

17) Henrie J., Kellis S., Schultz S. M., Hawkins A., *Electronic color charts for dielectric films on Silicon*, opt. express, **2004**, Vol. 12, p. 1464-1469.

18) Anderson A., Binions R., *The Effect of Brij® Surfactants in Sol-Gel Processing for the Production of* TiO_2 *Thin Films*, Polyhedron, **2015**, Vol. 85, p. 83–92.

Chapter 4: Coating by Ultrasonic Spray Pyrolysis (USP)

In the preparation of films by dip coating, as presented in chapter 3, the solution was coated on the substrate in a single process. However, the gases generated during the heating process were suddenly evolved in the coated film, leading to bubbles, cracks or delamination (fig. 4.1). To overcome this drawback, we selected the ultrasonic spray pyrolysis (USP). This deposition technique is based on an ultrasonic-aided generation of an aerosol, further blown onto a pre-heated substrate. With this method, we expect to coat the surface with particles that progressively undergo thermal decomposition, therefore avoiding a brisk gas evolution and associated cracking of the dried film.

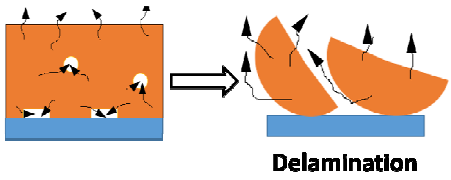

Figure 4.1 : A schematic representation of a evaporation mechanism for dip-coated films

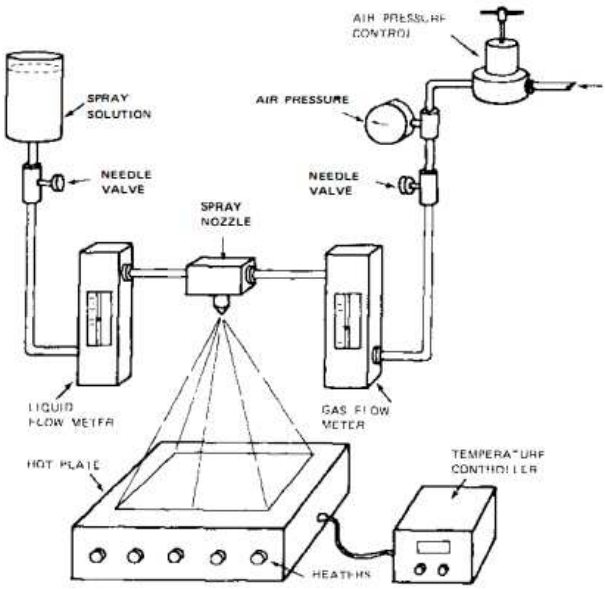

Figure 4.2: A spray pyrolysis system[7]

Many authors classify USP as a chemical deposition method[1-5]. This technique is one of the many evolutions of the spray pyrolysis developed by Chamberlin and Skarman[6] in 1966. Their spray deposition process can produce thin films (fig. 4.2) and their work mainly focuses on sulfides or selenides films for applications in the area of solar cells and photoluminescent or cathodoluminescent layers.

The literature relates various aerosol techniques under different names (tab. 4.1). Their names refer to the aerosol generation mechanism or the type of precursor used for the thermolysis reaction. “Spray pyrolysis” is the name which was finally imposed in the literature[7].

Term	Authors (year)
Evaporative decomposition of solutions	Roy, Neurogaonkar, O’Holleran, Roy (1977)
Spray Pyrolysis	Hirata, Kato (1979)
Chemical reactions with aerosols	Matijevic (1982)
Spray Roasting	Ruthner (1983)
Mist Decomposition	Imai, Takami (1985)
Ultrasonic Spray Pyrolysis	Ishizawa, Sakurai, Mizutani, Kato (1985)
Aerosol decomposition	Kodas, Datye, Lee, Engler (1989)
High-temperature aerosol decomposition	Moser, Lennhoff (1989)
Plasma vaporization of solutions	Pollinger, Messing (1993)
Solution aerosol thermolysis	Jayanthi, Zhang, Messing (1993)

Table 4.1: Nomenclature for Spray Pyrolysis Processes

Spray pyrolysis is a fast[2,7], simple and low cost[1-3,7-11] technique. It doesn’t require a vacuum and may be used in a continuous process[1,6,10,12]. The many advantages of this technique were quickly put to use within the industrial sector.

This method allows the coating of various compounds like oxides, sulfides, selenides, noble metals or tellurides[1,5-8,13]. Common substrates are made of glass, alumina, silica, stainless steel, sapphire, chromium oxide or In_2O_3-coated glass or soda-lime glass[1-3,5-7,9,14,15]. Such a variety of coatings have a wide range of applications: solar energy conversion, protection against corrosion, thermal barriers, wear resistance, biomedical material, catalysts, transparent conducting coatings, superconductors, optics, sensors or decorative effects[1-3,7-9,11,16].

4.1 Crucial points of Spray Pyrolysis process

The nature, thickness and homogeneity of the thin film obtained by this process depends on many parameters. The chemical composition of the precursor solution defines the final coated compound[1-3,6-10]. The temperature of the heating device, localized under the substrate (fig. 4.2 and 4.3), is reported as the main parameter[1-7,9]. The initial droplet size and velocity,

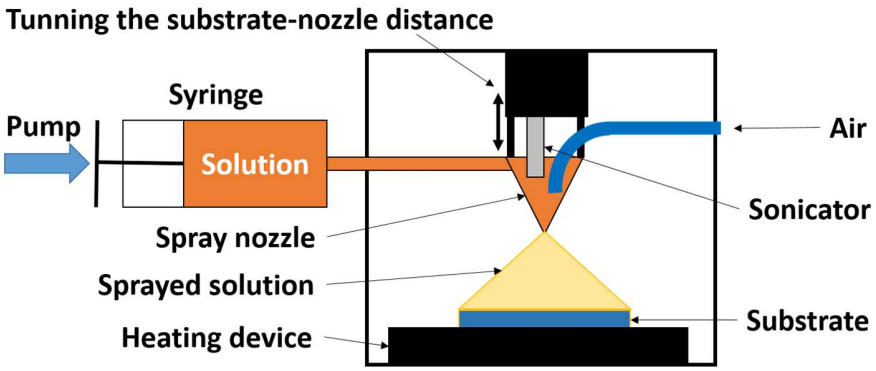

Figure 4.3: Representation of Ultrasonic Spray Pyrolysis system

fixed by the precursor's properties and the atomization process[1-3,5-9], combined with the heating rate explain the physical compound's state when impinging the substrate. The heating rate, and thus subsequent reactions, depends on the atomization process, temperature, precursor as well as the distance between the nozzle and the substrate[1,4,5,17], which is also a tunable parameter. The substrate's surface defines if the compound impinging on it can react and adhere[2]. As the coated surface is larger than the real sprayed surface, the spray nozzle must follow a programmed pattern to coat all of the desired surface.

4.1.1 Precursor's solution

Spray pyrolysis allows the use of a large choice of precursor solutions[9,18]. For safety and economic reasons, these choices must be shortened. Solvent, solute and other additives affect the solution properties and thus the nature and the characteristic of the deposited film[8,19,20].

4.1.1.1 Solute

To prepare metal oxide films, metal salts are often chosen. The metal salt must be soluble and stable in time, at room temperature, in the solvent[1] because precipitation may block the pipes and damage the apparatus. The precursors must decompose into the target compound. Chlorides, nitrates or metal-organic are commonly used as precursors[1,8,9].

Iron and yttrium chlorides were used to produce a powder of yttrium orthoferrite (see chapter 1). Even if these compounds are cheap and soluble in the solvent (water), they were not used with ultrasonic spray pyrolysis technique for two reasons: firstly, powders obtained with these precursors are less pure than the powder obtained from nitrates (see chapter 1),

secondly, chlorides are chemically aggressive and can cause corrosion of the experimental setup[9].

Nitrates are soluble in water. Upon drying and heating, they can dehydrate, melt and give volatile by-products during the thermolysis step[21].

According to the thermogravimetric (TG) study performed by Wieczorek-Cuirowa and Kozak[40], Iron(III) nitrate nonahydrate melts in its own water of crystallization, around 30°C. This melting is followed by an evaporation (or boiling depending on the temperature and the heating rate of the sample) and a simultaneous precipitation of $Fe(OH)(NO_3)_2$, $Fe(OH)_2NO_3$ and FeOOH. Fe_2O_3 is the final product, this oxide forms very slowly as a result of thermal dehydroxylation of FeOOH. The decomposition reaction (eq. 4.1) occurs at a broad range of temperatures (75 to 400°C). The lower temperatures require more time: the decomposition at 75°C needs at least 22 weeks.

$$Fe(NO_3)_3{\cdot}9H_2O \longrightarrow \text{liquefaction} \longrightarrow \text{evaporation + hydrolysis (1st step)}$$
$$\xrightarrow{-\{HNO_3\,-H_2O(1:6)\}} \text{system } Fe(OH)(NO_3)_2{:}H_2O = 1{:}2 \longrightarrow \text{evaporation} \xrightarrow{-H_2O}$$
$$\text{system } Fe(OH)(NO_3)_2{:}H_2O = 1{:}2 \longrightarrow \text{hydrolysis (2nd step)}$$
$$\xrightarrow{-HNO_3} Fe(OH)_2NO_3 \longrightarrow \text{decomposition} \xrightarrow{-HNO_3} FeOOH \longrightarrow$$
$$\text{dehydroxylation} \xrightarrow{-H_2O} \alpha\text{-}Fe_2O_3$$

Equation 4.1: The thermal decomposition of $Fe(NO_3)_3.9H_2O$[40]

Melnikov et al. study yttrium nitrate decomposition[41]. $Y(NO_3)_3.6H_2O$ becomes a liquid at around 50°C. According to their theory, one of the decomposition steps is a tetramer structure, they identify 9 decomposition steps on the thermogravimetric (TG) curve. The initial and final products are $Y(NO_3)_3.6H_2O$ and Y_2O_3 respectively. As the decomposition process generates a tetramer arrangement $Y_4O_4(NO_3)_4$, it is easier that $Y(NO_3)_3.6H_2O$ is written as $Y_4(NO_3)_{12}.24H_2O$ and Y_2O_3 as Y_4O_6 to facilitate comprehension in the thermal decomposition process (eq. 4.2).

$$Y_4(NO_3)_{12}.24H_2O \xrightarrow{-5H_2O} Y_4(NO_3)_{12}.19H_2O \xrightarrow{-3H_2O} Y_4(NO_3)_{12}.16H_2O \xrightarrow{-5H_2O} Y_4(NO_3)_{12}.11H_2O$$
$$\xrightarrow{-H_2O,-N_2O_5} Y_4O(NO_3)_{10}.10H_2O \xrightarrow{-2H_2O,-N_2O_5} Y_4O_2(NO_3)_8.8H_2O \xrightarrow{-4H_2O,-2N_2O_5} Y_4O_4(NO_3)_4.4H_2O$$
$$\xrightarrow{-4H_2O} Y_4O_4(NO_3)_4 \xrightarrow{-N_2O_5} Y_4O_5(NO_3)_2 \xrightarrow{-N_2O_5} Y_4O_6$$

Equation 4.2: The thermal decomposition of $Y(NO_3)_3.6H_2O$

4.1.1.2 Solvent

Although other solvents could be used for the precursor solution, in a similar way to ethanol as used in the chloride route (see chapter 1), water is chosen as a low cost, safe (non-flammable) and easy to handle solvent[1,8,17]. The solvent influences the boiling point of the solution, determining the speed of evaporation during the heating of the droplets, influencing the film's roughness as mentioned by Beckel[11] or by Neagu[20]. The solvent also determines the maximum metal salt solubility and the spreading behavior of the droplets. The deposition temperature and rate (depending on the selected flow rate[9]) are parameters mainly influenced by the solvent.

4.1.1.3 Additives

We plan to use citric acid and polyethylene glycol. These organic compounds help in gelation and polymerization reactions, modifying the properties of the solution[8,20,22,23], such as viscosity, metal salt solubility and the spreading of the droplets. During the pyrolysis process, they will release a lot of decomposition products, which increases the porosity of the film[3,23-25]. Citric acid mixed with nitrates generates heat *in situ*, sometimes mentioned as the Merck process[8]. Polyethylene glycol can reduce the number of cracks in the film[9,18,23,26] due to the binding properties of the polymer and can increase the spreading behavior of each droplet when it reaches the substrate[20,25].

4.1.2 Atomization

As a spray/aerosol technique, the way the droplets are generated determines the characteristics of the droplets[2] (tab. 4.2) and the nature and morphology of the coating. These atomization methods can be categorized as pneumatic (including pressure, nebulizer)[2,3,6-9,16], electrostatic[3,8,9,16] or ultrasonic[1-3,8,10,16,27].

Atomizer	**Droplet size (µm)[5,8]**	**Atomization rate (mL/min)[5,8]**	**Droplet velocity (m/s)[8]**
Pressure	5 - 100	3 – no limit	5 – 20
Nebulizer	0,1 - 2	0,5 - 5	0,2 – 0,4
Electrostatic	0,1 – 10	0,001 – no limit	No information
Ultrasonic	1 - 100	Maximum 2	0,2 – 0,4

Table 4.2: The characteristics of atomizers used in spray pyrolysis techniques

The atomization rate holds a strong interest for the industrial sector, as production yields increase with higher rates. Companies prefer to use pressure atomizers instead of ultrasonic atomizers. Indeed, the sprayed volumes are bigger (tab. 4.2) but the most advanced ceramic applications require small droplet pulverization at low exit velocities[8,28], achieved by USP or a nebulizer. A low exit velocity reduces bounce back (see paragraph 4.1.4.1) and solution wastage. The ultrasonically generated droplets have the narrowest distribution range for their size[1], allowing the best control of the deposition and reproducibility.

The volume of sprayed solution in a fixed time - the solution flow rate - is tuned by the syringe pump[4,17,28] (fig. 4.3). During our experiment, this parameter will vary between 0,1mL/min and 1mL/min. A higher rate induces a greater cooling of the substrate due to the endothermic evaporation of room-temperature solution.

The properties of the droplet, for a specific atomizer, depend on the solution density, viscosity, and surface tension[8,18,20,28].

Droplets leave the nozzle at ambient temperature and, by coming closer to the substrate, their temperature increases. This induces sequential reactions happening at ever higher temperatures[18]. The physico-chemical changes in the initial droplet will be discussed in paragraph 4.1.3 below.

4.1.2.1 Droplet properties

The Mean diameter of the initial droplet influences the type and number of reactions which occur before it reaches the substrate[2,24]. In process A (fig. 4.4), liquid droplets splash onto the substrate. These droplets still contain solvent which has to evolve, inducing possible delamination. The solid compounds (process B or D) have a low contact surface area with the substrate,

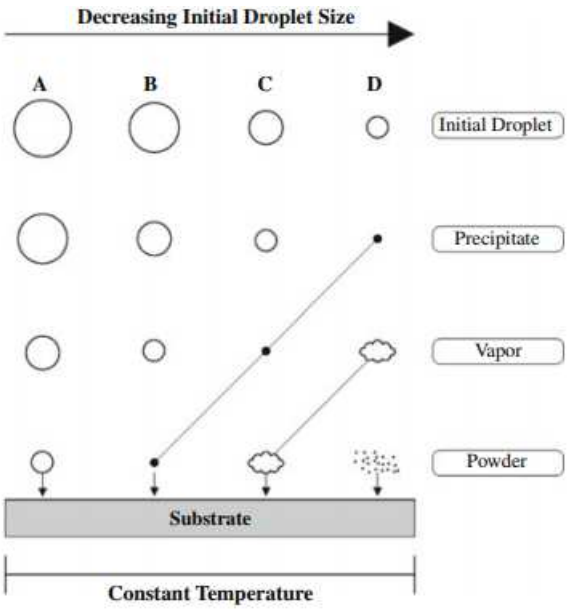

Figure 4.4: The mean diameter size of the droplets determines the phase that reaches the substrate[2]

reducing the adherence of the coating. Vapor deposition (process C) is the most favorable case in term of adherence. The contact with the surface is maximized and no solvent has to evolve.

The velocity of the droplets determines the residence time and the heating rate of the droplet before the contact with the substrate[8] which is directly proportional to the physico-chemical changes of the initial droplet.

4.1.2.2 Ultrasonic spray pyrolysis

Spitz and Viguié patented, in the early 70s[29], the Pyrosol process. The improvement of this process, compared to other spray pyrolysis methods, forms the ultrasonic droplets generation.

An ultrasonically excited liquid will form capillary waves on its surface. As these waves reach their maximal height, combined with cavitation effects within the liquid, numerous small droplets are generated producing an aerosol (fig. 4.5)[1,2,12,27,28].

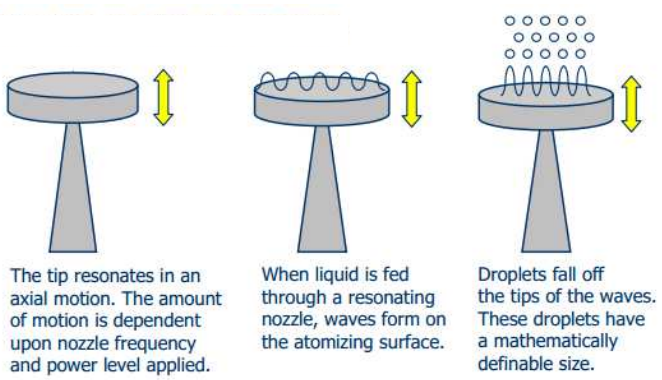

Figure 4.5: Ultrasonic aerosol generation[27]

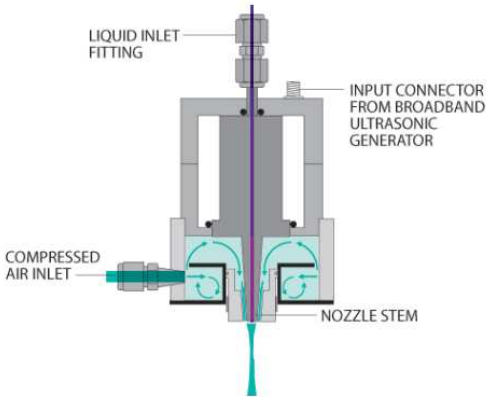

Figure 4.6: AccuMist® spray nozzle[30]

The size of the droplet is determined by the ultrasonic generator frequency[1-3,28]. This relation corresponds to Lang's equation (eq. 4.1). It gives a highly homogeneous droplet size distribution[1,12,27,28].

$$d = 0{,}34\left(\frac{8\pi\sigma}{\rho f^2}\right)^{1/3} \qquad \textit{Equation 4.1}$$

Where d is the diameter of the droplet, σ is the surface tension of the liquid, ρ the density of the liquid and f is the excitation frequency. As we don't intend to study the influence

of this parameter, we kept the frequency constant and equal to 120 kHz. If the diameter of the droplet varies, it is not due to the variation of the frequency.

The droplet velocity, in ultrasonic spray pyrolysis, is mainly due to the pressure of the carrier gas[1,4,17,18,26]. It is the source of kinetic energy that brings the solution down to the substrate. If the pressure is too low, the mist of solution will stay at the exit of the nozzle and won't reach the substrate. If the pressure is too high, an excessive cooling of the surface of the substrate can be observed.

Our USP is equipped with an AccuMist® nozzle (fig. 4.6) that uniformly distributes a flow of carrier gas around the nozzle stem. We set the air pressure at 0,98 psi to keep the velocity constant and reduce the number of studied parameters.

The nature of the carrier gas could be important. If the solvent of the sprayed solution is flammable, such as alcohols, and the carrier gas contains an oxidizing agent, such as dioxygen, combustion or an explosion can occur. As the solvent used in this study is water, air constitutes a cheap and safe carrier gas. The presence of oxygen can also promote faster decomposition of precursor and conversion into oxides.

4.1.3 Possible reactions during the flight of the droplets

A heated droplet undergoes several transformations[3,5,8,14,21].

The first reaction is **solvent evaporation**. This decreases the size of the droplet and increases the solute concentration.

Then, the solute **precipitates** in the droplet, generally at the droplet's surface, where the proportion of solvent is reduced. A crust of precipitated compound is thus formed around a core of solvent. In the case of a mixture of metal salts, successive or simultaneous co-precipitation may happen, giving respectively heterogeneous or homogeneous precipitated particles in the crust. With metalorganics, the precipitation may have the aspect of a polymerization or condensation before a gelation reaction.

After that, depending on the porosity of the solid crust, these particles can **dry out**, by just letting the rest of solvent vaporize through the crust, leading to a precipitated particle or **explode**, if the crust is not porous enough to allow solvent evaporation, leading to an increase

of internal pressure until explosion of the crust. The newly formed droplets have to undergo this cascade of transformations, considering the fact that their diameter is smaller, the temperature is higher and the route to the substrate is shorter. At the end of this step, no more liquid phase is present, just solid particles.

Thermolysis is the last transformation. This name encompasses many reactions like decomposition, vaporization, oxidation and/or sintering. These are the final reactions to obtain the desired coated compound.

All these reactions may happen in flight or on the substrate, depending on the initial mean diameter of the droplet, its velocity, on the distance between the nozzle and the substrate and on the temperature at each point between the heated substrate and the nozzle[1,5,18,20]. In our study, it is important to note that we kept the nozzle-substrate distance constant and equal to 5,5cm. For a fixed gas pressure, the decreasing of the distance between the nozzle and the substrate induces an increase of the deposition rate[19]. Furthermore, this distance determines the surface covered by the spray. A greater distance covers a larger surface but requires a faster droplet velocity induced by a higher carrier gas pressure. If the distance is too short, the temperature of the hot plate could damage the spraying device and also affect the solution in the tube of the machine before spraying.

The solvent has an evaporation time proportional to its quantity. High diameter droplets have a large quantity of solvent and in some cases, the full amount of the solvent is not evaporated before the droplets reach the substrate (case A in fig. 4.7). If the temperature of the substrate induces other reactions, they all take place after the spreading of the droplet on the substrate.

When a certain quantity of solvent has evaporated, the concentration inside the droplet reaches the saturation point and precipitation occurs (case B in fig. 4.7). In this case, a mixture of solid particles and liquid phase reaches the substrate.

If the precipitated particles are heated enough, depending on the chemical composition of the precursor's solution and temperature in the spray room, they can vaporize or even condensate before coming in contact with the substrate (cases C and D in fig. 4.7).

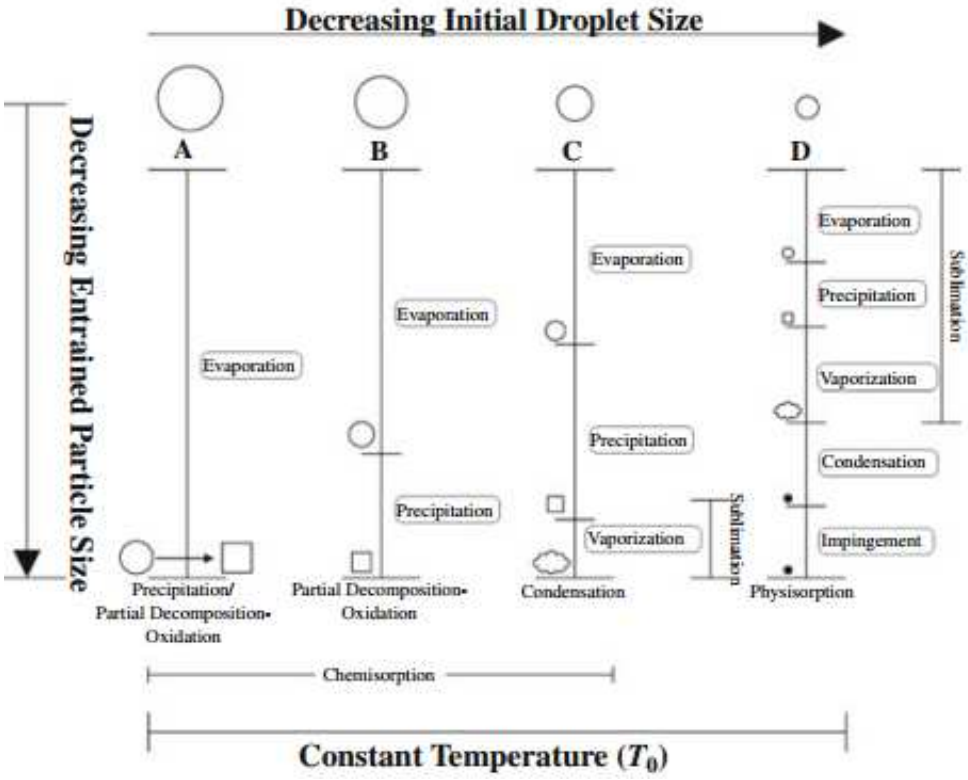

Figure 4.7: The mean diameter size of the droplets determines the reaction rate and the phase that reaches the substrate[2]

The type of process (A, B, C or D) affects the film morphology. Process A gives discs, circles or dried-cracked films due to solvent evaporation and tension release during the calcination step. Stacks of micrometric solid particles are the result of the process B. The morphology of films obtained by process D looks like a dust or powder deposition, absolutely not adherent. A USP deposit must be smooth, homogeneous and continuous. This morphology appears in the process C.

4.1.4 Heated substrate

A flat substrate is the target of the droplets. Furthermore, the thermal source is localized just behind it. Different techniques and apparatus can be used to obtain a homogeneous heating of the substrate like an infrared (IR) lamp[7], a liquid metal bath[7] or a conventional heating plate[7,9,11,13] as used in this study. The thermal conductivity and the thickness of the substrate influences the heat distribution.

4.1.4.1 Temperature of the heating device in USP

The heating temperature of the substrate is extremely important. It defines how far the particles are in the reaction process before impinging the substrate (see previous point). A study performed by Beckel et al. reports the influence of temperature on the homogeneity and the coherence of the film[11]. Castañeda et al. report a modification of the electrical resistivity and morphology of indium doped zinc oxide (ZnO:In) deposited on soda-lime glass due to a temperature variation[14]. Other publications also describe the link between the temperature and the morphology[9,31].

Temperature also induces a thermophoretic force that keep the smallest, lightest and slowest particles away from the substrate (fig. 4.8)[3,19,20].

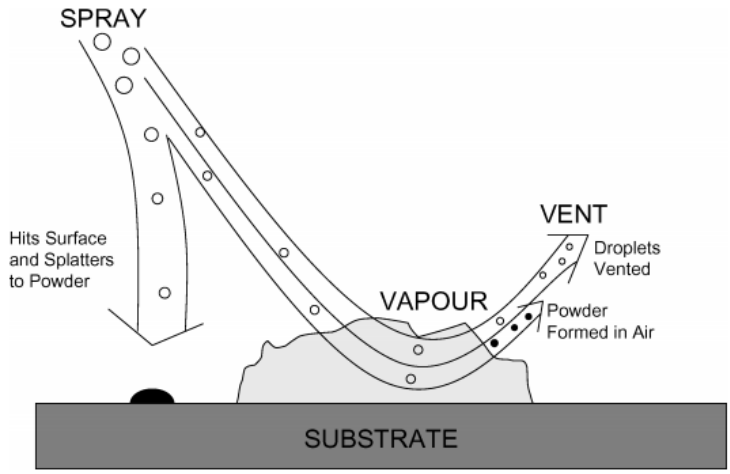

Figure 4.8: Aerosol transport mechanisms resulting from the initial velocity of the droplet, gravitational, Stokes/frictional and thermophoretic forces[3]

The thermophoretic force, sometimes mentioned as the Ludwig-Soret effect[32], pushes the particles away from a hot source. This movement results from the sum of the impacts at the particle's surface. Indeed, close to the heated substrate a particle is not alone. A particle is surrounded by other particles which do not necessarily move in the same direction, and can collide. Impacts can come from all directions and the impacts that come from the hottest side of the particle have a higher kinetic energy compared to the impacts coming from the coldest side. Thus for the same force of impact coming from both sides, the particle will be pushed away from the hot source. This is what we call the "thermophoretic force". The sum of other forces

(gravitational, initial kinetic energy etc) must be greater than thermophoresis to bring the particle in contact with the substrate. As the droplets are ultrasonically generated, their low velocities reduce the bounce back[28].

Muecke[19] explains that, in some cases, the Leidenfrost effect must also be taken into account. Droplets may still contain solvent when they reach the substrate (case A fig. 4.4 or 4.7) and the substrate temperature is high enough to form a thin vapor layer between the droplet and the substrate[20]. This effect makes the droplet levitate above its own vapor, never impinging on the substrate and is blown away by the air stream.

4.1.4.2 Substrate

As mentioned in the introduction, numerous substrates can be used in the ultrasonic spray pyrolysis technique. An appropriate substrate is temperature stable with properties fitting with the target applications[1]. This study was performed on monocrystalline silicon wafers (Si) for economical and availability reasons, FTO-coated glass (FTOcG) to meet the conductive and transparent application and FTO-coated Pyrex (FTOcP) to simultaneously avoid calcination treatment and meet the target application.

With a chemical deposition method, the substrate's surface must have a chemical affinity/reactivity with the impacting particles. Hydrophilicity-hydrophobicity or substrate's roughness must be considered to increase the spreading on the substrate[20]. The substrate's heat capacity, density and heat conductivity will influence the temperature above the substrate, giving a variation in the reaction rate of the droplet and thus in the coated film[19]. To maintain a reproducible surface, substrates were washed according to the same protocol[23,33] , previously mentioned in the chapter concerning dip-coating.

4.1.5 Spray pattern

As the sprayed area is smaller than the substrate, the nozzle must follow a **spray pattern** to cover all the substrate area. The selected pattern in the USP program is represented in fig. 4.9[26]. It is mentioned as "arc" in the "PathMaster" program. Another possibility is to keep the nozzle immobile and to move the substrate[7,13], but our apparatus does not allow such a technique.

In this pattern the length of the line (l) depends on the size of the substrate and the distance between each line determines the superposition ratio of various parallel coating lines. It is kept constant to 4 millimeters.

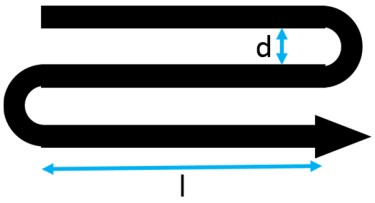

Figure 4.9: The spray line pattern with "d "the distance between 2 lines and "l" the length of the lines

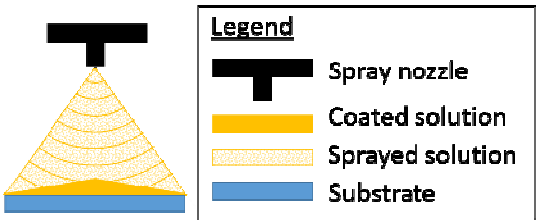

Figure 4.10: A representation of the influence on the coating of a radial spray on a flat surface

The **path speed** of the nozzle along the spray line pattern is also an important parameter. It defines the thickness of the deposit. If the nozzle moves slowly along its pattern, a large quantity of solution is sprayed on a fixed portion of the substrate. If the path speed increases, the nozzle spends less time above the same portion of substrate, coating less material. This speed is fixed to 40 millimeter per second. Furthermore, the radial dispersion of the solution in the spray and the flatness of the substrate implies that the quantity of deposited solution is more important in the center of the spray cone than at its edge (fig. 4.10). This leads to an inhomogeneous coating. We limit this undesired effect by tuning the distance "d" in the spray line pattern (fig. 4.9). A distance of 4 millimeters is adequate.

The number of **repetitions of spray** line pattern determines the thickness of the coating. USP can be used as a multi-layer coating technique[3,18,19,34,35].

The **delay between two repetitions** of the process has to be determined[18]. A short delay reduces the overall procedure time but it also reduces the thermolysis reaction time. If the time is too short, the coated particles will not have completely reacted before the next coating happens. In our case, the self-ignition reaction has to take place. This reaction produces gases and if this reaction is not finished before the next coating, it continues to produce gases under the next layer, inducing delamination.

4.1.6 Post treatment

Films obtained by ultrasonic spray pyrolysis are not crystallized enough. To obtain a crystallized yttrium orthoferrite coating, samples obtained by USP must be calcinated in a separate oven.

4.1.7 Summary of the studied parameters

Precursor solution

Composition: Nitrate metals (M^{3+}) in water with or without additives

Nitrate metals (M^{3+}): ..... $Y(NO_3)_3$ and $Fe(NO_3)_3$ (molar ratio 1/1)

M^{3+} concentration: .....5.10^{-3}mol/L to 1.10^{-1}mol/L

Additives: Citric acid (CA) and Polyethylene Glycol (PEG)

Molar ratio of CA/M^{3+}: .....2/1 to 3/1

Mass ratio of PEG/M^{3+}: .....0/1 to 10/1

Atomization

Liquid flow rate: .....0,1mL/min to 1,0mL/min

Atomizer: AccuMist® spray nozzle

Carrier gas: .....air

Pressure of the carrier gas: ....0,98 psi

Frequency: 120kHz

Deposition mode

Spray pattern: .....arc with interline distance equal to 4 mm

Path speed: .....40 mm/sec

Repetition of spray pattern: .....0 to 20

Time delay between two repetitions: 3sec to 60sec

Substrate

Substrate nature: .....Monocrystalline silicon, FTO-coated glass/Pyrex

Temperature of the heating device: ..200°C to 450°C

Distance spray nozzle-substrate: .....5,5 cm

Post-USP heating treatment: Calcination in an oven

Heating rate: .....300°C/h

Final temperature: .....450°C to 850°C

Time at the final temperature: 2h

4.2 Results and discussions

The first sprayed solution is based on the precursor's solution that gives the best results with dip coating. The solution is composed of peptized particles. One of the essential conditions for the precursor's solution, mentioned by Blandenet[1], is the stability of this source compound at room temperature. Unfortunately, the precursor's solutions used for dip-coating are not very

stable over a long period of time. Diluted solutions appear to be more stable in time. To prevent any congestion in the pipe between the syringe and the spray nozzle (fig. 4.3), we chose to dilute the solution.

4.2.1 Metal salt concentration

The first solution was prepared according to the protocol described in paragraph 3.3.4, in the previous chapter. The molar ratio is equal to 1/1/2 for yttrium, iron and citric acid respectively. The pH of this mixture is adjusted to 4 by the addition of NH_4OH. The yttrium or iron concentration is reduced to 5.10^{-3} mol/L. To shorten the legend under the forthcoming figures, this solution will be mentioned as "5.10^{-3}M of 1/1/2", where the concentration is the yttrium concentration and in "x/y/z", x, y and z are the molar ratio of yttrium, iron and citric acid respectively. The values of x and y are always equal to 1 as we plan to synthesize $YFeO_3$. All the solutions have a pH adjusted to 4. This information will not be mentioned anymore to simplify the legend. FTO coated glass (FTOcG) is chosen as substrate. The spray conditions are listed hereafter: flow rate=1mL/min, air flow=0,98 psi, distance nozzle-substrate=5,5cm, temperature of the heating device=450°C and path speed=40mm/s. For the samples coated more than once, the nozzle was put aside for 3 seconds between each spray procedure. We consider that every spray procedure coats one layer on the substrate.

At the end of only one spray procedure, the quantity of coated material is clearly insufficient (fig. 4.11a). We must repeat the procedure 10 times to observe a colored coating (fig. 4.11b) and 15 times to have a coating that presents the same color (fig. 4.11c) as the powder previously synthesized (fig. 1.1f).

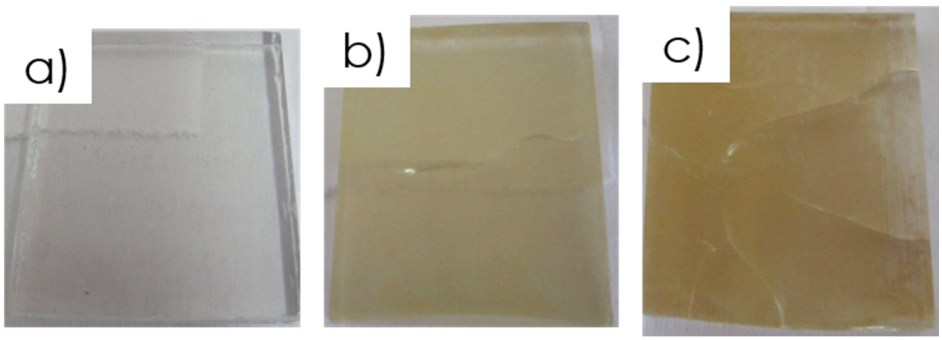

Figure 4.11: Films of 5.10^{-3} M solution of 1/1/2 coated a) 1 time, b) 10 times and c) 15 times by USP ($T_{substrat}$ 450°C) on an FTOcG substrate.

After multiple spray procedures, cracks were visible in the FTO substrate itself. Cracks were more and more frequent with the number of repetitions of the spray procedure. Their presence, length and shape are uncontrolled. This is expected to affect the conductivity and the efficiency of the film if used as a photoelectrode. Cracks are due to the thermal gradient between the surface in contact with the heating device and the surface on which the solution at a lower temperature is sprayed. To overcome this, we must reduce the number of layers. Das et al.[36] coated a $CH_3NH_3PbI_{3-x}Cl_x$ film at different concentrations. As expected, they report an increasing in the film thickness for more concentrated solution. Therefore, to have the same amount of deposited compound, we increased the M^{3+} concentration to 1.10^{-2} mol/L. No film was obtained for a solution with a concentration of 1.10^{-1} mol/L. Indeed, this solution is not stable enough and precipitates in the pipes, obtruding them.

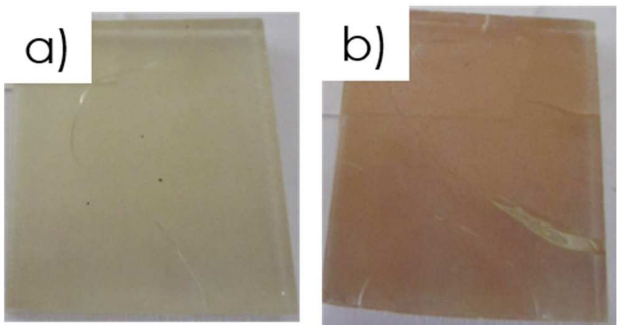

Figure 4.12: Films of 1.10^{-2} M solution of 1/1/2 coated a) 5 times and b) 10 times by USP ($T_{substrat}$ 450°C) on FTOcG substrate.

Samples obtained with a M^{3+} concentration of 1.10^{-2} mol/L (fig. 4.12a) still require to be coated too many times, causing cracks in the substrate. We need to work with a solution more concentrated than 1.10^{-2} mol/L and still taking care of avoiding its precipitation.

4.2.2 Complexing agent

Complexing agents interact with yttrium and iron cations and, as a complex, solubilize these cations by avoiding hydroxide precipitation. Vaqueiro and Lopez-Quintela[37] compare the complexation with citric acid and malonic acid. They observe precipitation with malonic acid. The calcination of such gels produces powders with a phase mixture. This does not happen when citric acid is used. Todorovsky and his group[38,] have proved the formation of mixed Y–Fe(III) citric complexes. Using a thermogravimetric (TG) study, they show that Y–Fe citrates are stable up to 50°C. The 1:1 complex dehydration proceeds in one step up to 125°C. In comparison, the dehydration of the Y citrate proceeds in two steps and is completed at 160°C. They conclude that their studied citrate compound is not a mixture of the monometallic complexes.

A proper amount of citric acid can complex the totality of yttrium and iron cations. We determined that the 1/1/3 molar ratio of yttrium/iron/citric acid allows the dissolution of all the species for a concentration of 1.10^{-1}mol/L yttrium or iron nitrate. It produces a clear solution for the M^{3+} concentration that previously plugged the pipes. The solution remains transparent whatever the pH adjustment. Samples coated with this solution are illustrated in fig. 4.13. From this point on, all solutions are prepared with this 1/1/3 molar ratio.

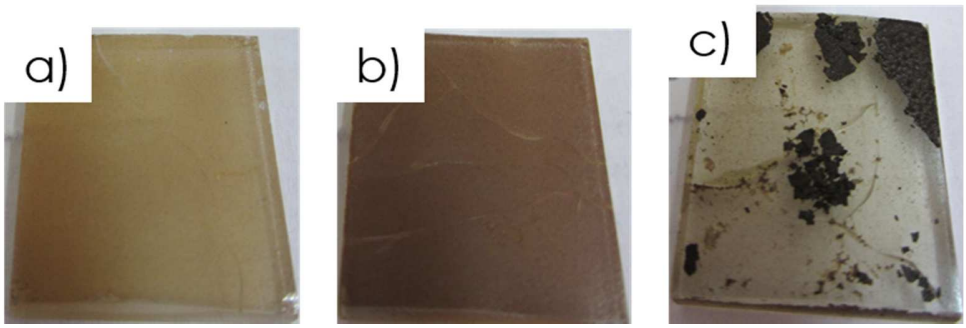

Figure 4.13: Films of 1.10^{-1} M solution of 1/1/3 coated a) 2 times, b) 5 times and c) 10 times by USP ($T_{substrat}$ 450°C) on an FTOcG substrate.

When samples are coated too many times, besides the fact that cracks appear in the substrate, the adherence of the coating on the substrate is reduced. The coating on the sample coated ten times (fig. 4.13c) is not adherent at all.

The crystallinity of the sample coated 5 times (fig. 4.13b) with the 1.10^{-1}mol/L solution is analyzed by X-ray diffraction. No peak corresponding to orthorhombic yttrium orthoferrite is visible in the diffractogram of the sample heated at 450°C (fig. 4.14 a). On a substrate adapted to avoid any melting (using FTOcP instead of FTOcG), the temperature can be increased to 850°C (fig. 4.14 b), leading to diffraction peaks corresponding to o-$YFeO_3$ (PDF: 04-010-6423). Despite the presence of some unwanted crystallized phases, like hematite (r-Fe_2O_3, PDF: 04-003-2900) or unidentified phase (peak at 2Θ=28,8°), orthorhombic yttrium orthoferrite is the major crystallized phase observed at this temperature.

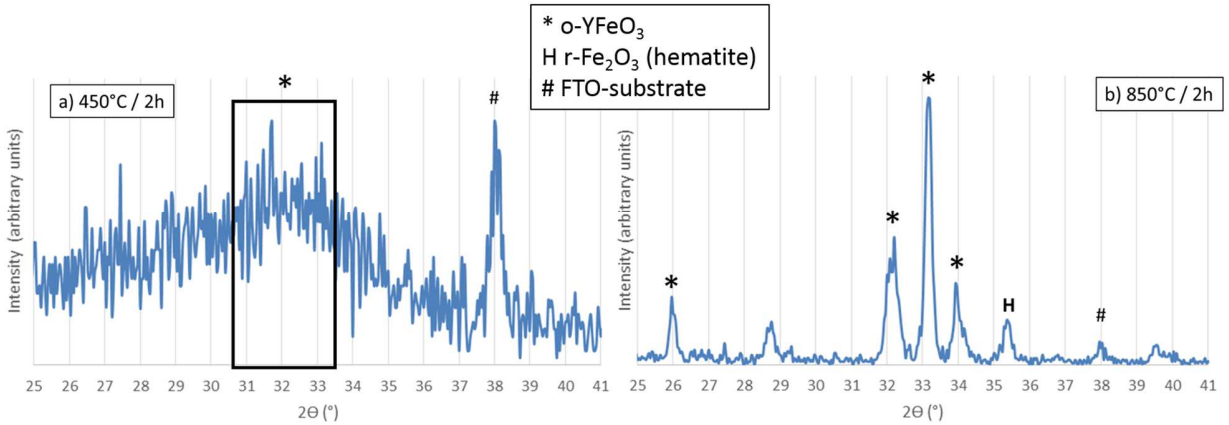

Figure 4.14: XRD patterns of a film obtained from a citric complex (1/1/3) solution ([M^{3+}]=1.10^{-1}M, $T_{substrat}$ = 450°C, 5 layers). Post-deposition calcination follows for 2h at 450°C (a) and 850°C (b).

4.2.3 Post-USP heating treatment

After calcinating at 450°C for two hours, the sample does not possess any diffraction peak corresponding to o-$YFeO_3$ on its XRD pattern (fig. 4.14a). This phase can be identified after heating at 800°C for two hours (fig. 4.15) but it still contains some impurities (hexagonal yttrium orthoferrite, PDF: 00-048-0529). This transition via a hexagonal phase before the orthorhombic phase at a higher temperature is not observed in powder material (see chapters 4 and 5). Powders and coatings do not have the same behavior when they are heated, due to the proximity and the number of the particles that compose the considered material. In bulk materials, every particle is surrounded by a lot of particles, more so than in the case of films. Thus, bulk material needs to be heated less than film to obtain the same crystal phase. The purest orthorhombic phase, for a coated material, is obtained after a heat treatment at 850°C for 2 hours (fig. 4.15). It confirms

what was previously reported in the chapter about dip-coating: powders require less thermal energy (450°C) to crystallize the orthorhombic phase.

From this point on, we will only use FTOcP as a substrate as it stands up to all post-USP heating treatments. This information will not be mentioned in the forthcoming legends.

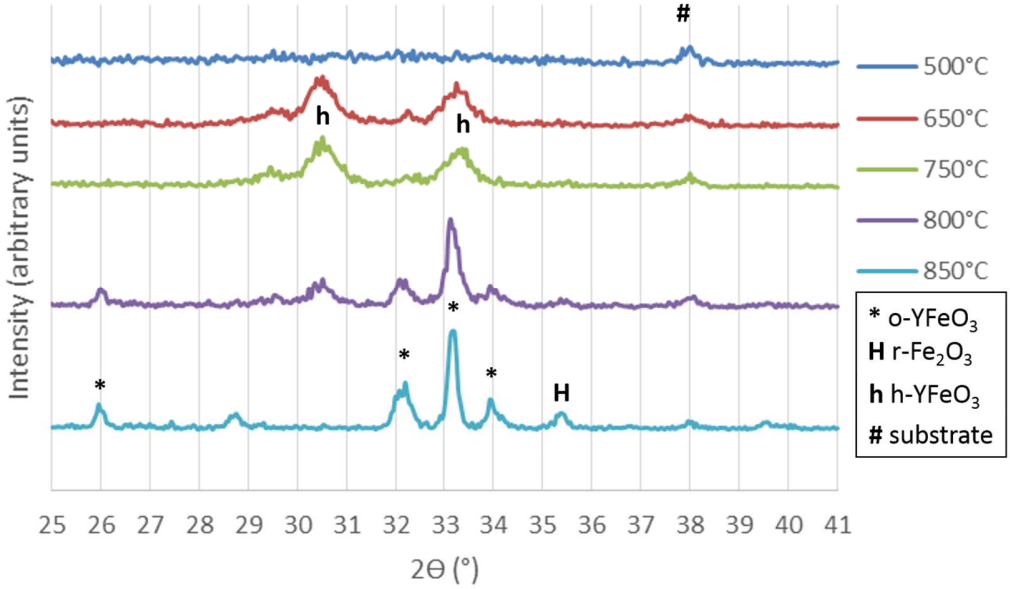

Figure 4.15: XRD patterns of films obtained from a citric complex (1/1/3) solution ([M^{3+}]=1.10^{-1}M, $T_{substrat}$ = 450°C, 2 layers, flow rate 1mL/min). Post-deposition calcination follows for 2h at 500°C (dark blue), 650°C (red),750°C (green), 800°C (purple) and 850°C (light blue).

4.2.4 Adherence improvement

A scratch was made on a film deposited on FTOcP (fig. 4.16a) to evaluate the adherence of the coating after calcination. The adherence was weak. A possible cause of the lack of adherence is the gaseous evaporation. To address the problem of adherence, we increased the time between spray sequences. Increasing the time from 3 seconds to 60 seconds allows all of gas to leave the coating before the next spray sequence.

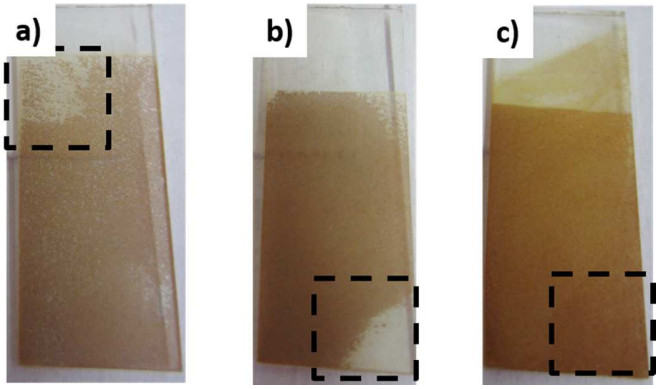

Figure 4.16: Films of 1.10^{-1}M citric complex (1/1/3) solution coated 2 times by USP ($T_{substrat}$ 450°C) with a delay time of a) 3 seconds or b) 60 seconds. Samples are then heated at 850°C for 2 hours. The third sample (c)) is prepared in the same way as b), but the coating is performed on an under-layer.

The coating looks denser when the time between sprays is longer but the adherence is not improved. The dashed windows (fig. 4.16) indicate the zone where a slight wiping was applied to test the adherence of the film.

We observe a significant improvement of the adherence when the coating is performed on an under-layer (fig. 4.16c). The under-layer results from the total wiping of a film previously sprayed on the FTOcP substrate. Consequently, all further samples will be prepared onto an under-layer.

This under-layer is a thin and smooth deposit of the precursor solution. Although the under-layer presents some defects due to stress release in the film or due to mechanical erosion (fig. 4.17 a & b), it gives a smoother surface than a bare FTOcP substrate (fig. 4.17 c). A smoother substrate helps the droplet to spread on the substrate. Roughness is one of the parameters, together with surface tension of the coated substrate, which Perednis identified as important for the spreading behavior of the droplet[9] and thus the film morphology.

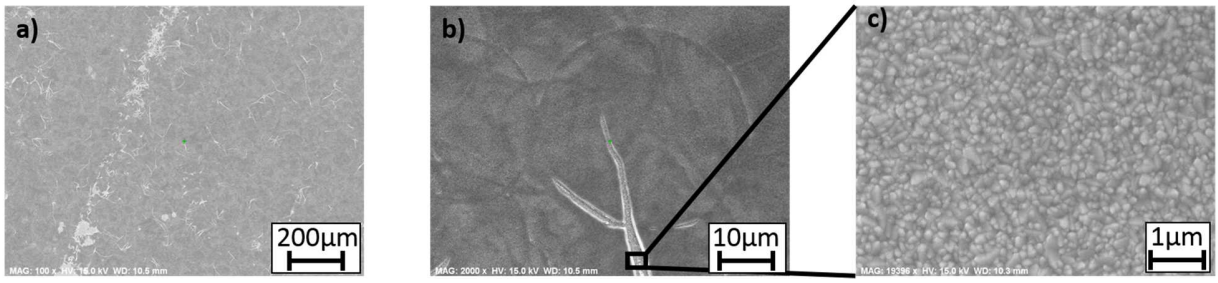

Figure 4.17: The surface morphology at two magnifications: 100x (a) and 2000x (b) of an under-layer of a 1.10^{-1}M citric complex (1/1/3) solution ($T_{substrat}$ 450°C, 1mL/min). Additional surface morphology of underlying FTOcP substrate (magnification: 20000x) (c).

An under-layer of a 10^{-1}M citric complex (1/1/3) solution with a pH adjusted to 4, even calcined at 850°C, does not present any diffraction peak in X-ray diffractogram (fig. 4.28). The film is too thin or does not contain enough matter to give observable diffraction peaks in XRD.

4.2.5 Morphological study of an adherent film

At 850°C, the coating is crystallized but not uniform (fig. 4.18). The morphology of this film is similar to a deposit made by Bian et al.[39] of MgO on a substrate heated at 630°C (fig. 4.19). At such a high temperature, the solvent is completely vaporized before the droplets reach the substrate surface. Precipitated particles strike the surface. These solid particles do not spread on the surface and as the deposition rate is important, 1,0mL/min in this case, the film grows faster in vertical direction (stacking of particles) than in horizontal direction (droplet spreading). To allow a better spreading and a subsequent more continuous film, the substrate temperature has to be reduced.

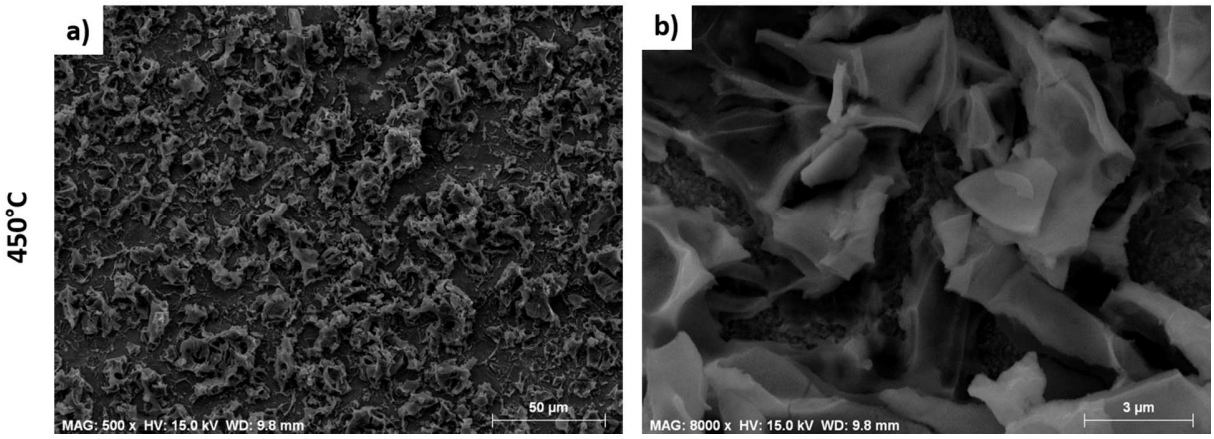

Figure 4.18: The surface morphology (two magnifications a) and b)) of a film of 1.10^{-1}M solution 1/1/3 coated twice ($T_{substrat}$ 450°C, 1mL/min) on an under-layer. The sample is then heated at 850°C for 2h.

Figure 4.19: A SEM micrograph for a MgO film deposited at 630°C[39]

4.2.6 Tuning the coating homogeneity

The 450°C substrate temperature was chosen according to the temperature determined during the powder synthesis (see chapter 2). But we deduced from the morphological study performed by scanning electron microscopy (fig. 4.18) that this temperature is too high to allow a uniform coating of the substrate.

4.2.6.1 Substrate temperature

Two samples were prepared with a substrate temperature of 300°C (fig. 4.20 a and b) and 200°C (fig. 4.20 c and d) respectively.

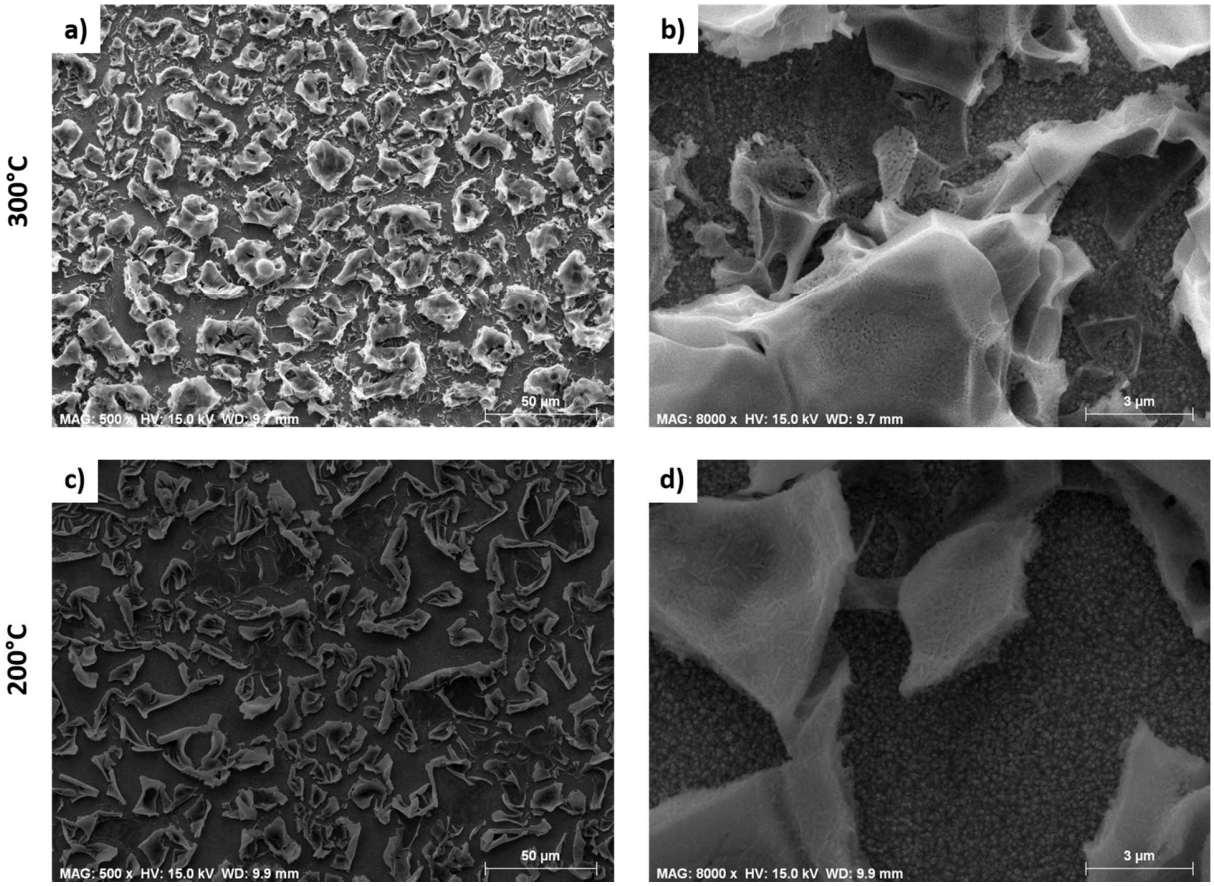

*Figure 4.20: The surface morphology of a film of 1.10^{-1}M solution of 1/1/3 coated twice (1mL/min) on an under-layer. Two magnifications (a & b) for the substrate heated at **300°C** and two magnifications (c & d) for the substrate heated at **200°C**. Both samples are then heated at 850°C for 2h.*

When the substrate is heated to 450°C, the film is made of a stacking of solid particles (fig. 4.18). The covering rate appears to be better for a substrate heated to 300°C (fig. 4.20), the film's morphology is similar to a dried liquid thick film, but the coating is still not uniform. The coating presents lots of cracks, due to drying, tension release and gas evacuation. The quantity of deposited material can be reduced by decreasing the solution flow controlled by the syringe (fig. 4.3). On the other hand, the roughness of a film can be reduced by adding some surfactant, like polyethylene glycol (PEG).

4.2.6.2 Flow rate

Until now, all films were obtained with a 1,0mL/min flow rate syringe-injected. We study the impact of the flow rate on film's morphology by reducing the value from 1,0mL/min to 0,5 and 0,1 mL/min.

Films obtained at 0,5mL/min (fig. 4.21) are more continuous than the deposited material at 1,0mL/min (fig. 4.20). This is in agreement with what Perednis et al. reported for yttria-stabilized zirconia (YSZ) films[9]. They showed that YSZ prepared with a low precursor flow rate exhibits less agglomerates and looks denser. However, the 0,5mL/min (fig. 4.21) sample still presents some cracks. Most of these cracks follow the borders of the circles left by the droplets. It is also observable on an SEM picture of the under-layer (fig. 4.17). Cracks result from the tension release in the weakest point of the film. The circles are reported to be the maximal spreading of a droplet[9,15,20]. The localization of these cracks is coherent with the discussion made by Neagu[20]: the evaporation is more intense at the border of the splat considering the temperature distribution in the liquid layer and in the substrate at the end of the spreading phase. It is due to a high local temperature and the presence of the triple contact point (solid-liquid-vapor).

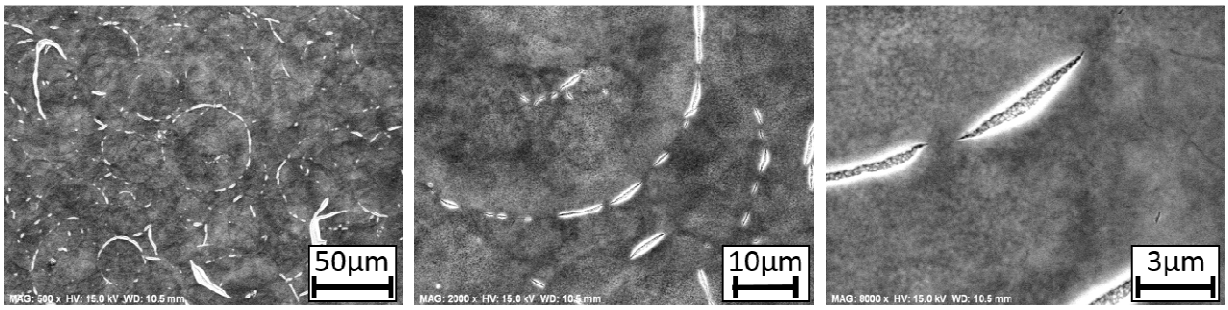

Figure 4.21: *The surface morphology (three magnifications) of a film of 1.10^{-1}M solution of 1/1/3 coated 2 times (at 300°C and **0,5mL/min**) on an under-layer. The sample is then heated at 850°C for 2h.*

Discs are visible in fig. 4.17 a & b and also in fig. 4.21. They differ from the rings with thick rims displayed in the film prepared with a flow rate of 0,1mL/min (fig. 4.22). Mueke et al.[15] observe this phenomenon when they change the salt saturation (fig. 4.23). Rings with thick rims correspond to an insufficient salt precipitation in the droplet when they impact the substrate surface. It allows the migration of the precipitated compound toward the edges of the deposited

droplet. This displacement is possible only if the time between two droplets strike on the same surface is long enough, according to Mooney[7] and Beckel[11]. This time is determined by the solution flow rate.

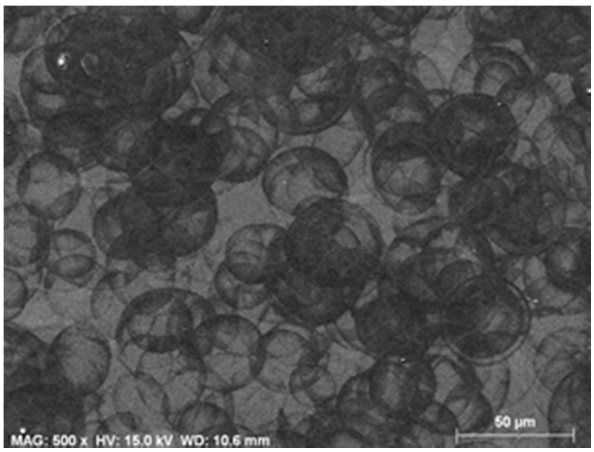

*Figure 4.22: Surface morphology of a film of 1.10^{-1}M solution of 1/1/3 coated 20 times (at 300°C and **0,1mL/min**) on an under-layer. The sample is then heated at 850°C for 2h.*

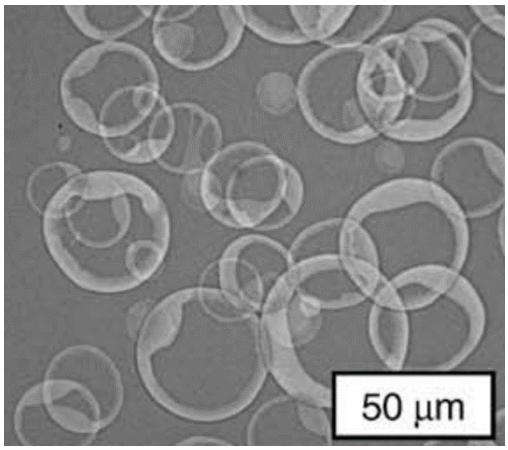

Figure 4.23: Thick rims observed by Mueke et al.[15]

When the flow rate is decreased down to 0,1mL/min (fig. 4.22), a first non-completely precipitated droplet reaches the substrate surface. This droplet has enough time to spread and dry on the substrate before a second droplet strikes the same area. It gives an inhomogeneous coating with lots of rings with thick rims.

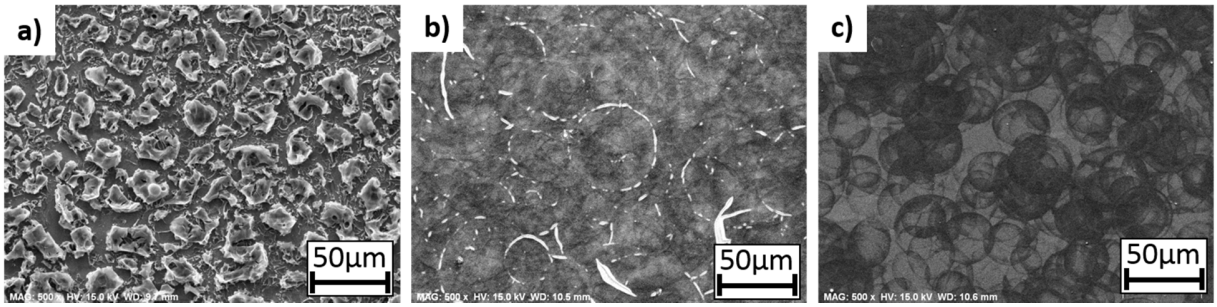

*Figure 4.24: The surface morphology of films obtained with a flow rate of **1,0mL/min**(a), **0,5mL/min**(b), **0,1mL/min**(c).*

Among the three tested flow rates (fig. 4.24), the most continuous coating is the sample prepared with a solution flow rate equal to 0,5mL/min (b). Therefore, we select this value for the next experiments.

4.2.6.3 Surfactant

The film thickness depends, among others, on the spreading of the droplet on the surface. Polyethylene glycol (PEG) is reported to change the film morphology from a cracked to a crack-free film[9].

Neagu[20] or Denayer[23] provide a reminder that the addition of PEG reduces the surface tension and from eq. 4.1, we deduce a decrease of the droplet diameter. According to Messing[8], the particle evolution process affects the film morphology. Small diameter droplets (fig. 4.4, process D) reach the substrate in a powdery phase, as reported in the Nakaruk paper[5].

The film mentioned as "PEG 1/1" (fig. 4.25) is obtained from a precursor solution prepared by mixing 0,38g of $Y(NO_3)_3.6H_2O$, 0,40g of $Fe(NO_3)_3.9H_2O$, 0,58g of citric acid and 0,4g of PEG (average molecular weight of 400 and a density of 1,128g/mL from Sigma-Aldrich) in 10,0 mL of distilled water. The pH is then adjusted to 4 by adding NH_4OH (10%). A similar mixture with 4,0g of PEG, instead of 0,4g, is used to produce the film named "PEG 10/1" in fig. 4.26.

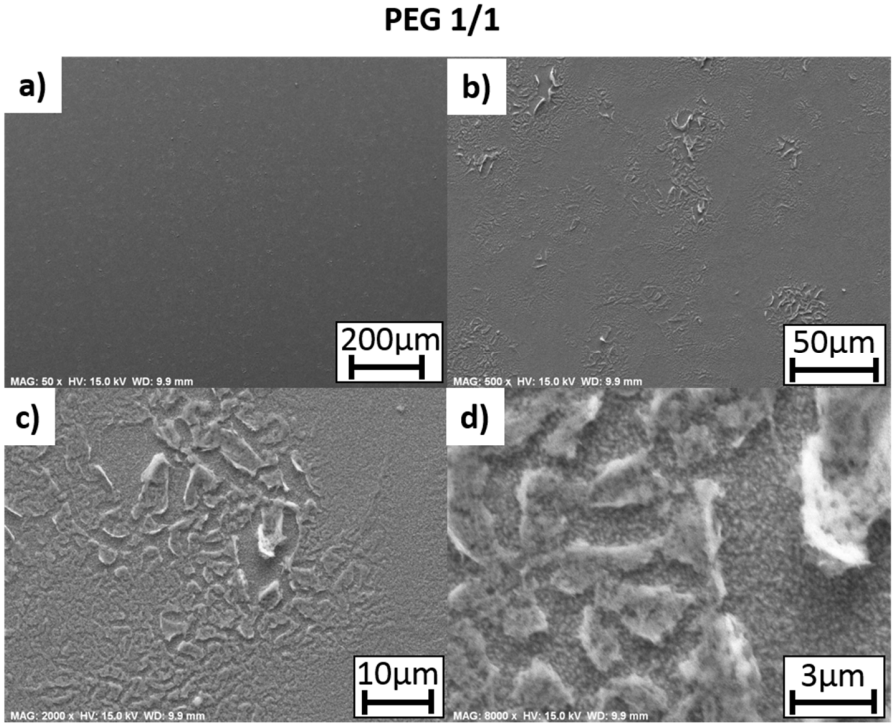

Figure 4.25: The surface morphology of a film of 1.10^{-1}M solution of 1/1/3 mixed with PEG/M^{3+} mass ratio 1/1 (four magnifications: a, b, c and d) coated 2 times (at 300°C and 0,5mL/min) on an under-layer. The sample is then heated at 850°C for 2h.

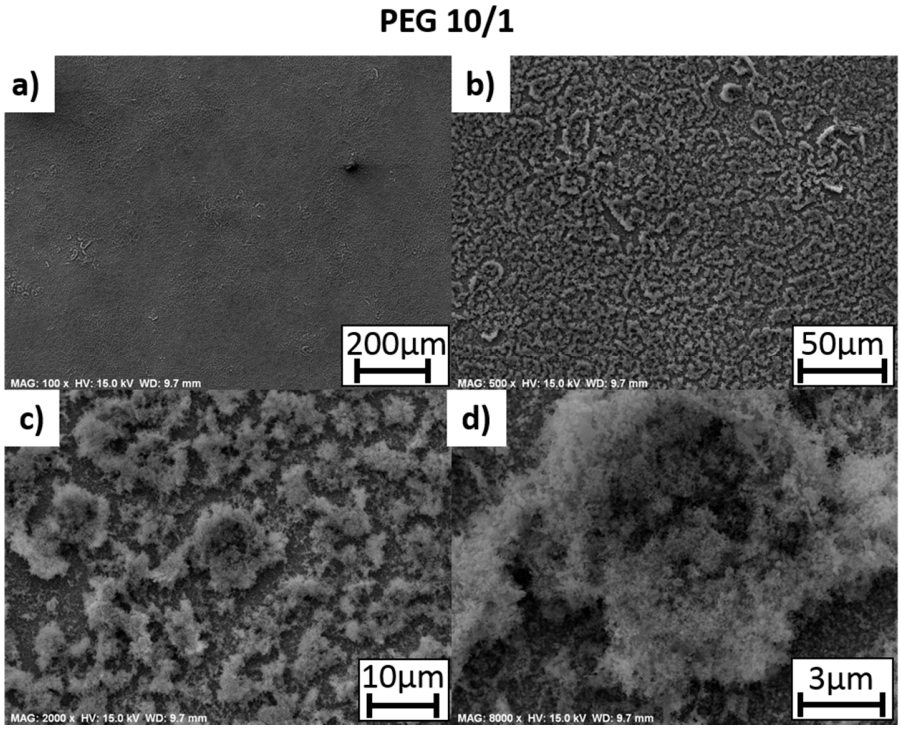

Figure 4.26: The surface morphology of a film of 1.10^{-1}M solution of 1/1/3 mixed with PEG/M^{3+} mass ratio 10/1 (four magnifications: a, b, c and d) coated 2 times (at 300°C and 0,5mL/min) on an under-layer. The sample is then heated at 850°C for 2h.

The PEG 1/1 sample is a smooth, thin and continuous film with some irregularities (fig. 4.25 a and b). For the higher PEG ratio (fig. 4.26), the film looks like a deposited fine dust which is absolutely not adherent. The solution containing PEG/M^{3+} = 10/1 does not lead to a continuous film.

When we selected the PEG/M^{3+}=1/1 solution and increased the number of layers up to 5 (fig. 4.27b), the film looks more continuous and contains less circular patterns than a film prepared according to the same process but without the polyethylene glycol (fig. 4.27a). These observations are coherent with the improvement of the spreading behavior of the droplets with a solution containing surfactant as reported by Denayer[23] or Deepa[25].

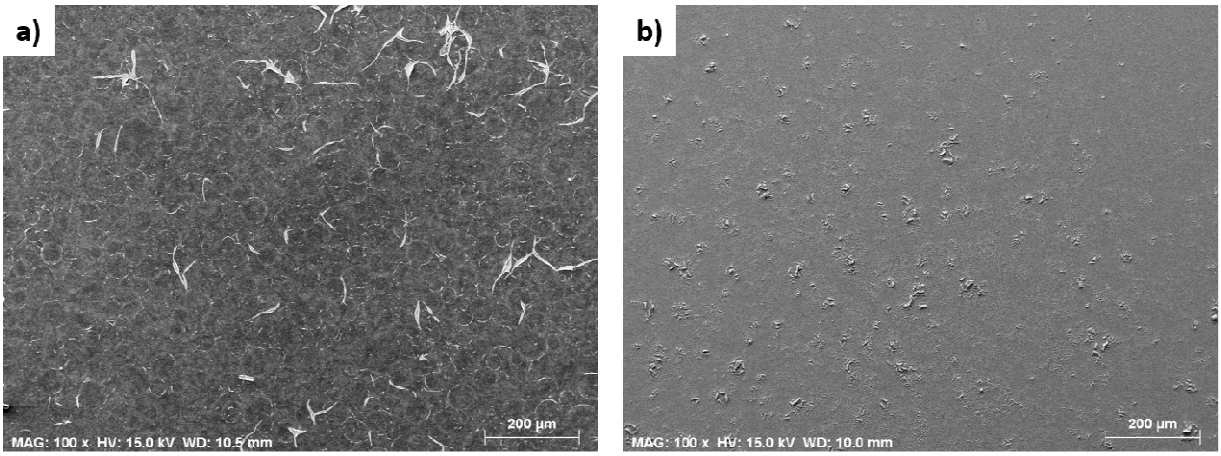

*Figure 4.27: The surface morphology of a film of 1.10^{-1}M solution of 1/1/3 a) without PEG, b) with PEG/M^{3+} mass ratio 1/1 coated 5 times (at 300°C and **0,5mL/min**) on an under-layer. The samples are then heated at 850°C for 2h.*

The under-layer (fig. 4.28 (blue line at the bottom)) does not contain any crystallized o-$YFeO_3$. X-Ray diffraction peaks at 2Θ = 26,5° and 33,9° correspond to an FTO substrate (#). Without polyethylene glycol (fig. 4.28 (red line in the center)), the main peak of orthorhombic yttrium orthoferrite, localized at 2Θ = 33,1°, is observable but less so than in the sample prepared with PEG in M^{3+}/PEG mass ratio equal to 1/1 (fig. 4.28 (green line at the top)). The main peaks of o-$YFeO_3$ (*), in the sample prepared with PEG, do not seem to have the right proportion for their intensity. Indeed, the peaks at 2Θ = 32° and 34° must have more or less the same intensity. Due to the small thickness of this film, the signal from the substrate combines with the signal from the crystallized o-$YFeO_3$ and gives a higher intensity at 2Θ =34°.

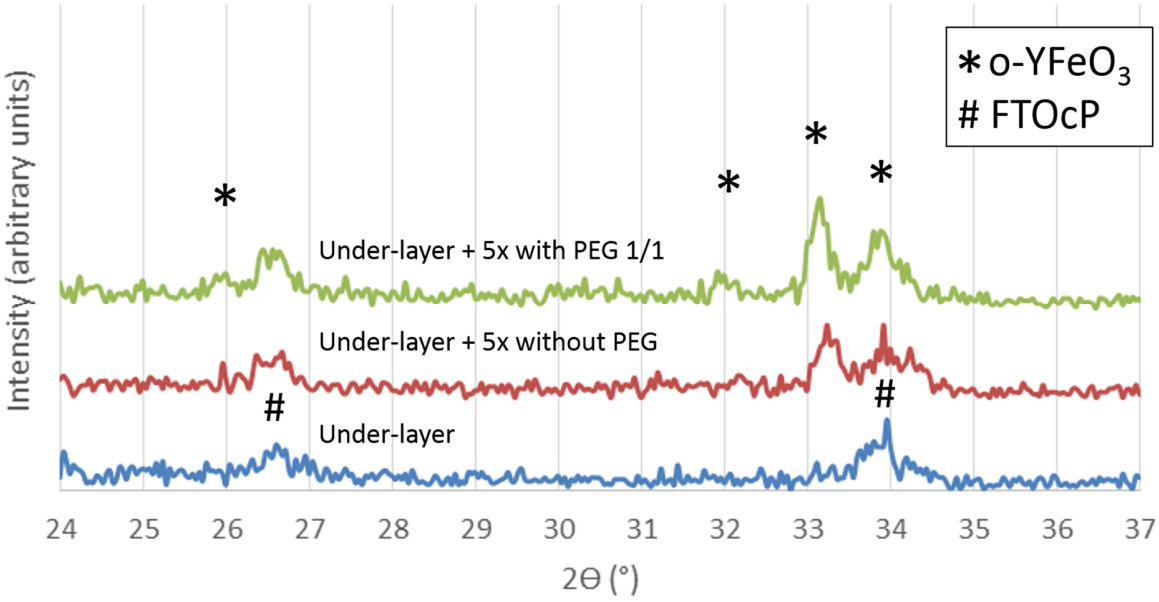

Figure 4.28: XRD patterns of a film obtained from a citric complex (1/1/3) solution ([M^{3+}]=1.10^{-1}M, $T_{substrat}$ = 450°C) mixed with PEG mass ratio 1/1: under-layer (blue line at the bottom), under-layer and 5 layers with (green line at the top) or without PEG (red line in the middle). Post-deposition calcination for 2h at 850°C.

4.2.7 Photoelectrochemical performances

The photoelectrochemical performances of the film - obtained from a citric complex (1/1/3) solution ([M^{3+}]=1.10^{-1}M) mixed with PEG mass ratio 1/1, coated with an under-layer and 5 other layers and heated at 850°C for 2 hours - were characterized by measuring the current (J in mA/cm²) generated in an electrochemical cell as a function of an applied bias voltage (E vs RHE (V)), which is the standard procedure to evaluate the performance of such photoanodes. Indeed, the position of the yttrium orthoferrite conduction band is lower than the water reduction potential and water reduction cannot happen without the application of a bias voltage.

We compared the data obtained in dark conditions (dashed curves in fig. 4.30) and under illumination (solid curves in fig. 4.30) to estimate the contribution of the photocurrent.

Front (fig. 4.29 b) and back (fig. 4.29 a) illumination give slightly different results. Indeed, in back illumination, the majority of photogenerated electron-hole pairs are localized close to the substrate. While electrons are quickly collected by the conductive substrate and injected into the external circuit, photogenerated holes have to migrate through the coating towards the

electrolyte solution. Furthermore, some of the photons are absorbed by the glass substrate before activating the semiconductor. The quantity of photogenerated electron-hole pairs may be reduced compared to the front illumination.

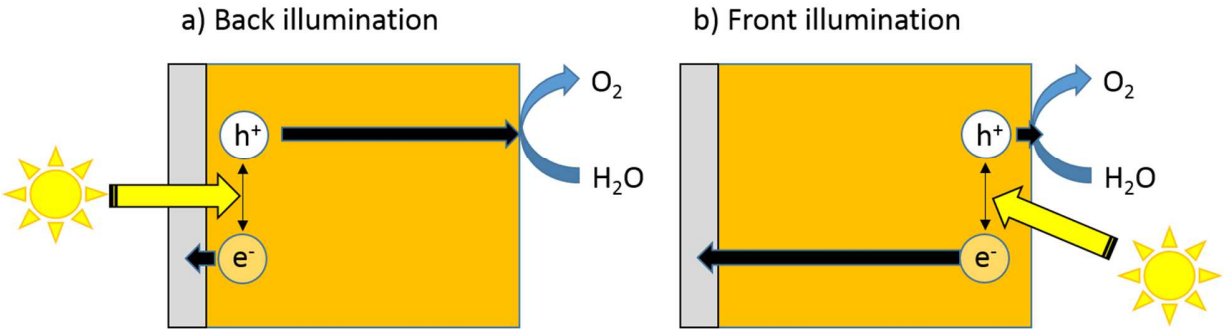

Figure 4.29: The migration of photogenerated species in back (a) and front (b) illumination

In front illumination, the electrons have to travel through the yttrium orthoferrite coating before reaching the substrate and the external circuit. On the contrary, holes can quickly oxidize water thanks to their generating area in the outer layer of the film.

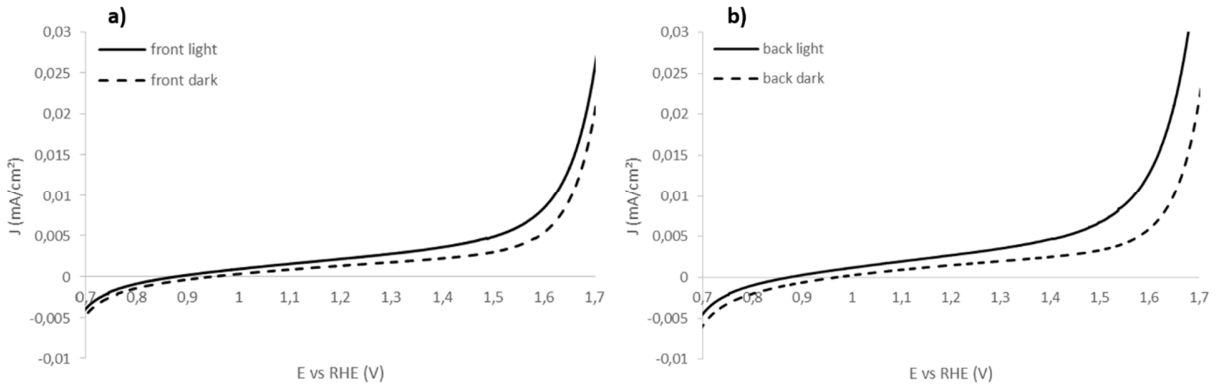

Figure 4.30: Comparison of the photocurrents obtained under front (a, solid curve) and back (b, solid curve) illumination. The dashed curves correspond to photocurrents obtained without illumination.

When the current generated by our sample is recorded in dark conditions, the oxidation potential of water is about 1,65V, which is translated by a sharp increase of current density above this value (fig. 4.30 a) and b), dashed curves). This represents the so-called "dark current". However, very little improvement is observed when the $YFeO_3$ is illuminated: the current density curve is displaced by less than 50mV towards the left. The effect is slightly more pronounced with

back illumination (fig. 4.30 b), solid line). This probably points to poor electron conductivity of the coating: the charges are more easily collected when generated close to the collecting substrate. To improve electron conductivity, future optimization of the material should be envisaged, like chemical doping. Toussaint et al.[42], during the development of Ti-doped hematite nanostructured films, actually relate the strong influence of dopant on the photoanode performance in a water splitting cell. With suitable doping of their material, they could lower the water oxidation potential down to 1,1V.

In summary, the best sample obtained so far by USP, that is homogeneous, adherent and crystallized (fig. 4.31) is made of 5 layers sprayed at 0,5mL/min from a precursor solution containing iron nitrate, yttrium nitrate (1.10^{-1} mol/L) mixed with citric acid in a molar ratio M^{3+}/CA = 1/3, to which PEG is added in a mass ratio PEG/M^{3+} = 1/1.

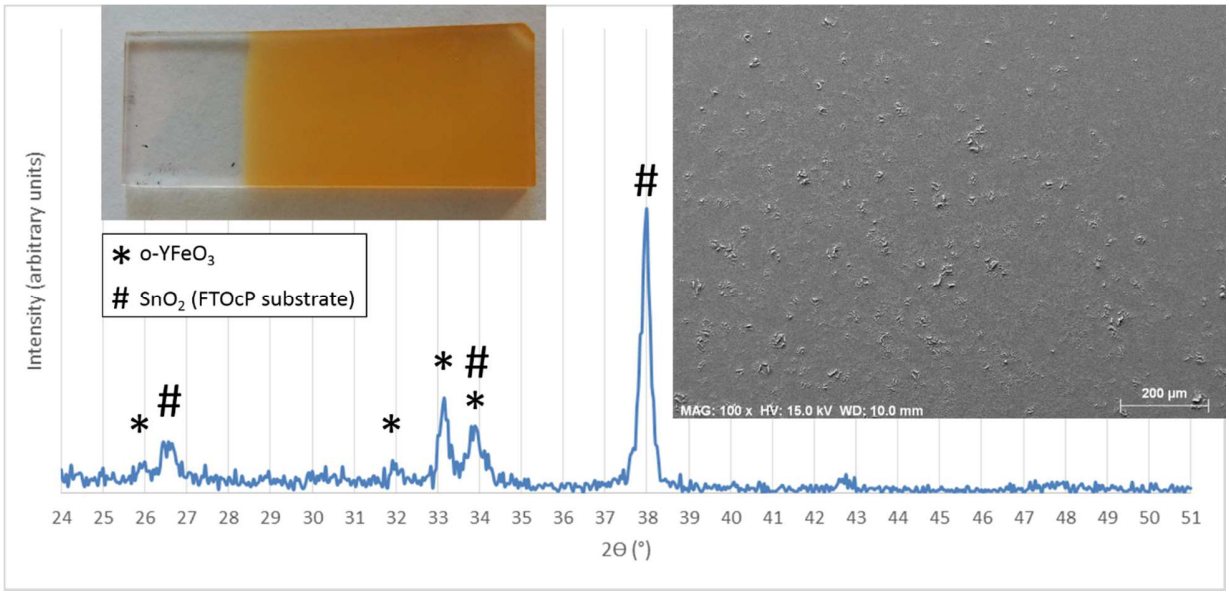

Figure 4.31: Visual picture, SEM image and X-ray diffractogram of a film of 1.10^{-1}M solution of 1/1/3 mixed with PEG mass ratio 1/1 with M^{3+}*/PEG respectively, coated 5 times (at 300°C and* ***0,5mL/min****). The sample is then heated at 850°C for 2h.*

4.3 Conclusion

This chapter focuses on Ultrasonic Spray Pyrolysis deposition technique for an orthorhombic yttrium orthoferrite film. This technique depends on a lot of parameters which allow a high versatility of applications. Although most of the parameters have to be tuned, some of them - like the type of spray nozzle, the pressure and type of the carrier gas, the atomization frequency, the spray pattern, the path speed and the distance between the nozzle and the substrate – are kept constant.

Among the studied parameters, we tested the metal concentration, the absence or presence, and their proportion, of citric acid and polyethylene glycol in the precursor solution and observed their influence on the material when it is coated on a substrate. The number of sprayed layers and the delay between spray sequences influence the adherence and the crystallinity of the coated material. These parameters are optimized and during this study, we highlighted the improvement of the adherence by an initial under-layer coated on the substrate. USP is a suitable technique to obtain an adherent and crystallized o-$YFeO_3$ (fig. 4.31).

4.4 Bibliography

1) Blandenet G., Court M., Lagarde Y., *Thin Layer deposition by the pyrosol process*, Thin solid films, **1981**, vol. 77, iss. 1-3, p. 81-90

2) Nakaruk A., Sorrell C. C., *Conceptual model for spray pyrolysis mechanism: fabrication and annealing of titania thin films*. J. Coat. Technol. Res., **2010**, Vol. 7, Iss. 5, p. 665–676

3) Perednis D., Gaukler L.J. *Thin Film Deposition Using Spray Pyrolysis*, J. Electroceram., **2005**, Vol. 14, p. 103-111

4) Desai J.D., Pathan H.M., Min S.-K., Jung K.-D., Joo O.-S., *Preparation and characterization of iron oxide thin films by spray pyrolysis using methanolic and ethanolic solutions*. Appl. Surf. Sci., **2006**, Vol. 252, Iss. 6, p. 2251-2258.

5) Viguié J.C. and Spitz J., *Chemical Vapor Deposition at Low Temperatures*, J. Electrochem. Soc., **1975**, Vol. 122, Iss. 4, p. 585-588.

6) Chamberlin R.R. and Skarman J.S., *Chemical Spray Deposition Process for Inorganic Films*. J. Electrochem. Soc., **1966,** vol. 113, iss. 1, p. 86-89

7) Mooney J. B. and Radding S. B., *SPRAY PYROLYSIS PROCESSING,* Ann. Rev. Mater. Sci., **1982,** Vol. 12, p. 81-101

8) Messing G.L., Zhang S.-C., Jayanthi G.V., *Ceramic Powder Synthesis by Spray Pyrolysis*, J. Am. Ceram. Soc., **1993**, Vol. 76, Iss. 11, p. 2707-2726

9) Perednis D., Wilhelm O., Pratsinis S.E., Gauckler L.J., *Morphology and deposition of thin yttria-stabilized zirconia films using spray pyrolysis*., Thin Solid Films, **2005**, Vol.474, p. 84–95

10) Wang W.-N., Purwanto A., Lenggoro W., Okuyama K., Chang H., Jang H. D., *Investigation on the Correlations between Droplet and Particle Size Distribution in Ultrasonic Spray Pyrolysis*, Ind. Eng. Chem. Res., **2008**, Vol. 47, Iss. 5, p. 1650-1659

11) Beckel D., Dubach A., Studart A. R., Gauckler L. J., *Spray pyrolysis of $La_{0.6}Sr_{0.4}Co_{0.2}Fe_{0.8}O_{3-\delta}$ thin film cathodes*, J. Electroceram., **2006**, Vol. 16, Iss. 3, p. 221-228.

12) Gillaspie D.T., Tenent R.C. and Dillon A.C*., Metal-oxide films for electrochromic applications: present technology and future directions*, J. Mater. Chem., **2010**, Vol. 20, Iss. 43, p. 9585-9592.

13) Tomar M.S. and Garcia F.J., *Spray pyrolysis in solar cells and gas sensors*, Prog. Cryst. Growth Charact. Mater., **1981**. Vol. 4, Iss. 3, p. 221-248.

14) Castañeda L., Maldonadob A., Escobedo-Moralesc A., Avendaño-Alejod M., Gómeze H., Vega-Pérezf J., Olverab M. de la L., *Indium doped zinc oxide thin films deposited by ultrasonic spray pyrolysis technique: Effect of the substrate temperature on the physical properties*, Mater. Sci. Semicond. Process., **2011**, Vol. 14, p. 114–119

15) Muecke U.P., Luechinger N., Schlagenhauf L., Gauckler L. J., *Initial stages of deposition and film formation during spray pyrolysis - Nickel oxide, cerium gadolinium oxide and mixtures thereof*, Thin Solid Films, **2009**. Vol. 517, Iss. 5, p. 1522-1529.

16) Guild C., Biswasa S., Menga Y., Jafarib T., Gaffneyd A. M., Suib S. L., *Perspectives of spray pyrolysis for facile synthesis of catalysts and thin films: An introduction and summary of recent directions*, Catal. Today, **2014**. Vol. 238, Iss. 0, p. 87-94.

17) Li C.-P., Lin F., Richards R. M., Engtrakul C., R. C. Tenent, Wolden C. A., *The influence of sol–gel processing on the electrochromic properties of mesoporous WO_3 films produced by ultrasonic spray deposition*, Sol. Energy Mater. Sol. Cells, **2014**, Vol. 121, Iss. 0, p. 163-170.

18) Bertus L.M., Faure C., Danine A., Labrugere C., Campet G., Rougier A., Duta A., *Synthesis and characterization of WO_3 thin films by surfactant assisted spray pyrolysis for electrochromic applications*, Mater. Chem. Phys. **2013,** Vol. 140, Iss. 1, p. 49-59.

19) Muecke U. P., Messing G. L. and Gauckler L. J., *The Leidenfrost effect during spray pyrolysis of nickel oxide-gadolinia doped ceria composite thin films*, Thin Solid Films, **2009**, Vol. 517, Iss. 5, p. 1515-1521.

20) Neagu R., Perednis D., Princivalle A. and Djurado E., *Initial Stages in Zirconia Coatings Using ESD*, Chem. Mater., **2005**, Vol. 17, Iss. 4, p. 902-910.

21) Enesca A. and Duta A., *Tailoring WO_3 thin layers using spray pyrolysis technique*, Phys. Status Solidi C, **2008**, Vol. 5, Iss. 11, p. 3499-3502.

22) Duta M., Perniu D. and Duta A., *Photocatalytic zinc oxide thin films obtained by surfactant assisted spray pyrolysis deposition*, Appl. Surf. Sci., **2014**, Vol. 306, Iss. 0, p. 80-88.

23) Denayer J., Bister G., Simonis P., Colson P., Maho A., Aubry P., Vertruyen B., Henrist C., Lardot V., Cambier F., Cloots R., *Surfactant-assisted ultrasonic spray pyrolysis of nickel oxide and lithium-doped nickel oxide thin films, toward electrochromic applications*, Appl. Surf. Sci., **2014,** Vol. 321, Iss. 0, p. 61-69.

24) Morales J., Sánchez L., Martín F., Ramos-Barrado J.R., Sánchez M., *Use of low-temperature nanostructured CuO thin films deposited by spray-pyrolysis in lithium cells*, Thin Solid Films, **2005**, Vol. 474, Iss. 1–2, p. 133-140.

25) Deepa M., Kar M., Singh D.P., Srivastava A.K., Ahmad S., *Influence of polyethylene glycol template on microstructure and electrochromic properties of tungsten oxide*, Sol. Energy Mater. Sol. Cells, **2008**, Vol. 92, Iss. 2, p. 170-178.

26) Denayer J., Aubry P., Bister G., Spronck G., Colson P., Vertruyen B., Lardot V., Cambier F., Henrist C., R. Cloots, *Improved coloration contrast and electrochromic efficiency of tungsten oxide films thanks to a surfactant-assisted ultrasonic spray pyrolysis process*, Sol. Energy Mater. Sol. Cells, **2014**, Vol. 130, Iss. 0, p. 623-628.

27) Sono-tek-*Investor-Presentation*, www.sono-tek.com/, Feb **2013**

28) Rajan R. and Pandit A.B., *Correlations to predict droplet size in ultrasonic atomization*, Ultrasonics, **2001**, Vol. 39, Iss. 4, p. 235-255.

29) Spitz J. and Viguié J.C., French Patent 2,110,622 (**1972**); U.S. Patent 3,880,112 (**1975**); U.S. Patent 3,890,391 (**1974**); F.R.G. Patent 2,151,809 (**1974**); Japanese Patent 83-845-7 (**1971**); Br. Patent 1,362,803 (**1974**)

30) Sono-tek, AccuMist Ultrasonic Nozzle, www.sono-tek.com, online 24 June **2015**.

31) Chen C.H., Emond M.H.J., Kelder E.M., Meester B., Schoonman J., *Electrostatic sol–spray deposition of nanostructured ceramic thin films*, J. Aerosol Sci., **1999**, Vol. 30, p. 959-967

32) Rosner D.E, Israel R.S, La Mantia B*., "Heavy" Species Ludwig–Soret Transport Effects in Air-Breathing Combustion*, Combust. Flame, **2000**, Vol. 123, p. 547-560

33) Işık D., Ak M., Durucan C., *Structural, electrochemical and optical comparisons of tungsten oxide coatings derived from tungsten powder-based sols*, Thin Solid Films, **2009**, Vol. 518, p. 104–111

34) Furusaki A., Konno H. and Furuichi R., *Perovskite-type lanthanum chromium-based oxide films prepared by ultrasonic spray pyrolysis*, J. Mater. Sci., **1995**. Vol. 30, Iss. 11, p. 2829-2834.

35) Amani Hamedan H., Investigation of deposition parameters in ultrasonic spray pyrolysis for fabrication of solid oxide fuel cell cathode, Thesis, **2008**

36) Das S., Yang B., Gu G., Joshi P.C., Ivanov I.N., Rouleau C.M., Aytug T., Geohegan D.B. and Xiao K., *High-Performance Flexible Perovskite Solar Cells by Using a Combination of Ultrasonic Spray-Coating and Low Thermal Budget Photonic Curing*, ACS Photonics, **2015**, Vol. 2, p. 680−686

37) Vaqueiro P., Lopez-Quintela M. A., *Influence of Complexing Agents and pH on Yttrium-Iron Garnet Synthesized by the Sol-Gel Method*, Chem. Mater., **1997**, Vol. 9, p. 2836-2841

38)Todorovsky D.S., Todorovska R.V., Groudeva-Zotova S., *Thermal decomposition of yttrium-iron citrates prepared in ethylene glycol medium*, Mater. Lett., **2002**, Vol. 55, p. 41-45

39) Bian J.M., Li X.M., Chen T.L., Gao X.D., Yu W.D., *Preparation of high quality MgO thin films by ultrasonic spray pyrolysis*, Appl. Surf. Sci., **2004**, Vol. 228, p. 297-301

40) Wieczorek-Ciurowa K., Kozak A. J., *The thermal decomposition of $Fe(NO_3)_3.9H_2O$*, J.Therm. Anal. Calorim., **1999**, Vol. 58, p. 647-651

41) Melnikov P., Nascimento V. A., Consolo L. Z. Z., Silva A. F., *Mechanism of thermal decomposition of yttrium nitrate hexahydrate, $Y(NO_3)_3.6H_2O$ and modeling of intermediate oxynitrates*, J. Therm. Anal. Calorim., **2013**, Vol. 111, p. 115–119

42) Toussaint C., Tran H. L. L., Colson P., Dewalque J., Vertruyen B., Gilbert B., Nguyen N. D., Cloots R., Henrist C., *Combining Mesoporosity and Ti-Doping in Hematite Films for Water Splitting*, J. Phys. Chem. C, **2015**, Vol. 119, p. 1642−1650

Chapter 5 : General conclusions and outlooks

5.1 Precursor selection for yttrium orthoferrite powder

We performed a comparison of liquid routes mentioned in the literature suitable for the production of yttrium orthoferrite powder. The crystal phase purity, estimated by X-ray diffraction, of the final powder, the cheap price and the safe handling of water solvent and the reduced hygroscopy of the metal salts, led this work to the selection of a synthesis protocol based on nitrate precursors. Orthorhombic yttrium orthoferrite powder was characterized by scanning electron microscopy and transmission electron microscopy. These studies exhibit the greater porosity of the powder obtained by the nitrate route compared to the powder obtained by the chloride route. Diffuse reflectance spectroscopy confirms that the optical band gap, deduced from a Tauc plot, is broad enough to simultaneously contain water oxidation and reduction potentials. As we plan to obtain a photocatalyst, with a suitable band gap and good porosity, thus a good surface, these are good omens for the target application: photo-electrochemical water splitting.

5.2 Influences of organic additives on powder synthesis protocol

Five organic additives (urea, oxalic acid, malonic acid, tartaric acid and citric acid) are respectively added in the precursor solution. These additions, for some of these molecules, highly improve the crystallinity and the purity of the final powder. These additives can be compared on the basis of their flexibility and on their ability to bind metal cations. The worst additive is urea. This molecule is small, not flexible and does not contain a carboxylic group, resulting in no possible bonds with Y^{3+} or Fe^{3+}. In opposition, the citric acid molecule is much longer and flexible and possesses 3 carboxylic groups, allowing a better complexation of the metal cations. The use of citric acid in the precursor solution increases the $YFeO_3$ phase content from 70% to more than 90% when the calcination temperature is equal to 850°C.

Furthermore, orthorhombic yttrium orthoferrite is obtained at a highly reduced temperature: 450°C, an interesting temperature considering that we plan to coat this material on to a glass substrate. At 450°C glass does not melt.

5.3 Dip coated films

Even if the technique of dip coating looks easy, we encountered lots of problems.

On monocrystalline silicon, we had some difficulties with the quantity of coated solution. We tried to fix this by increasing the number of coating cycles, by adding a small quantity of surfactant in the solution before the coating and by increasing the concentration of the solution.

More concentrated solutions show a time stability problem, indeed, precipitates appear during the coating process within the solution. To prevent this precipitation, we tried to peptize the precursor solution and study the pH influence on the stability of the solution by comparing the homogeneity of the coating; films coated on monocrystalline silicon have a color that depends on their thickness.

We determined the best solution parameters to obtain a homogeneous film on silicon, but when we tried to use this solution on FTO-coated glass, the affinity between the substrate and the solution were completely different.

When the coating on FTO-coated glass finally seems good, it appears that no o-$YFeO_3$ was crystallized. We have to heat our sample to 850°C before observing the expected diffraction peaks. To withstand this high sample temperature treatment, we needed to change the glass substrate to a borosilicated glass (= pyrex), which is much more expensive. Even with this substrate we encountered problems, the main one being the adherence of the film after the calcination treatment. We decided to try another coating technique.

5.4 Films obtained by ultrasonic spray pyrolysis technique

The first deposits were performed on FTO-coated glass. This substrate allows us to determine some parameters: the spray pattern, the number of coating, the best constituent proportions for the sprayed solution. At this point, two problems still persist: orthorhombic yttrium orthoferrite is not crystalized and the coating is not adherent.

A thermal study leads us to use FTO-coated pyrex. The purest o-YFeO3 phase is observed with a calcination temperature of 850°C.

The adherence problem was solved by coating with an under-layer before the usual spray cycle.

Scanning electron microscopy shows an extremely rough film with an important proportion of uncovered substrate. This was improved by adding polyethylene glycol to the sprayed solution.

The photoelectrochemical study of the final chosen sample demonstrates that this sample is suitable for water oxidation. Indeed, the oxidation potential of water is reduced from 1,65V (without illumination) to 1,6 V (with back illumination).

Even if our samples do not show photoelectrochemical performances as good as other material reported in the literature, this study has demonstrated that ultrasonic spray pyrolysis is a suitable technique to obtain a homogeneous, adherent and crystallized orthorhombic yttrium orthoferrite film on suitable substrates.

5.5 future research

Several studies could be performed to better characterize the synthetized material at every step of its synthesis: the complexation mechanism in the precursor solution and interatomic bindings can be studied more accurately by using infrared (IR), ultraviolet-visible (UV-vis.) and Raman spectroscopies. The morphology and microstructure of the orthorhombic yttrium orthoferrite films coated on FTO-coated pyrex can be obtained thanks to a Brunauer, Emmett and Teller (BET) surface area analysis method. The water splitting cell behavior can be studied by a technique called electrical impedance spectroscopy (EIS). The physical properties of the water splitting cell are extracted from a modeled equivalent circuit. EIS models impedance data in terms of an electrical circuit composed of ideal resistors (R), capacitors (C), and inductors (L). The four point probes characterizes the film resistivity. The drift mobility of electrons and holes in thin films can be estimated by a time-of-flight (TOF) apparatus.

Properties of the film can be modified and improved by changing the morphology or using another deposition method. The use of surfactants during the synthesis may produce an ordered mesoporous film with a higher specific surface. Due to the high calcination temperature during the production of the film, the surfactant must be stable enough at high temperatures and not produce a collapsed film.

The photoelectrochemical properties of orthorhombic yttrium orthoferrite may be improved by adding dopant. This could enhance electron or hole mobility.

Remerciements

Bien que ce soit mon nom qui apparaisse sur cette thèse, il faut savoir que je n'aurais jamais pu la faire sans l'aide de nombreuses personnes que je tiens à remercier.

Je tiens tout d'abord à remercier Monsieur **Rudi Cloots** pour m'avoir permis d'effectuer cette thèse au sein de son laboratoire,…

…madame **Catherine Henrist** pour son encadrement, ses conseils avisés, sa volonté d'acier et son jusqu'au-boutisme… elle a plus que mérité sa boite de marrons glacés…

…madame **Bénédicte Vertruyen** pour son inestimable soutien en matière de diffraction des rayons X, de révision de publication, d'organisation de voyage pour des colloques à l'étranger, pour sa rigueur et sa serviabilité…

…monsieur **Frédéric Boschini** pour tout ce qu'il apporte au labo et au bureau que j'ai occupé ces 6 années : des chercheurs ou stagiaires dans mon bureau, des couleurs sur les murs, de l'humour dans les couloirs et des pralines pour les grandes occasions….

… tous les membres du laboratoire **LCIS-GREEnMat** qu'ils y soient encore ou qu'ils n'y soient plus…, plus particulièrement **Gilles Spronck** qui chante et qui a la banane… **Mélanie Rondeux** qui colorie ses DRX en souriant comme une gamine de 6 ans… tous les **étrangers** qui sont passés dans mon bureau, grâce à eux j'ai pris plaisir à parler anglais et j'ai su dire « à tes souhait » en indien, bulgare et chypriote…

… à **Christelle et Anaïs** pour… toutes les raisons qui font que je les aime…

… à mes **parents** pour leur soutien tant financier qu'affectif…

… à la famille **McCann** pour les longues heures qu'ils ont passé à corriger l'orthographe et la grammaire de cette thèse.

… à tous les **étudiants** qui m'ont ont, Ils m'ont ouvert les yeux sur le plaisir que je prends à transmettre un savoir.

… à tout mon entourage (famille et amis) qui n'ont bien souvent rien à voir avec cette thèse mais dont le fait de les côtoyer rend ma vie très agréable.